UNIVERSITY OF LEEDS
SCHOOL OF EARTH AND ENVIRONMENT

Coprecipitation of Mixed Radionuclides From Large Volumes of Nuclear Waste Water Via Carbonate Coprecipitation Reactions

Author:
David J. HODKIN

Supervisors:
Dr. Ian T. BURKE
Dr. Doug I. STEWART
Dr. James T. GRAHAM

SUBMITTED IN ACCORDANCE WITH THE REQUIREMENTS FOR THE DEGREE OF DOCTOR OF PHILOSOPHY

April, 2018

The Candidate confirms that the work submitted is his own, except where work which has formed part of jointly authored publications has been included. The contribution of the candidate and the other authors to this work has been explicitly indicated below. The candidate confirms that appropriate credit has been given within the thesis where reference has been made to the work of others.

The following chapters contain jointly published material:

Chapter 4

- Hodkin D.J., Stewart D.I., Graham J.T., Burke I.T. (2016). Coprecipitation of ^{14}C and Sr with carbonate precipitates: The importance of reaction kinetics and recrystallization pathways. Science of the Total Environment, **562**, pp. 335-343

Chapter 6

- Hodkin D.J., Stewart D.I., Graham J.T., Cibin G., Burke I.T. (2018). Enhanced Crystallographic incorporation of Strontium(II) ions to Calcite via Preferential Adsorption at Obtuse growth steps, Journal of Crystal Growth and Design, Just Accepted Manuscript.

Acknowledgements

This research has been carried out by a team which has included Ian T Burke, Doug I Stewart, and James T Graham. My own contributions, fully and explicitly indicated in the thesis, have been concept development, experimental work, model development and thesis preparation. The other members of the group and their contributions have been as follows I.T Burke, Development of initial concept, assistance with method development, assistance with data interpretation and comments on manuscript. D I Stewart, concept development, assistance with data interpretation, assistance with modelling and comments on manuscript. J T Graham, concept development, information on site specific conditions and research context and comments on manuscript.

Thanks are given to the technical staff in the Cohen Geochemistry labs whose knowledge made my lab work significantly more efficient. Divyesh Trivedi from the NNL for training and assistance with PHREEQC model development. Samuel Adu-Amankwah from the Department of Civil Engineering at the University of Leeds for his help with experimental design and data collection for the cement work included in chapter 7 and Giannantonio Cibin from the Diamond light source for EXAFS/XANES data collection for the calcite solid solution work in chapter 6.

My thanks must also go to my wife Katy for her tireless support over the last 3.5 years, my parents for encouraging my interest in science from a young age, and all of my family.

Abstract

Strontium-90 and Carbon-14 are two important contaminants associated with nuclear waste. Accidental release of these to the environment can cause a hazard which will persist for hundreds or thousands of years.

The coprecipitation of ^{90}Sr and ^{14}C into calcium carbonate has been demonstrated to be a feasible process for the removal of these isotopes from groundwater, achieving over 99.9 % removal for both isotopes. However, there exists a number of potential issues that should be considered before applying this technique to any site. ^{90}Sr and ^{14}C are removed by fundamentally different processes (prolonged Ca^{2+} and TIC depletion respectively). Since these process cannot be achieved in the same solution at the same time the simultaneous removal of these two isotopes to high removal efficiencies is not possible. Furthermore ^{14}C removal displayed a remobilization back to solution, indicating that ^{14}C held in calcite in a solution where there is not a net TIC flux to the precipitate will exchange with TIC in the solution. Sr incorporation into calcite was possible across a range of Sr concentrations and was found to be enhanced by the presence of calcite seed crystals (likely due to sorption to the calcite surface) also toward the end of free drift experiments where strontianite became supersaturated.

Contents

List of Figures

List of Tables

Selected list of symbols and abbreviations

aX	Aqueous activity of X
$[X]$	Aqueous concentration of X
χ_i	Mole fraction of component i
D_X	Berthelot-Nernst Distribution coefficient of X
γ_i	Activity coefficient of component i
γ	Surface free energy/Surface tension (N m^{-1})
G	Molar Gibbs energy
ΔG_m^{xs}	Excess Gibbs free energy of mixing
H	Enthalpy
I	Ionic strength
K_x	Solubility product of X
m_i	Molality of i
μ_i	Chemical potential of i
Ω	Saturation state
$\Sigma\Pi$	Lippmann solubility product
R	Gas Constant
S	Entropy
T	Absolute temperature in Kelvin
U	Chemical potential
z_i	Charge of i

ACC	Amorphous Calcium Carbonate
AFm	Alumina Ferric oxide monosulphate
AFt	Alumina Ferric oxide trisulphate
BSE	Backscattered Electrons
CSH	Calcium Silicate Hydrate
CH	Calcium Hydroxide
CTSR	Continuous Tank Stirred Reactor
DIW	Deionized Water
GGBFS	Ground Granulated Blast Furnace Slag
IAP	Ion Activity Product
Mc	Monocarboaluminate
OPC	Ordinary Portland Cement
SE	Secondary Electron
XRD	X-ray Diffraction

Part I

Introduction and Background

Chapter 1

Introduction

Radioactively contaminated ground and groundwater pose a potential threat to a number of receptors including drinking water resources, human and non-human biota, as well as impacting on the decommissioning of nuclear sites. Neither the scale of the UK contaminated ground and groundwater liability, nor the approach to its future management are fully defined, and as such a range of potential remedial options are required in order to suit individual site circumstances and differing radionuclide characteristics.

Strontium-90 and Carbon-14 are two radionuclides of potential concern observed at the Sellafield site in Cumbria which share a similar distribution in groundwater Stamper et al. (2014). Several techniques exist for the removal of ^{90}Sr from groundwater, each with inherent advantages and disadvantages. To date, the removal of ^{14}C has received less interest however, the scope of ^{14}C contamination is becoming better understood, and its presence in concentrations of up to 50 KBq L^{-1} at the Sellafield site call for an effective remediation technique for this radionuclide.

Ion exchange resins are one of the key technologies currently used to remove ^{90}Sr from

groundwater. Their operation relies on the displacement of weakly bound cations from a matrix by ^{90}Sr ions from the groundwater. This technique is used extensively for remediating nuclear plant effluent as well as treating incoming make-up water. These ion exchange resins can be very effective for the removal of high concentration ions from groundwater; however, their applicability to dilute compounds in groundwater is potentially problematic – owing to the presence of competing ions (Möller et al., 2002). Contaminated groundwater contains $^{90}Sr^{2+}$ ions in concentrations of ng/L-pg/L whereas other divalent metals such as Ca^{2+} and Mg^{2+} are present in mg/L concentrations. The abundance of these groundwater ions can greatly reduce the effectiveness of any proposed treatment scheme based on ion exchange resins, by taking up ion exchange capacity. In addition, anionic contaminants such as $H^{14}CO_3^-$ and $^{14}CO_3^{2-}$ would require a separate anion exchange process – with similar competing ion issues from non-radioactive species.

The substitution of Sr^{2+} into carbonates has been studied by a number of researchers (Kinsman and Holland, 1969; Lorens, 1981; Tesoriero and Pankow, 1996; Mitchell and Ferris, 2005). These studies highlight a number of parameters which may affect the partitioning; including rate of reaction, carbonate polymorph formed, presence of competing ions, and temperature. The affinity of ^{14}C for carbonate precipitates has however received less interest.

This project aims to develop a new remediation technique which will use alkaline carbonate coprecipitation reactions to trap ^{90}Sr and ^{14}C in calcium carbonate precipitates. This technique would have the benefit of using low cost, readily available sources of Ca; in the form of slaked lime ($Ca(OH)_2$) or gypsum ($CaSO_4$). This should greatly

reduce the cost of this treatment scheme and potentially make it more favourable than relatively expensive synthetic ion exchange resins.

This research aims to better understand the incorporation mechanisms of ^{90}Sr and ^{14}C into carbonates with the goal of identifying the optimal conditions, reasonably achievable for an industrial technique, for the coprecipitation of ^{90}Sr and ^{14}C into carbonates; and use this information to design a large scale remediation technique.

1.1 Objectives

1. Determine the effect of varying initial solution concentrations of Ca and CO_3^{2-} on the distribution coefficients of Sr and ^{14}C into calcium carbonate. This will be achieved by carrying out a series of batch alkaline coprecipitation experiments with varying initial concentrations of $Ca(OH)_2$ and Na_2CO_3.

   (b) Establish the importance of atmospheric CO_2 in-gassing on the above reaction. This will be achieved by repeating the batch alkaline coprecipitation experiments in sealed reactions vessels, with minimal head-space.

2. Determine the effects of changing groundwater ionic content on the distribution coefficients of Sr and ^{14}C into calcium carbonate. This will be achieved by carrying out a series of batch alkaline coprecipitation experiments with varying ionic content; including (Mg^{2+} and SO_4^{2-}).

3. Develop a kinetic model in PHREEQC which is capable of understanding changing solution calcium, TIC, pH and mineralogy during carbonate precipitation. As well as the partitioning of Sr and ^{14}C into the precipitate.

4. Investigate whether the addition of seed crystals will improve the distribution coefficients of Sr and ^{14}C into calcium carbonate.

5. Probe the strontianite-calcite solid solution with a series of constant composition experiments to better understand the mechanism of Sr incorporation into calcite.

6. Determine the stability of radio-carbonate powders in cement waste forms, and understand the fate of ions from any calcite which dissolves. This will be achieved by mixing radio-carbonate into a series of cement blends.

Thesis outline

This dissertation will comprise an Introduction in Chapter 1. A literature review in Chapter 2. This will be followed by a discussion of research methodology used in this study, including analytical techniques, method development, and sampling strategy in Chapter 3. Experimental data Chapters are included in Chapters 4-7, and subsequently concluded in Chapter 8.

Chapter 4 - Reaction kinetics and recrystallization pathways

The first data chapter discusses work carried out to understand the removal of Sr and ^{14}C from a series of batch coprecipitation experiments carried out under alkaline conditions. Modelling in PHREEQC was also completed to better understand key trends.

Key findings

- 99.7% of ^{14}C and 98.6% of Sr removed from aqueous solution by CaCO3 precipitation
- Remobilization of ^{14}C observed during calcium carbonate recrystallization
- Sr displayed variable distribution coefficient (possibly affected by Ca:Sr ratio)
- Reagent cost of $0.22/m3 of treated groundwater.

Reference - David J. Hodkin, Douglas I. Stewart, James T. Graham, Ian T. Burke (2016) Coprecipitation of ^{14}C and Sr with carbonate precipitates: The importance of reaction kinetics and recrystallization pathways, Science of The Total Environment, Volume 562

Chapter 5 - Potential amendments to the Carbonate precipitation scheme

The second data chapter includes potential mechanisms for improving the coprecipitation of Sr and ^{14}C into calcium carbonate. These includes using SO_4 and increased temperature (40°C) to favour aragonite precipitation as well as using seed crystals to prevent the recrystallization pathways affecting the reaction in section 1.1.

Key findings

- Under high pH conditions the precipitation of aragonite is unfavourable and not a suitable mechanism for improving Sr coprecipitation into calcite.
- High seed crystal surface areas are beneficial for the removal of Sr and ^{14}C from solution.

Chapter 6 - Enhanced Crystallographic incorporation

This section aims to better understand the Calcite-Strontianite solid solution. At a fixed precipitation rate the amount of Sr incorporated into calcite was increased by altering the solution Ca/Sr ratio. This generated a range of carbonate precipitates with varying Wt. % Sr.

Key findings

- The distribution coefficient of Sr into calcite is independent of the Sr/Ca ratio in the solution and, under the conditions of the experiment, was 0.15.

- Calcites were precipitated with 0.02-9.47 Wt. % Sr. These precipitate displayed an increasing disorder with Sr Wt. %.
- Sr^{2+} is preferentially adsorbed to obtuse growth steps and generates an increase in the L/W ratio of precipitates.

Chapter 7 - Waste-form stability

The planned disposal route of the radioactive calcium carbonate generated by this treatment scheme would be through mixing into cement grout waste forms. The fate of ^{90}Sr and ^{14}C in cement blends will be tested, with implications for long term stability and weathering properties.

Key findings

- ^{14}C is most likely incorporated in the Monocarboaluminate phase.
- ^{90}Sr was not found at concentrations above the LOD. This suggests that it is most likely incorporated diffusely throughout the sample.
- Cement blends with higher proportions of OPC relative to GGBFS favour the dissolution of calcite

Bibliography

Kinsman, D.J.J., Holland, H.D. (1969). The co-precipitation of cations with CaCO3—IV. The co-precipitation of Sr2+ with aragonite between 16° and 96°C. *Geochimica et Cosmochimica Acta*, **33**(1), pp. 1–17.

Lorens, R.B. (1981). Sr, Cd, Mn and Co distribution coefficients in calcite as a function of calcite precipitation rate. *Geochimica et Cosmochimica Acta*, **45**(4), pp. 553–561.

Mitchell, A.C., Ferris, F.G. (2005). The coprecipitation of Sr into calcite precipitates induced by bacterial ureolysis in artificial groundwater: Temperature and kinetic dependence. *Geochimica et Cosmochimica Acta*, **69**(17), pp. 4199–4210.

Möller, T., Harjula, R., Lehto, J. (2002). Ion exchange of 85Sr, 134Cs and 57Co in sodium titanosilicate and the effect of crystallinity on selectivity. *Separation and Purification Technology*, **28**(1), pp. 13–23.

Stamper, A., Coughlin, D., Bowes, A., Ruddick, P., Laws, F. (2014). Groundwater Monitoring at Sellafield Annual Data Review 2013. Technical Report LQRD000077, Sellafield Ltd.

Tesoriero, A.J., Pankow, J.F. (1996). Solid solution partitioning of Sr2+, Ba2+, and Cd2+ to calcite. *Geochimica et Cosmochimica Acta*, **60**(6), pp. 1053–1063.

Chapter 2

Background Information and Theory

The Sellafield site in Cumbria (Figure 2.1) has had a long nuclear history dating back to 1947 when the plutonium producing Windscale piles were commissioned, followed by Calder Hall, the worlds first nuclear power plant in 1956. Calder Hall was a Magnox reactor, named for the Magnesium oxide alloys used to clad the Uranium fuel elements. This design was favoured throughout the 1950s-60s with a total of 11 operational reactors built. Currently the UK nuclear portfolio comprises of six Advanced Gas Reactors (AGR) alongside a Pressurised Water Reactor (PWR) at Sizewell B and an European Pressurized Reactor (EPR) under development at Hinkley point C (World Nuclear Association, 2016).

Alongside this rich history of Nuclear power generation, the UK is host to the Sellafield Nuclear reprocessing facility. Sellafield has operated as a nuclear facility since 1947 when the Windscale Piles were created as part of the UK's atomic weapons program, alongside a plutonium extraction plant. In 1956 the Calder Hall nuclear reactor was commissioned (named for the river running through the site), as well as reprocessing

facilities designed to tackle Magnox and Oxide fuel. Calder hall was closed in 2003 and the site currently operates exclusively as a reprocessing facility, receiving waste streams from several countries (Baldwin, 2003; Reeve and Eilbeck, 2007).

During nuclear power generation it is possible for a wide variety of radioisotopes to be generated depending on the process type and materials present. Due to the diverse range of materials taken in by Sellafield it hosts a wide array of radionuclides (^{3}H, ^{14}C, ^{60}Co, ^{90}Sr, ^{95}Zr, ^{95}Nb, ^{99}Tc, ^{106}Ru, ^{129}I, ^{134}Cs, ^{137}Cs, ^{144}Ce, ^{237}Np, ^{241}Pu, ^{241}Am, ^{243}Cm, ^{244}Cm, and Uranium) (Defra, 2002). The aim of Sellafield is to take in these waste streams, and concentrate their radionuclides in a stable waste form which can be returned to the customer. Since 1952 Sellafield has been authorised to emit radionuclides to the Irish sea. Peak emissions were reached in the mid 1970s with over 8000 TBq yr^{-1} being discharged (Baldwin, 2003). Since then Sellafield has made a significant effort to reduce these emissions, with a swift decline achieved throughout he early 1980s (Cook et al., 1997). In addition to these authorised emissions a number of accidental leaks have occurred throughout the sites history.

The Magnox Swarf Storage Silo (MSSS) is a facility at Sellafield used as storage for the Magnesium oxide cladding (swarf) used in the fuel elements of the UK's historic Magnox plants. Within the silos the swarf is stored submerged in water for heat regulation and shielding. The magnesium rich swarf reacts with this water to produce hydrogen gas and $Mg(OH)_2$ which has buffered the solution to a high pH (Fairhall and Palmer, 1992). This high pH solution caused corrosion of the concrete tank base below ground level, resulting in the release of a high pH plume to the local groundwater. The corrosion of the tank is believed to have self-sealed by tank sludge and precipitates

however the potential for these fractures to reopen is acknowledged which may result in future leaks (Reeve and Eilbeck, 2007; Garrard et al., 2016).

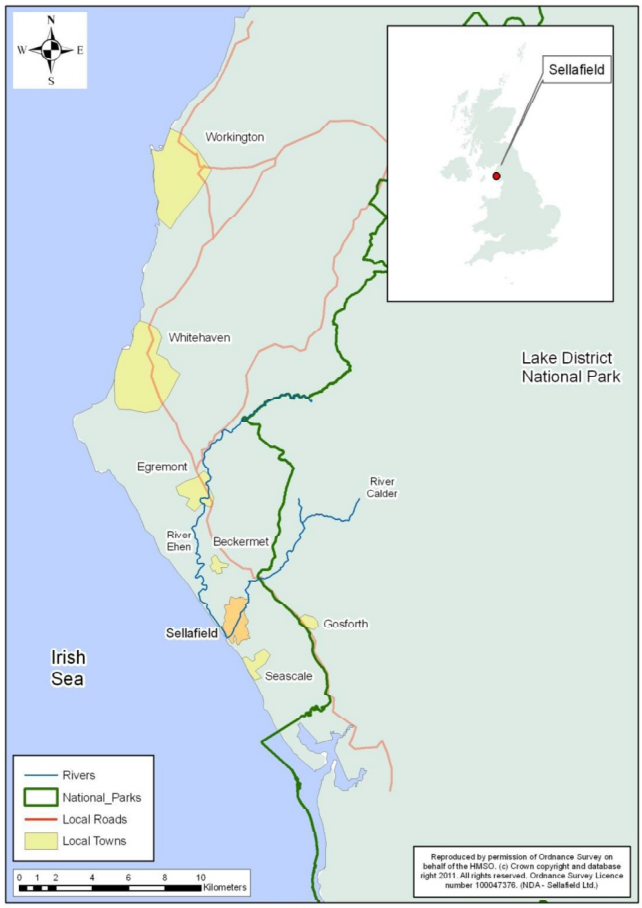

Figure 2.1: Sellafield location from (Cruickshank, 2012)

2.1 Sellafield Site characterization

Since the scope of nuclear contamination at Sellafield was discovered a significant effort has been made to understand the nature and extent of the contamination present under the Sellafield site (Cruickshank, 2012).

In April 2001 a six year Phase 1 investigation into the contamination levels under

Sellafield commenced, called the Sellafield Contaminated Land Study (SCLS) (El-Ghonemy, 2004). This was followed by a Phase 2 investigation in April 2007 which was completed in August 2010 (Cruickshank, 2012). In 2011 Sellafield began a series of annual groundwater monitoring rounds to track and delineate groundwater contamination. This section will aim to give a summary of these reports within the context of ^{90}Sr and ^{14}C contamination at Sellafield.

Geology

The first layer encountered in the Sellafield profile is made ground, installed during the site's construction. This is reported to be < 3 m thick, but may be thicker alongside to the river Calder.

The made ground is underlain by drift deposits laid down during the Quaternary glaciation. Sands, gravels and silts make up these deposits which vary in their relative proportion due to the diverse range of material brought down the glacial valleys. These glacial sediments form channels, one of which underlies the Separation area with a maximum depth of 60 m.

The Quaternary geology is underlain by the Triassic Sherwood Sandstone, comprised of the Wilmslow and Helsby formations. These both are reddish Aeolian sandstones with significant surface weathering (Cruickshank, 2012; Stamper et al., 2014).

Hydrology

Groundwater was encountered at between 3-12 m bgl in the separation area. This wide range of groundwater depths is a result of a mound of groundwater centred on the

separations area. This mound is likely the result of slow leakage into low permeability drift layers.

Groundwater flow through the sandstone unit was found to be, at least partially, controlled by fracture networks which, coupled with the multiple sandstone units, leads to significant heterogeneity in the groundwater flow characteristics (El-Ghonemy, 2004). A buried channel situated under the site adds further complexity to flow characteristics (Figure 2.2).

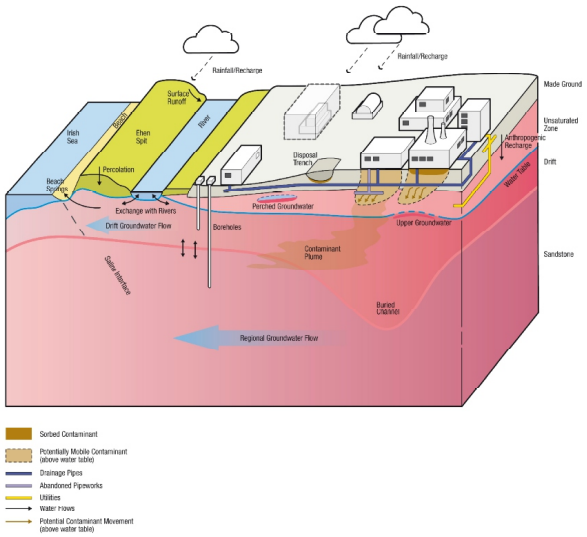

Figure 2.2: A section illustrating the geology and hydrology underlying Sellafield from (Cruickshank, 2012)

Groundwater monitoring

Groundwater samples taken during the annual groundwater monitoring rounds have consistently identified, among others, a zone of beta contamination in groundwater extending from the SW of the separation area (Figure 2.3)(Stamper et al., 2014). In this groundwater ^{90}Sr was found to be the dominant beta emitting radionuclide, with maximum concentrations observed in monitoring well 10087. A concentration of 75.3

KBq L−1 was observed in 2011, followed by an increase to 77.1 KBq L−1 in 2012, and a decrease to 44.2 KBq L−1 in 2013. The same monitoring well (10087) also displayed the maximum concentrations of ^{14}C. ^{14}C displayed a similar behaviour to ^{90}Sr; a concentration of 47.4 KBq L^{-1} was observed in 2011, followed by an increase to 53 KBq L^{-1} in 2012, and a decrease to 44.2 KBq L−1 in 2013. These peak beta concentrations coincide geographically with a historic leak associated with a storage silo recorded in this area in 1979 (Stamper et al., 2014).

Other concentrations of ^{90}Sr have been observed towards the NE of the separation area in well 10202, at a maximum concentration of 8.2 KBq L^{-1} again co-located with the maximum ^{14}C concentration of 6.3 KBq L^{-1}. Although significantly lower than concentrations observed in well 10087 at the SW of the separation area, these concentrations exceed the WHO drinking water guidelines of 0.001 and 0.100 Bq L^{-1} for ^{90}Sr and ^{14}C respectively. Both wells are situated in the Drift deposits underlying the sites.

Carbon-14 in the environment

Carbon-14 is a relatively weak β emitting isotope (maximum 0.156 MeV, average 49 KeV). It has a half-life of 5730 years and, due to its central role in the structure of organic molecules, it may become incorporated in organic matter. In UK power stations (AGR and Magnox) ^{14}C is produced by reactions involving C, N and O within the coolant, graphite moderator, core structural materials and fuel (Eq. 2.1 - 2.3) (Yim and

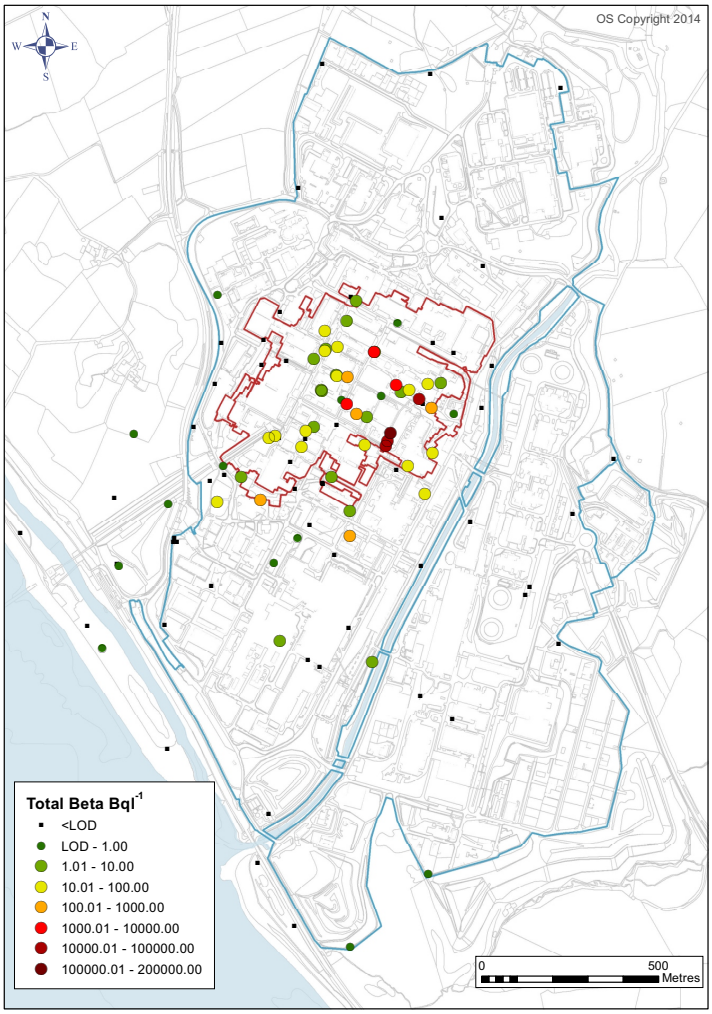

Figure 2.3: Extent of Beta contamination in Sellafield groundwater from (Stamper et al., 2014)

Caron, 2006).

$$^{13}_{6}C + ^{1}_{0}n \rightleftharpoons ^{14}_{6}C + \gamma \tag{2.1}$$

$$^{14}_{7}N + ^{1}_{0}n \rightleftharpoons ^{14}_{6}C + ^{1}_{1}p \tag{2.2}$$

$$^{17}_{8}O + ^{1}_{0}n \rightleftharpoons ^{14}_{6}C + ^{4}_{2}\alpha \tag{2.3}$$

The fate of this ^{14}C depends on the environment it is generated in. Carbon-14 generated in the coolant will be present as $CO_{2(g)}$ and be released to the atmosphere. Carbon-14 generated in the graphite moderator may be retained until decommissioning takes place and ^{14}C generated in the fuel and cladding will pass to a reprocessing plant, such as Sellafield (Bush et al., 1984).

When leaked to the groundwater this ^{14}C, commonly present as $H^{14}CO_3$ may react with Ca to precipitate as calcium carbonate. Boylan et al. (2016) found that at Sellafield this may be controlling ^{14}C concentration in the groundwater near the leak zone

Strontium-90 in the environment

Strontium-90 is a fission product which is concentrated in reactor core materials and the fallout from nuclear weapons testing. It has a half-life of 28.8 years producing a β emission with a maximum energy of 0.546 MeV and an average energy of 0.196 KeV. It also has a short lived daughter isotope ^{90}Y (64.2 h) in its decay chain.

Strontium-90 can become incorporated in living organisms through substitution for Ca in the bones (Kulp and Schulert, 1962). A study investigating the distribution of ^{90}Sr in teeth and bone from Greece observed an average concentration of Sr^{90} of ~30 mBq g^{-1}

across 105 samples as a result of nuclear weapons testing and the Chernobyl accident (Stamoulis et al., 1999).

Under circumneutral-alkaline pH conditions and ionic strength around 10 mM, ^{90}Sr is readily adsorbed to the surface of common soil minerals. As pH or ionic strength rises ^{90}Sr will desorb and return to the solution (Wallace et al., 2012). This makes its presence in ground water a particular concern as it will remain immobile until a rise in pH or ionic strength e.g. due to a saline intrusion mobilises it.

2.2 Summary of Remediation Options

With more known about the site conditions and contamination present Sellafield commissioned a series of reports into potential treatment and management strategies. The main treatment strategies investigated were Permeable Reactive Barriers (PRB), In-Situ Manipulation (ISM), and Pump and Treat.

2.2.1 Permeable Reactive Barrier (PRB)

PRBs have been successfully installed in a number of areas to treat a range of groundwater contaminants (Benner et al., 1999; Barton et al., 2004). They operate by intercepting groundwater flow and creating localised chemical conditions (often within 1-2 m) which enable the contaminants to be precipitated, adsorbed or broken down. PRBs may take the form of trenches filled with the PRB material or Funnel and gate systems which consist of impermeable funnels channelling the groundwater flow to the gate area which comprises of the PRB material, this enables less PRB material to be used (Palmisano

and Hazen, 2003). Their construction also allows for more engineered gate systems wherein the gate fill material can be extracted and replaced as it becomes spent, the leak changes or a better material becomes available (Cummins et al., 2016).

One of the fundamental requirements of a PRB is that the groundwater flow containing the contaminants be fully intercepted by the barrier. Due to the lack of a low permeability layer at depth at Sellafield there exists the potential for groundwater to flow under the PRB rather than through it, particularly in areas where the groundwater flow is being retarded e.g. the funnel region. Detailed hydrological modelling was carried out to attempt to determine optimal operating conditions to minimise around flow however due to the complex anisotropic hydrology in the area there exists the potential for modelling errors.

The barrier fill material may vary depending on the contaminant to be treated. Zeolite and Apatite were both identified as potential fill materials for the remediation of ^{90}Sr, achieving 99.9% removal of ^{85}Sr (used as a surrogate for ^{90}Sr). These remove the Sr through sorption and are therefore unlikely to remove anionic species such as ^{14}C.

While PRBs could provide a long term passive remediation technique their application at Sellafield is problematic due to the uncertainties in local hydrology and potential logistical issues with the access require to install a PRB.

2.2.2 In-Situ Manipulation (ISM)

The goal of ISM is similar to that of PRB however instead of creating an engineered barrier to groundwater flow ISM relies on the injection of the material into groundwater.

This makes it a less invasive technique requiring the drilling of boreholes rather than trenches. It also minimises potential worker exposure to contaminants by leaving them in the subsurface. A successful ISM using an Apatite slurry was applied to ^{90}Sr at the Hanford site, USA (Szecsody et al., 2007) . A two stage injection of a low then high concentration of Ca-citrate-PO_4 solution was used to initiate in-situ precipitation of apatite whilst minimising the potential remobilization of ^{90}Sr due to the influx of high ionic strength solution.

Potential materials identified for borehole treatment of ^{90}Sr include apatite, zeolite, and Granulated Activated Carbon for adsorption (as in the the PRB) as well as the in-situ precipitation of apatite potentially resulting in coprecipitation and adsorption. These materials were found to offer a viable removal of ^{90}Sr from the groundwater and due to the relative ease of installation and proof of concept at the Hanford site this poses an attractive treatment option (Lancefield et al., 2016).

A potential drawback of this treatment scheme is the inability of it to remove ^{14}C. It is possible that in-situ precipitation of calcium carbonate could remove ^{90}Sr as well as ^{14}C from the groundwater however this remains to be tested (Mitchell and Ferris, 2005).

2.2.3 Pump and Treat

By pumping the contaminated groundwater to the surface more precise treatment conditions can be achieved. The SIXEP plant was commissioned in the 1970s to treat effluent from the various storage ponds on site. It is based on a zeolite matrix (clinoptilolite) to which the contaminants ($^{134/137}$Cs and ^{90}Sr) are adsorped. The application of the SIXEP clinoptilolite to contaminated groundwater has been considered however, due

to the high ionic content of the groundwater it would have to softened by carbonate precipitation first to remove ions which would otherwise compete for sorption space on the clinoptilolite matrix.

What remains unclear is how the softening stage would affect the contaminant profile. The coprecipitation of Sr into calcium carbonate proceeds largely due to the similarities between the ionic radius and charge of the Sr^{2+} and Ca^{2+} ions. Furthermore the simultaneous removal of ^{14}C through isotopic exchange with the $^{12}CO_3^{2-}$ may occur, simultaneously removing both contaminants. The product from this treatment (a radioactive carbonate powder) should be compatible with a cement grout, enabling a stable waste form to be produced.

The carbonate coprecipitation occurring during the softening stage may be sufficient to remove the contaminants below the desired limits. Should any radioisotopes remain a polishing stage comprising of a cation exchange media (such as the SIXEP clinoptilolite) could be applied, significantly reducing the volume of this more expensive material required.

2.3 Thermodynamics

Thermodynamics uses the state properties of a system to understand it's most stable endpoint. It is therefore very useful for understanding the equilibrium position of a system, and precipitates likely to form therein.

2.3.1 Internal energy (U)

The internal energy (U) of a system is equal to the sum of all the kinetic and potential energies of the components of that system. The first law of thermodynamics states that energy is conserved and if energy is lost by a system it will be gained by its surroundings through the completion of work or the exchange of heat (Eq. 2.4 where q is heat and w is work) (Kapel, 2011).

$$\Delta U = q + w \tag{2.4}$$

Transforming the system from state A to state B will result in a change in the internal energy. If the change is negative the transformation will occur spontaneously giving out energy to its surroundings. If it's positive an energy barrier exists which must be overcome through the assimilation of energy from the systems surroundings (Eq. 2.5) (Smith, 1990).

$$\Delta U = U_B - U_A \tag{2.5}$$

Chemical systems may do work by changing their pressure and volume. Assuming the system is open to atmosphere there will be no change in pressure and a useful way of quantifying this is to remove the work term of Eq. 2.4 and replace it with one that quantifies this expansion Eq. 2.6, where q_P is the heat content of a system (Smith, 1990).

$$\begin{aligned} \Delta U &= q + w \\ \Delta U &= q_P - P(V_B - V_A) \end{aligned} \tag{2.6}$$

Chemical Potential (μ)

The chemical potential (μ) is one of the potential energies that make up the total internal energy of a system. It is defined as the ΔU when 1 mole of a substance is added to the system.

$$\begin{aligned} \mu &= \left(\frac{dU}{dn}\right) \\ \Delta U &= TdS - PdV + \mu dn \end{aligned} \tag{2.7}$$

2.3.2 Enthalpy (H)

The change in heat content of a system (q_P) may be quantified by another state property termed Enthalphy (ΔH) Eq. 2.8. A chemical reaction that gives off heat energy to its surroundings is exothermic and has a $\Delta H < 0$, whereas a chemical reaction that takes in heat energy from its surroundings is endothermic and has a $\Delta H > 0$.

Enthalpy alone is not enough to determine if a chemical reaction is favourable and will happen spontaneously or unfavourable and requires energy. The entropy of the reaction must be understood.

$$\begin{aligned} H &= U + PV \\ \Delta H &= (U_B - PV_B) - (U_A + PV_A) \end{aligned} \tag{2.8}$$

2.3.3 Entropy (S)

Entropy is a measure of the disorder of a system, which for perfectly ordered crystalline solids is zero at 0 K. The second law of thermodynamics states that entropy of a system will increase, resulting in the dispersal out of energy rather than its concentration. In a closed system the point at which the maximum entropy has been reached the system is said to be at equilibrium.

Transforming the system from state A to state B will result in a change in the entropy. This is determined by integrating the quotient of the heat absorbed by the system and the Temperature under which it occurred (Smith, 1990).

$$\Delta S = \int_A^B \frac{dH}{T} \tag{2.9}$$

The formation of a precipitate (such as $CaCO_3$) will result in a localised decrease in entropy, due to the ordering of energy into chemical bonds. Therefore this must be accompanied by a increase in entropy elsewhere in the system. This is achieved through the emission of heat and through the release of hydration water.

2.3.4 Gibbs Free Energy (G)

A spontaneous reaction must either decrease the enthalpy of a system or lead to an increase in it's entropy. The Gibbs free energy of a system is a state function that uses the enthalpy and entropy of a system, along with it's temperature, to determine the energy available for reactions to take place.

$$G = H - TS \tag{2.10}$$

If the ΔG of a reaction is negative it is favourable and will proceed without requiring extra energy. If the ΔG of a reaction is positive it is unfavourable and will require the addition of energy from outside the system. This is therefore a useful tool for understanding the most stable energy state for a chemical system and thus its equilibrium position. In solids the entropy component of a components free energy is small due to the high degree of order, however, the enthalpy is negative and large due to the strong bonds formed between the atoms (Smith, 1990).

2.3.5 Law of Mass Action

At equilibrium the concentration of various phases is calculated through the law of mass action Eq. 2.11. The relationship between the products and the reactants can then be quantified by an equilibrium constant Eq. 2.11b. Because the activity of a solid is 1 the concentrations of Ca^{2+} and CO_3^{2-} in equilibrium with $CaCO_{3(s)}$ can be calculated by Eq. 2.11c. This value is the concentration threshold at which aqueous Ca^{2+} and CO_3^{2-} ions will begin to react to form $CaCO_{3(s)}$.

$$aCa^{2+} + aCO_3^{2-} \rightleftharpoons CaCO_{3(Cal)} \tag{2.11a}$$

$$K_{Cal} = \frac{aCa^{2+} \times aCO_3^{2-}}{aCaCO_3} \tag{2.11b}$$

$$K_{Cal} = 10^{-8.48} = aCa^{2+} \times aCO_3^{2-} \tag{2.11c}$$

If the activities of Ca and CO_3 at which calcium carbonate is known to precipitate as Eq. 2.11c then it is possible to determine how close a solution is to precipitating a given phase by calculating the Ion Activity Product (IAP) Eq. 2.12a and dividing this by the K value from Eq. 2.11c to obtain the saturation state (Eq. 2.12b). This is often converted to a saturation index (2.12c) by taking the log of the Ω. A solution with a saturation index of 0 is in equilibrium with any solid phase present. If the SI is greater than 0 a precipitate may form and conversely if the SI is less than 0 any precipitate may dissolve.

$$IAP = aCa^{2+} \times aCO_3^{2-} \tag{2.12a}$$

$$\Omega = IAP/K \tag{2.12b}$$

$$SI = \log(\Omega) \tag{2.12c}$$

2.3.6 Non-Ideal solutions

Equation 2.11 uses the activity of aqueous ions rather than their concentration. The aqueous activity of an ion differs from its concentration in solution due to the effects of

shielding by water molecules and interaction with ions in solution. The Debye-Hückel relation is commonly used to correct for these effects. First the ionic strength of the solution is calculated by Eq. 2.13a. Then the ionic strength is used to calculate the activity coefficient by Eq. 2.13b, where A and B are temperate dependent constants, and $\dot{a}_i$ is the empirical ion-size parameter of ion i. This relation only holds true for solution with I<0.1.

$$I = {}^1/_2 \Sigma m_i \times z_i^2 \tag{2.13a}$$

$$\log \gamma_i = -\frac{A z_i^2 \sqrt{I}}{1 + B\dot{a}_i \sqrt{I}} \tag{2.13b}$$

In addition to the effects of shielding by water molecules and ion association, corrected for through activity coefficients, ions may form complexes in solution which will lower their activity. The formation of these complexes can be modelled using the law of mass action, in a similar way to the formation of compounds. The total solution Ca concentration can then be calculated by summing the Ca bearing complexes throughout the solution.

2.4 Carbonate equilibria

The term carbonate refers to the $CO_3{}^{-2}$ ion, however it is also commonly used to refer to the whole group of minerals which are comprised of a carbonate ion bound to a divalent metal ion (M^{2+}) i.e. MCO_3. A wide variety of carbonate species can form

with various metal ions binding to one or more CO_3^{2-} ions (Ca, Mg, Mn, Fe, Zn, Sr, Cd, Ba, Pb), the most common of these species is calcium carbonate ($CaCO_3$) (Appelo. and Postma., 2007). Carbonates have importance across a range of research areas; it is one of the main minerals used in nucleation studies (Nilsson and Sternbeck, 1999; Gebauer et al., 2008; Nielsen et al., 2014), its chemical and isotopic signatures can be used to probe paleoclimatic conditions (Fairchild et al., 2006), it is used as a drug carrier (Wei et al., 2008), as well as a potential phase to remove contamination from solution (Mitchell and Ferris, 2005).

When there is an interface present between a solution and a gas containing CO_2 (such as the atmosphere) diffusion of CO_2 will take place across the interface until an equilibrium has been established. If the solution is under-saturated with respect to CO_2 atmospheric $CO_{2(g)}$ dissolves to form $CO_{2(aq)}$. This process is dependent on temperature and pressure and is calculated by Henry's law. Equation 2.14 shows the concentration of $CO_{2(aq)}$ in equilibrium with the atmosphere at 20°C.

$$\begin{aligned} [CO_{2(aq)}]^{eq} &= \kappa_H \times P_{CO2} \\ [CO_{2(aq)}]^{eq} &= 0.032 \times 4 \cdot 10^{-4} \\ [CO_{2(aq)}]^{eq} &= 0.0128\ mmol\ L^{-1} \end{aligned} \tag{2.14}$$

Aqueous CO_2 reacts in water to form carbonic acid (H_2CO_3) which may in turn dissociate into bicarbonate (HCO_3^-) and carbonate (CO_3^{2-}). This speciation is dependent on solution pH, the equilibria between these carbonate species is detailed in Table 2.1. These equilibria enable the speciation of solution TIC across a range of pH conditions

to be calculated, this information is plotted in Fig. 2.4. Under alkaline conditions (pH>10.3) CO_3^{2-} becomes the dominant phase of dissolved inorganic carbon (Appelo. and Postma., 2007).

In solution $CO_{2(aq)}$ is significantly more abundant than H_2CO_3 and due to the relatively rapid conversion from $CO_{2(aq)}$ to H_2CO_3 these two species are commonly summed under the name $H_2CO_3^*$.

The speciation of TIC towards carbonate at high pH has important implications for calcium carbonate precipitation, due to its reliance of the aqueous activity of CO_3^{2-}.

Table 2.1: Equilibria of the 3 key carbonate species

Reaction	Equilibria
$CO_{2(g)} + H_2O \rightleftharpoons H_2CO_3$	$K_H = [H_2CO_3^*]/P_{CO_2} = 10^{-1.5}$
$H_2CO_3 \rightleftharpoons HCO_3^- + H^+$	$K_1 = [H^+][HCO_3]/[H_2CO_3] = 10^{-6.3}$
$HCO_3^- \rightleftharpoons CO_3^{2-} + H^+$	$K_2 = [H^+][CO_3^{2-}]/[HCO_3^-] = 10^{-10.3}$

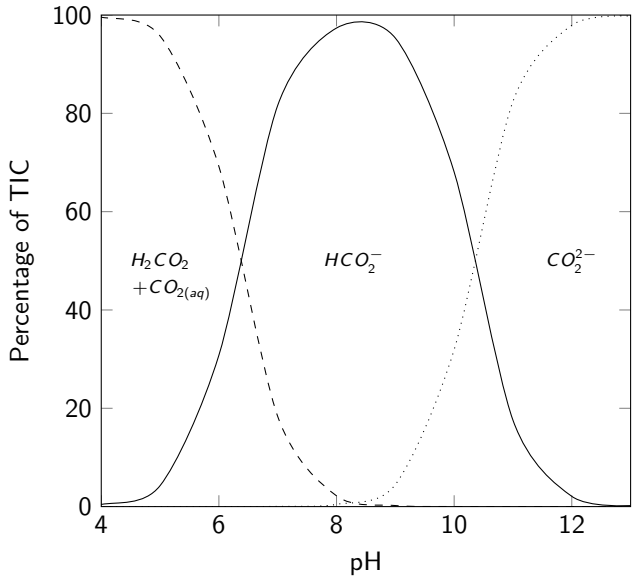

Figure 2.4: Carbonate speciation dependence on pH

Calcium ions in solution will form dative covalent bonds with the electron pair on the Oxygen atoms contained in water molecules (Dorvee and Veis, 2013). This results in a

hydration shell of water molecules surrounding Ca^{2+} ions in solution.

The degree of hydration of an aqueous ion can be approximated by the formula (Richens, 1993)

$$\Delta H^{\theta}_{hyd} = \frac{-69500 \cdot Z^2}{r_{eff}} \tag{2.15}$$

2.5 Nucleation Theory

When a solution becomes supersaturated with a phase the nucleation and growth of this phase may occur. There exists much debate regarding the mechanism through which solution ions interact to form a solid phase. One of the frameworks commonly used is Classical Nucleation Theory (CNT).

2.5.1 Classical Nucleation Theory (CNT)

CNT stems from the work of (Gibbs, 1878; Volmer, 1939; Stranski, 1928; Becker and Döring, 1935; Burton et al., 1951). It uses the difference in the chemical potential of the species in solution and in the nascent phase as the driving force behind nucleation Eq. 2.16 (Mullin, 1972; Benning and Waychunas, 2008). When the chemical potential of the solute becomes greater than that of the molecules in the solid phase it will become energetically favourable for a precipitate to form.

$$\Delta\mu_{CaCO_3} = \mu_{CaCO_3(s)} - \mu_{CaCO_3(aq)} \tag{2.16}$$

$\mu_{CaCO_3(ppt)}$ is the chemical potential of the calcium carbonate in the precipitate

$\mu_{CaCO_3(s)}$ is the chemical potential of the calcium carbonate in the solution.

A crystal nucleating from a solution will generate a decrease in free energy proportional to the change in chemical potential ($\Delta\mu$) and the number of molecules in the crystal lattice (n). The same crystal will generate free energy due to the production of an interface between the solution and the crystal lattice (Eq. 2.17). This interface will have a free energy (γ), which combined with the total surface area (for a cube $6a$) present will give the total free energy generated during nucleation (ΔG_n) (Mullin, 1972; Vekilov, 2010).

This shows that small crystals (sub-critical nuclei) are energetically unfavourable due to their high surface area:volume, however past a certain threshold the volume energy becomes dominant and crystals will readily grow. Crystals that reach this critical size are termed critical nuceli.

$$\begin{aligned} \Delta G_S &= -n\Delta\mu \\ \Delta G_V &= 6a^2 n^{2/3}\gamma \\ \Delta G_n &= \Delta G_S + \Delta G_V \end{aligned} \tag{2.17}$$

A study by Sleutel et al. (2014) observed nucleation of glucose isomerase on the surface of a Mica crystal. This paper produced an image of ion clusters ranging in size from 1->50 molecules. These ion clusters maintain a consistent lattice structure throughout their nucleation and growth, displaying clear molecule by molecule growth consistent

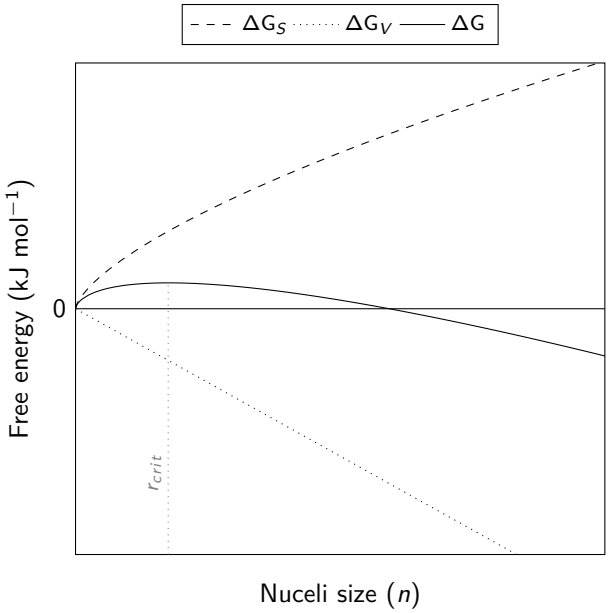

Figure 2.5: Visualisation of the free energy associated with nucleus formation

with CNT (Fig. 2.6).

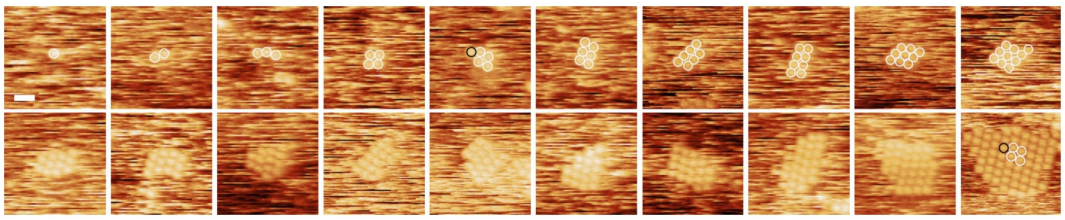

Figure 2.6: AFM images of glucose isomerase clusters varying in size taken from Sleutel et al. (2014)

Assailing the energy barrier

Sub-critical nuclei are unstable and must grow to reach critical size. They are able to do this through two mechanisms, hetrogenous and homogenous nucleation.

Most solutions contain surfaces either from seed crystals isostructual with the nucleating phase, foreign particles such as dust, and even the walls of the a reaction vessel. These surfaces may reduce the inhibitory effect of the surface energy term and allow precipitation at lower supersaturations.

In solutions absent of seed crystals a sub-critical nucleus may still reach the required size to become stable. This is possible due to localised fluctuations in the free energy of the system. This suggests that nucleation is a fundamentally probabilistic process which depends on enough ions colliding in a favourable energy environment to form a critical nucleus. The more constituent ions of the nucleating phase in solution the more likely they are to collide and precipitate (Gibbs, 1878; Mullin, 1972).

LaMer and Dinegar (1950) found that the concentration of a solute may increase past the solubility threshold to a critical limiting supersaturation, at which the nucleation of a precipitate will occur. After this point the concentration of the solute will decrease until the solubility limit is reached (Fig. 2.7).

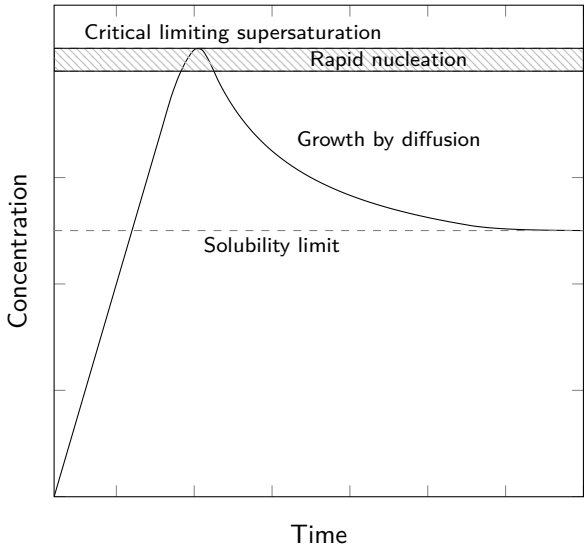

Figure 2.7: La Mer Nucleation plot

Ostwald rule of stages

While a system will seek to reach an endpoint with the lowest free energy, which in the case of the calcium carbonate system is normally calcite (at room temperature and

pressure). It may reach this end point by passing through a myriad of intermediate reaction products (Ostwald, 1897). However, this rule is largely based on observation and does not have a mathematical foundation (Hedges and Whitelam, 2011).

Non-Classical crystallization

Real world nucleation has proven more complex than CNT would suggest. The exact mechanism of nucleation is is a matter of debate but certainly depends on the composition of the precipitating solution. Gebauer et al. (2008) found evidence of stable ion clusters of a sub-critical radius, this is inexplicable within the framework offered by CNT. Pre-nucleation clusters were first identified in a series of constant addition experiments. These experiments found that calcium and carbonate ions were binding as solute clusters prior to the nucleation of a precipitate. Since then these structures have gained significant interest due to their key role in the early stages of nucleation, with cryo-TEM images backing up Gebauer's initial findings (Pouget et al., 2009).

These prenuleation clusters accompany new growth mechanisms, such as growth by the orientated attachment of nano-crystals isostructural with the final mineral (Song and Cölfen, 2010), and growth by the aggregation of amorphous precursors non-isostructural with the final mineral such as the ACC-Vaterite-Calcite transition (Rodriguez-Blanco et al., 2011). The formation of prenucleation clusters increases with supersaturation, thus for a given Ca and TIC concentration the formation of prenucleation clusters increases with pH due to increased TIC speciation as carbonate (Gebauer and Cölfen, 2011)

Nucleation summary

In summary, crystals form through the agglomeration of ions in solution. Below a certain size these ions are unstable and will break apart. However, due to localised energy fluctuations it is possible for a nucleus to gain the energy required to reach the critical size. The SI is the threshold at which the concentration of the ions in solution is great enough that collisions and resultant bond forming are rapid enough to overcome the energy barrier for nucleation (Debenedetti, 1996). In recent years evidence has come to light of nucleation mechanisms that don't fit into this framework, termed non-classical nucleation theory. This theory suggests that stable ion clusters of a sub-critical size are possible and may contribute to nucleation through non-classical pathways, such as through amorphous precursors or agglomeration of nanocrystals.

Growth

If the formation of a critical nucleus can be thought of as the nucleation of a mineral phase, the subsequent addition of ions can be thought of as its growth.

The calcite lattice is comprised of a repeating pattern of Ca^{2+} and CO_3^{2-}. In this lattice the charge from these ions are distributed about the lattice such that when each ion is fully coordinated a neutral charge is achieved. Due to the lack of coordination towards the surface of the lattice a charge is present. Ions in solution will become attracted to this charged surface, adsorb to it, become dehydrated and finally incorporate into the lattice. The two potential ion adsorption reactions are displayed in Eq. 2.19 and 2.19 (Sand et al., 2016). It is believed that the rate limiting process for both of these reactions is the removal of the hydration waters around the calcium atom (Larsen et al., 2010).

$$> CaCO_3^- + Ca^{2+} \rightleftharpoons > CO_3Ca^+ \tag{2.18}$$

$$> CO_3Ca^+ + CO_3^{2-} \rightleftharpoons > CaCO_3^- \tag{2.19}$$

At pH > 7.5 carbonate is more stable than bicarbonate on the calcite surface, and due to the rapid deprotonation of bicarbonate-carbonate a $HCO_3 + Ca^{2+}$ pathway can be ignored (Andersson et al., 2016).

The rate at which ions are attached to the mineral surface can be determined by Eq. 2.20. Where Φ is the Brownian flux, E_A is the activation energy barrier, k_b is the Boltzman constant, T is temperature in Kelvin, a_i is the aqueous activity of ion i, v_i is the detachment coefficient and P_i and P_j are he probability of the site being an i or a j site respectively (Nielsen et al., 2013).

$$u_i = \Phi e^{-E_A/k_bT} a_i P_j - v_i P_i \tag{2.20}$$

The net rate of ion attachment u_{net} can then be used to calculate the growth rate (R) by Eq. 2.21 where ρ is the kink density, h is step heigh, b is kink depth, d is mineral density and y_0 is terrace width (Nielsen et al., 2013).

$$R = \frac{\rho u_{net} hbd}{2y_o} \tag{2.21}$$

To minimise the energy required for the incorporation of these ions they will seek to minimise the amount of faces exposed to the solution. Figure 2.8 shows the potential

binding sites at a mineral's surface. By precipitation at kink and step vacancies vs adatom sites the incoming ions requires less energy to bind to the surface.

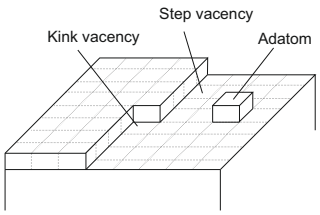

Figure 2.8: Three key surface binding sites

However, were the surface growth in figure 2.8 to continue until the upper layer of atoms is complete and there are no step or kink vacancies to fill, incoming ions would have to form adatoms to continue precipitation. This may be achieved through localised fluctuations in the energy environment (in the same way the initial critical nucleus is formed) however this would require a relatively high supersaturation of the mineral in solution (Woodruff, 2015).

A potential mechanism by which crystal growth can continue was proposed by the BCF theory presented by Burton et al. (1951). This paper reports the importance of dislocations within a crystal lattice on the growth of a mineral surface. Figure 2.9 displays a screw dislocation formed through a shear defect in the crystal lattice. As ions become incorporated at the step sites of this dislocation the step face simply rotates about an axis, constantly presenting a step face to co-ordinate onto. Spiral growth has been observed by a number of researchers through atomic force microscopy (Maiwa et al., 1998; Larsen et al., 2010; Wang et al., 2016).

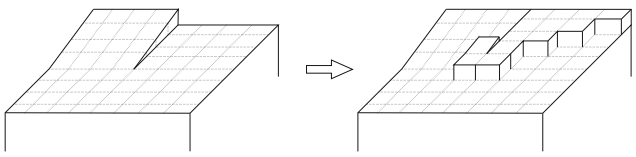

Figure 2.9: Spiral growth

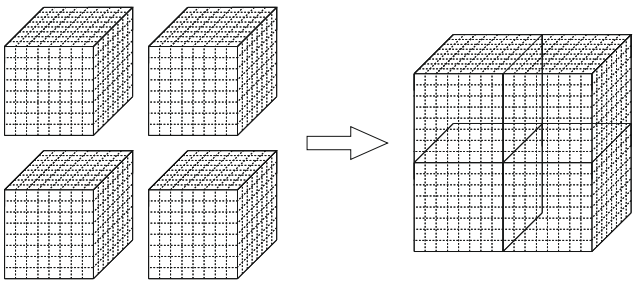

Figure 2.10: Orientated attachment of isomorphous particles

2.6 Crystal Morphologies

As the previous section introduced, ions in solution will precipitate to form a crystal lattice once their concentration passes a certain threshold. Certain arrangements of ions will be more stable than others resulting in energy wells that causes these precipitates to be meta-stable. For a given crystal composition there will exist a lattice arrangement that is the most thermodynamically stable however, often a transient chemical environment will favour the crystallisation of another polymorph which will convert to the more stable morphology, often through a series of intermediaries. This process is known as Ostwald's rule of stages, however there exists no definitive formula for predicting which morphologies will form in a given solution.

Calcium carbonate is a versatile mineral with three key polymorphs, each of which may display varying crystal morphologies depending on the solution from which they crystallised.

2.6.1 Calcite

Calcite is the most common carbonate polymorph, it belongs to $R\bar{3}C$ space group within the trigonal system (a subset of the Hexagonal system) and exhibits a diverse range

of morphologies. The most stable calcite morphology at atmospheric temperature and pressure is the calcite rhombohedron, where the interfacial angles are either 102° or 78°. (Ukrainczyk et al., 2014), the rhombohedral morphological unit cell of which is displayed in Fig. 2.11. An alternative unit cell is often quoted (the structural unit cell) where the a dimension is halved (from 10 Å to 5 Å) and the c dimension is doubled (from 8.5 Å to 17 Å), this makes the $\{10\bar{1}\}$ face $\{104\}$ (or $\{10\bar{1}4\}$) (Hazen, 2004). In calcite the central calcium atom is surrounded by 6 oxygen atoms with C-O bond lengths of 2.36 Å (Blanco-Gutierrez et al., 2014)

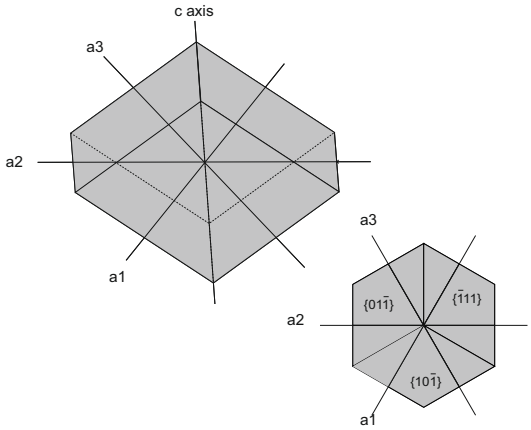

Figure 2.11: Calcite rhombohedral structural unit cell with miller indices, viewed from both an arbitary angle to observe all axes and from along the c axis displaying the hexagonal symmetry (amended from http://www.mindat.org/min-859.html)

Another common calcite morphology is that of the scalenohedron (Fig. 2.12). This morphology is commonly produced in industrial precipitated calcium carbonate production by the carbonation of $Ca(OH)_2$ (Thriveni et al., 2014). The dominant growth face in this morphology is the $\{21\bar{1}\}$ face.

The molar ratio of Ca^{2+} to CO_3^{2-} has a significant effect on the morphology of calcite precipitated (Jung et al., 2000). García Carmona et al. (2003) report the following ratios associated with the following morphologies.

Table 2.2: Calcite morphologies favoured at a range of $Ca:CO_3$ ratios

$Ca:CO_3$	Morphology
1.06-1.23	Rhombohedral
1.28-1.46	Rhombohedral-Scalenohedral
>1.56	Scalenohedral

This is due to the relative concentrations of Ca and CO_3 in the dominant faces of these morphologies. The $10\bar{1}$ face contains equal concentrations of calcium and carbonate atoms. Thus while the precipitating solution contains equimolar concentrations of Ca and CO_3 the rhombohedral morphology will be favoured. In solutions with excess Ca it has been suggested that growth sites may become blocked by the Ca ions and the formation of non-stoichiometric scalenohedral $\{21\bar{1}\}$ faces will be favoured.

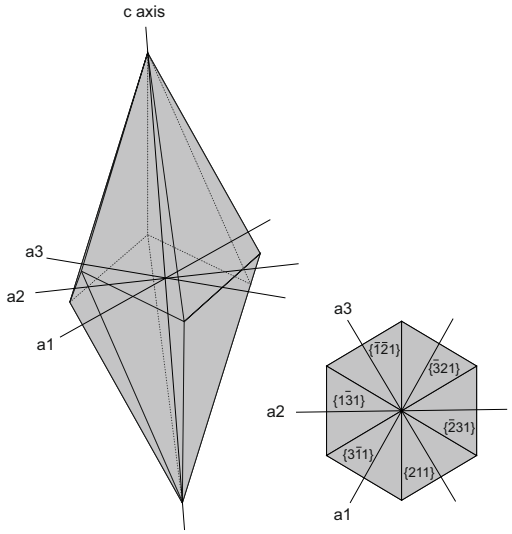

Figure 2.12: Calcite scalenohedral structural unit cell with miller indices, viewed from both an arbitary angle to observe all axes and from along the c axis displaying the hexagonal symmetry (amended from http://www.mindat.org/min-859.html)

2.6.2 Aragonite

Aragonite is a distinct polymorph of calcium carbonate, distinguished from calcite by its orthorhombic crystal system. This polymorph is commonly expressed as "needle"

like crystals although alternative morphologies of "cauliflower" and "flake" like crystals have been reported (Chakrabarty and Mahapatra, 1999). In aragonite the central calcium atom is coordinated by 9 oxygen ions with C-O bond lengths ranging from 2.41-3.55 Å (Blanco-Gutierrez et al., 2014).

Aragonite is a common biomineral present in calcifying organisms including the nacre of mollusk shells (Massaro et al., 2014), it is metastable with respect to calcite under atmospheric temperature and pressure. One of the factors which may promote the stability of aragonite is the presence of magnesium in solution. The Mg^{2+} ion adsorbs to the surface of calcite due to its high degree of hydration, forming $MgCO_3$ which is more soluble than pure calcite leading to the destabilisation of the calcite phase. Magnesium in not incorporated into the aragonite structure which means aragonite is unaffected by the presence of Mg in solution (Loste et al., 2003). Therefore in a Mg rich solution (Raz et al. (2000) suggest Mg:Ca of 4 or greater) precipitating calcium carbonate Aragonite will be favoured due to this destabilisation of the calcite phase, however, if the Mg is removed a phase change from aragonite to calcite will occur. Experimental results suggest that SO_4^{2-} favours the precipitation of aragonite over calcite (Bots et al., 2011). However, aragonite has also been observed to form in hyperalkaline springs, absent of these ions, at elevated temperatures (>25°C) (Chavagnac et al., 2013).

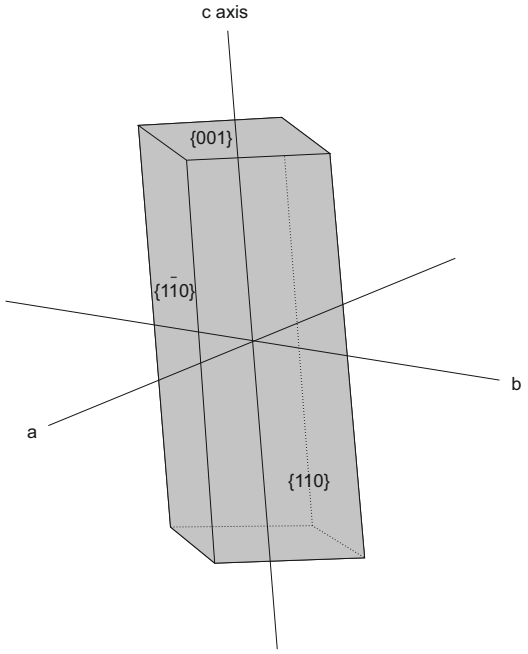

Figure 2.13: Aragonite structural unit cell with miller indices (amended from http://www.mindat.org/min-859.html)

2.6.3 Vaterite

Vaterite is the third polymorph of calcium carbonate and the least stable at room temperature and pressure. It belongs to the hexagonal crystal system and commonly presents as thin fibres or spherules. In vaterite the central calcium atom is coordinated by 8 oxygen atoms with C-O bond lengths ranging from 2.29-2.90 Å (Blanco-Gutierrez et al., 2014).

2.6.4 Amorphous Calcium Carbonate (ACC)

In addition to these three crystalline polymorphs calcium carbonate may form through an amorphous precursor.

ACC is a highly unstable form of calcium carbonate which commonly forms as a

precursor to the three main polymorphs (calcite, aragonite and vaterite). It has received a lot of interest in recent years due to its role in biomieral formation, allowing the formation of structurally complex minerals (Weiner et al., 2005) as well as its potential to enhance the doping of trace elements into calcite (Matsunuma et al., 2014), and the non-classical nucleation pathways it commonly exhibits (Gebauer et al., 2008).

The ACC structure has been found to comprise of a Ca-rich frame with interconnected tunnels containing water and CO_3^{2-} ions, with an overall chemical formula approximately $CaCO_3 \cdot H_2O$.

2.7 Solid solutions

The crystals we have discussed this far have been pure crystals, that is to say they contain no foreign ions. In reality most minerals have a variable composition and will allow for the substitution of trace elements. This principle has long been used by chemists to separate target species from a solution. In 1925, Doerner and Hoskins recognised that in a solution precipitating barium sulphate, the concentration of radium will be lowered even though the solubility limit of its sulphate had not been reached. This suggested that the precipitation of a major phase (in this case barium sulphate) can facilitate the coprecipitation of a minor phase (radium sulphate) even under conditions where the minor phase is soluble.

Different trace elements and different minerals will have varying affinities for one another. The carbonate system is particularly prone to such coprecipitation owing to the abundance of M^{2+} ions with a similar ionic radius to calcium. In order to better

understand the solid solution formed we need to understand the thermodynamics behind solid solution formation.

In section 2.3.1 we discussed the internal energy of a system and how this relates to the chemical potential of its constituent species. A simple mixture of two powders will have a free energy that is the sum of the chemical potentials of the individual powders multiplied by their mole fraction (Eq. 2.22).

$$G^{mm} = \Sigma \chi_i G_i \tag{2.22}$$

As Sr substitutes for Ca in calcite or aragonite it will form a binary solid solution between the pure calcium carbonate and pure strontianite end members with the composition $Ca_{1-x}Sr_xCO_3$. A binary solid solution differs from a simple mechanical mixture in that the two components are dispersed at an atomic scale which leads to bond forming and changes in entropy (S). The energy of a mechanical mixture (G_m^{mix}) is calculated by summing the products of the mole fractions and chemical potentials for all components (Eq. 2.22). The difference in energy of an ideal solid solution to this mechanical mixture is the change in entropy, which must be quantified. This is achieved by correcting for the amount of potential configurational arrangements (i.e. A-A, A-B, B-B)(Eq. 2.23a). This entropy change is then combined with the absolute temperature to determine the deviation from mechanical mixing 2.23b. The molar Gibbs energy of an ideal solid solution (G_m^{id}) can then be calculated by Eq. 2.23c. Where the first term defines the summation of the standard state chemical energies of the components and the second is derived from the entropy (Appelo. and Postma., 2007). The difference between the

energies of a mechanical mixture and solid solution are illustrated in Fig. 2.14.

$$\Delta S = -R\Sigma\chi_i \ln \chi_i \tag{2.23a}$$

$$= -k_B(N - A\ln(\frac{N_A}{N_A+N_B}) + N_B \ln(\frac{N_B}{N_A+N_B})$$

$$G^{id} = -T\Delta S \tag{2.23b}$$

$$G^{id} = \Sigma\chi_i G_i + RT\Sigma\chi_i \ln \chi_i \tag{2.23c}$$

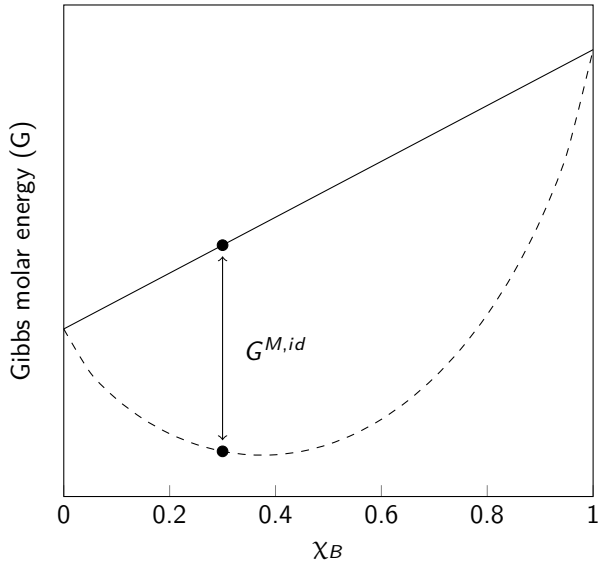

Figure 2.14: Comparison between a mechanical mixing trend (solid line) and an ideal solid solution (dashed line). With two hypothetical solutions (red dots) plotted.

2.7.1 Mechanisms for coprecipitation

There are three key coprecipitation mechanisms which can result in this solid solution, incorporation into crystal defects, major element substitution and adsorption (Meece and Benninger, 1993; Curti, 1997).

Incorporation into crystal defects

As a crystal lattice grows defects such as vacancies and dislocations form. These defects provide free space in the lattice in which ions can become trapped. As the precipitation rate increases the frequency of these defects increase and this becomes a more important process.

Sorption

An ionic crystal lattice, such as calcium carbonate, will have an overall neutral charge due to the balance between cations and anions. The surface of such a crystal however may host a surface charge significant enough to affect the growth of the crystal. This surface charge is generated due to a layer of uncoordinated Ca^{2+} and CO_3^{2-} ions at the surface of the lattice (Fenter and Sturchio, 2012).

Negative hydroxyl ions (OH^-) and positive hydrogen ions (H^+) are attracted to the uncoordinated Ca^{2+} and CO_3^{2-} ions respectively. Therefore in an alkaline solution OH^- ions will bind to the Ca^{2+} sites leaving the CO_3^{2-} site unoccupied generating a negative surface charge. This is exacerbated by deprotonation of the OH^- ions which amplify the negative surface charge. The Zeta point charge of calcite (i.e. the point at which the surface is un-charged) is reported to exist between pH 8-9.5 (Somasundaran and Agar, 1967).

Solution ions have also been reported to have an effect on the calcite surface charge. The presence of Mg^{2+} and Ca^{2+} produce a positive charge across a calcite surface, whereas SO_4^{2-} produced an overall negative charge (Kasha et al., 2015).

Sorption may be either outer sphere or inner sphere. Outer sphere complexes form when ions are attracted to the charged surface of a mineral however water sits between the solution ions and the mineral surface, which prevents bond forming. During inner sphere adsorption the water molecules are expelled and a bond forms between the ions and the mineral surface (Appelo. and Postma., 2007).

Sorption at the calcite surface may be of significant importance for the growth of precipitates due to its role in controlling solution chemistry and thus supersaturation at the solution/crystal interface. It will create a concentrated layer of cations close to the mineral surface, including Ca^{2+}, while anions, such as CO_3^{2-}, will be repelled.

Major element substitution

One of the key mechanisms by which a trace element can become incorporated into calcium carbonate is through the direct substitution for a major element within the carbonate lattice. This establishes a solid solution between the calcium carbonate ($CaCO_3$) and the trace metal carbonate (MCO_3). Major element substitution becomes more favourable the more similar the trace element is to the major element in terms of its ionic radius and charge (Curti, 1997). There are however, several other parameters which may have an impact.

2.7.2 Distribution coefficient

An useful measure of how effectively a trace metal will incorporate in a mineral is its distribution coefficient. A range of distribution coefficients (also known as partition coefficients) exist to quantity the affinity of the trace metal for the carrier mineral.

The most simple of these is the Berthelot-Nernst distribution coefficient (D_X) (Eq. 2.24). The values used for the trace (X) and Carrier (C) are important to the meaning of the D_X value. If the concentration of the trace and carrier of the bulk crystal are used then the D_X is a homogeneous distribution coefficient. Such a value is inapplicable to a system where the solution composition changes during precipitation. If the solution composition changes during precipitation then only the surface layer will be in equilibrium with the solution, and therefore only the composition of X and C in this layer may be used to calculate the distribution coefficient (this is termed a hetrogenous distribution coefficient).

$$\begin{aligned} D_X &= \frac{[X]/[C]_{ppt}}{[X]/[C]_{sol}} \\ \frac{[X]_{ppt}}{[C]_{ppt}} &= D_X \times \frac{[X]_{sol}}{[C]_{sol}} \end{aligned} \tag{2.24}$$

An alternative distribution coefficient was devised by Doerner and Hoskins (1925) to enable calculations to be made based on incremental changes in solution data (Fig. 2.25).

$$\begin{aligned} \lambda_X &= \frac{\ln([X]_{final}/[X]_{initial})}{\ln([Ca]_{final}/[Ca]_{initial})} \\ \ln\frac{[X]_{final}}{[X]_{initial}} &= \lambda_X \times \ln\frac{[Ca]_{final}}{[Ca]_{initial}} \end{aligned} \tag{2.25}$$

A trace element that substitutes very favourably in a carrier mineral and becomes enriched therein will have a distribution coefficient >1. Whereas a trace element which is unfavourable in the host mineral and accumulates in the parent solution will have a distribution coefficient <1.

Table 2.3: Berthelot-Nernst distribution coefficients for Sr into calcite and aragonite taken from (Curti, 1997)

Polymorph	D_{Sr}
Calcite	0.037-0.14
Aragonite	0.9-1.6

Fajans-Paneth-Hahn rule

The Fajans-Paneth-Hahn rule states that the distribution coefficient is dependent on the solubility of the trace element species in solution; with higher solubilities producing lower degrees of coprecipitation (Hahn, 1936). Based on this rule, any process which can lower the solubility of $SrCO_3$ will facilitate higher D_{Sr} values, and greater Sr concentrations in the precipitate. The solubility of $SrCO_3$ has been reported to decrease with increasing temperature and is proportional to the cube root of CO_2 fugacity (Helz and Holland, 1965). pH is also expected to have an effect on the solubility of strontianite in a similar way to calcite, with increasing pH leading to decreasing solubility.

Rate effect

The rate of calcium carbonate precipitation is another key control on the distribution coefficient of strontium. A study by (Lorens 1981) used a pH-stat to maintain a constant degree of carbonate supersaturation - and thus a constant precipitation rate on D_{Sr}. By repeating individual experiments at differing supersaturations they were able to determine the effect of varying precipitation rate (Fig. 2.15). Their results indicate that precipitation rate has a strong effect on the D_{Sr}, with more Sr incorporated under faster precipitation rates. The suggested mechanism for this is that under low precipitation rates, the cation sites at the surface of a mineral are almost in equilibrium with the

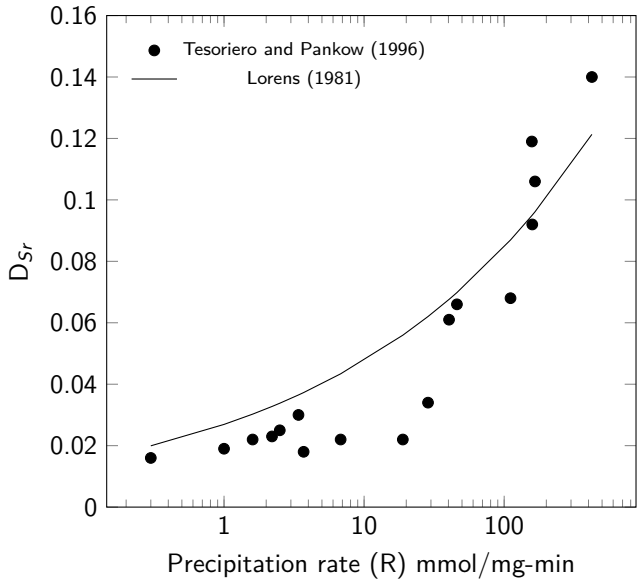

Figure 2.15: Experimental data from (Tesoriero and Pankow, 1996) plotted against a model produced by Lorens (1981) ($log(D_{Sr}) = 0.249 \times log(R) - 1.57$) R=nmol of $CaCO_3$per mg of seed crystal per minute

bulk solution. Under these conditions the incorporation of a trace element such as Sr will be relatively unfavourable owing to the relative difference between its ionic radius and the ideal for the site. Because of this it may become displaced from the surface of the mineral before it is fully coordinated by carbonates and incorporated into the lattice. Under fast precipitation rates it is more likely that the Sr^{2+} ion will become fully coordinated by CO_3^{2-}- and thus incorporated into the mineral lattice - before it can become displaced by an ion more favourable that site.

pH has been shown to increase the rate of calcite precipitation, leading to rapid precipitation of small crystals (Ma et al., 2010). Therefore high pH solutions may be preferable for Sr coprecipitation.

Temperature

Kinsman and Holland (1969) report a linear correlation between temperature and

D_{Sr} (Figure 2.16). The cause of this trend is likely to be the changing solubilities of the carbonate phases in solution. As temperature increases the solubility of both strontianite and calcite decrease. However, the solubility of strontianite is most affected by temperature changing the solubility ratios of strontianite to calcite. As strontianite s solubility increases relative to calcites the distribution coefficient increases (Kinsman and Holland, 1969).

Another possible effect of temperature is alluded to in (Plummer et al., 1978), where it is shown that the rate of calcite precipitation is dependent on temperature. Because of the importance of the rate effect reported by (Lorens, 1981) it is possible this mechanism could play a role in controlling the distribution coefficient. However, data displayed in figure 2.16 indicates that the change in precipitation rate between 15 - 30°C is minimal.

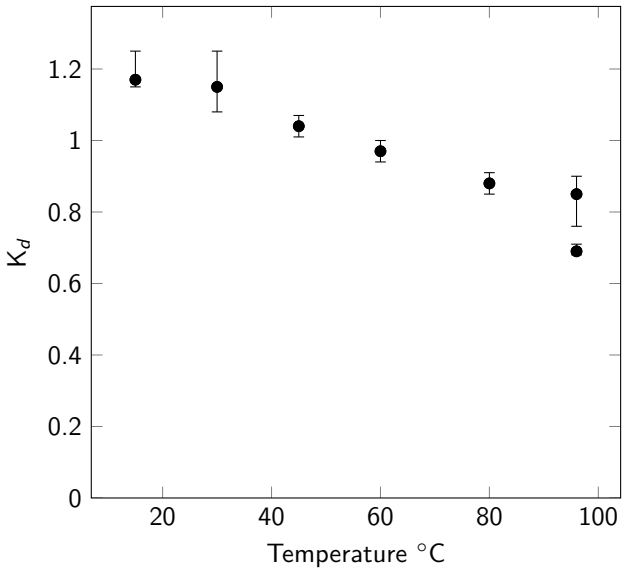

Figure 2.16: Data from (Kinsman and Holland, 1969) displaying the effect of temperature on the K_d. Data points represent averages of several experiments carried out at each temperature. In this paper a different formulation of the distribution coefficient formula is used $log\left(1+\left(\frac{[Sr]_i}{[Sr]_f}\right)\right) = K_d\left(1+log\left(\frac{[Ca]_i}{[Ca]_f}\right)\right)$

Ionic radius effect

The size of the trace elements ionic radius relative to the ideal for the lattice site strongly controls how effectively a substitution can take place. Strontium's ionic radius is 1.13 Å - 14% greater than that of calcium. This reduces how effectively it can substitute for calcium in calcite which is reflected in its partition coefficient. Literature values suggest a partition coefficient for strontium into calcite of 0.02-0.39 (Curti, 1997). Comparing this with the quoted partition coefficient for cadmium into calcite of 3040-9.5 (Curti, 1997) (which has an ionic radius of 0.95Å, 4% smaller than Ca^{2+}) it becomes clear that ions with significantly larger ionic radii than calcium are less readily incorporated into calcite.

Another result of the ionic radius effect can be seen in the partition coefficients into the different phases of calcium carbonate. The M^{2+} lattice site in calcite is characterised by a 6 fold symmetry whereas aragonite displays a 9 fold symmetry, creating a larger lattice site (Lorens, 1981). This larger lattice site is better able to accommodate the Strontium ion, and literature values suggest a D_{Sr} into aragonite of 0.9-1.6 (Kinsman and Holland, 1969).

Competitive ion effect

A study by Pingitore Jr and Eastman (1986) showed that the addition of barium to a solution could suppress the strontium partition coefficient, this effect was most prevalent in dilute Sr solutions. Because barium is an divalent cation with a larger ionic radius than Sr it will mostly compete for surface defect sites rather than lattice sites. Because these defect sites are limited and offer a lower energy environment for large cations

such as Sr and Ba they are important site for trace element incorporation under low concentration conditions (at higher concentrations the greater number of lattice sites overwhelm the surface defect sites). A similar effect is observed with increasing NaCl concentration in the solution.

Solution chemistry can also have a significant effect on the partition coefficient; through its effects on aqueous complexation, site competition and the polymorph of carbonate formed. Solutions bearing Mg^{2+}, Ni^{2+}, Co^{2+}, Fe^{2+}, Zn^{2+}, and Cu^{2+} favour the precipitation of aragonite. Whereas the presence of Mn^{2+}, Cd^{2+}, Ca^{2+}, Sr^{2+}, Pb^{2+}, and Ba^{2+} favour the formation of calcite. Of these species Mg^{2+} has the greatest control on the final polymorph (Söhnel and Mullin, 1982) thus the greater Mg^{2+} concentrations are likely to lead to greater partition coefficients.

The SO_4^{2-} ion has been shown to favour the stabilisation of aragonite precipitates (Bots et al., 2011). This may have a positive effect on the substitution of Sr^{2+} into carbonates by increasing the lattice volume.

Summary

Based on this information Sr^{2+} coprecipitation should be favoured at relatively high precipitation rates; where its incorporation is into the abundant lattice sites available in a structurally open calcium carbonate polymorph, such as aragonite or ACC. Competitive ions should be minimised however the extent to which this is necessary is uncertain at the concentrations of Sr to be used in these experiments. Magnesium doping however may induce aragonite formation which would be favourable. The temperature should have little effect between 15 - 35 degrees however, temperatures lower than this were

not tested and may be encountered during groundwater treatment.

2.8 Remediation by carbonate coprecipitation

To date much research into carbonate coprecipitation has been focused on natural systems including biogenic calcite (Lorens, 1981), limestone lithification (Pingitore Jr et al., 1992) and lacustrine systems (Tesoriero and Pankow, 1996); with few researchers seeking to apply this process to groundwater remediation. However, carbonate precipitation controlled by bacterial ureaolysis has been suggested as a mechanism for the in-situ remediation of ^{90}Sr and other divalent cations from groundwater (Fujita et al., 2000; Mitchell and Ferris, 2005). Mitchell and Ferris (2005) were able to achieve 35% removal of solution Sr through carbonate precipitation, however, their starting concentration of 8769 ppm is significantly greater than the ca.0.1 ppm observed at Sellafield and it is unclear how the system would behave under these low concentration conditions. Also, while the use of in-situ reactions would reduce pumping and disposal costs, the ability to closely control the solution composition is lost. Finally pump and treat would minimise the potential for dissolution and re-mobilisation by removing the activity from the ground - which is particularly important if ^{14}C is to be included in the treatment, owing to its 5730 year half life.

2.9 Isotopic exchange and fractionation

$^{14}CO_3$ will take place in the carbonate forming reaction as well as $^{12}CO_3$; by this mechanism $^{14}CO_3$ will become depleted in the solution. However, due to differences in

atomic mass $^{14}CO_3$ will not react exactly as $^{12}CO_3$. This is known as an isotope effect and results in slightly differing chemical behaviour of the different isotopes. These isotope effects will manifest differently under different conditions.

When the reaction is far from equilibrium (where the reverse component of the reaction is small) the light isotope will become concentrated in the reaction products. This is because the heavier isotope moves more slowly and thus has a slower reaction rate (Hoefs, 2013).

Under equilibrium conditions (where the reverse component of the reaction is equal to the forward) the heavier isotope will become concentrated in the products. This is because the heavy isotope will have a lower zero point energy which is due to a lower molecular vibration. Because of this lower molecular vibration, bonds formed by the heavier ^{14}C will be stronger leading to more stable compounds (Hoefs, 2013). Based on this $^{14}CO_3$ is likely to be more stable in the final carbonate than $^{12}CO_3$, which bodes well for the long term stability of the final product.

The extent to which the isotopes have separated between the two phases is determined by the fractionation factor α. Where R_A is the ratio of isotopes in phase A and R_B is the ratio of isotopes in phase B.

$$\alpha_{A-B} = \frac{R_A}{R_B} \tag{2.26}$$

Bibliography

Andersson, M., Rodriguez-Blanco, J., Stipp, S. (2016). Is bicarbonate stable in and on the calcite surface? *Geochimica et Cosmochimica Acta*, **176**, pp. 198–205.

Appelo., C.A.J., Postma., D. (2007). *Geochemistry, groundwater and pollution*. A.A. Balkema.

Baldwin, N.D. (2003). Remediating Sellafield: A New Focus for the Site. *9th ASME International Conference on Radioactive Waste Management and Environmental Remediation: Volumes 1, 2, and 3*, pp. 35–40.

Barton, C.S., Stewart, D.I., Morris, K., Bryant, D.E. (2004). Performance of three resin-based materials for treating uranium-contaminated groundwater within a PRB. *Journal of hazardous materials*, **116**(3), pp. 191–204.

Becker, R., Döring, W. (1935). Kinetische behandlung der keimbildung in übersättigten dämpfen. *Annalen der Physik*.

Benner, S.G., Blowes, D.W., Gould, W.D., Herbert, R.B., Ptacek, C.J. (1999). Geochemistry of a permeable reactive barrier for metals and acid mine drainage. *Environmental Science and Technology*, **33**(16), pp. 2793–2799.

Benning, L.G., Waychunas, G.A. (2008). Nucleation, growth, and aggregation of mineral phases: Mechanisms and kinetic controls. In *Kinetics of Water-Rock Interaction*, 259. pp. 259–333.

Blanco-Gutierrez, V., Demourgues, A., Jubera, V., Gaudon, M. (2014). Eu(III)/Eu(II)-

doped (Ca 0.7 Sr 0.3) CO3 phosphors with vaterite/calcite/aragonite forms as shock/temperature detectors. *J. Mater. Chem. C*, **2**(46), pp. 9969–9977.

Bots, P., Benning, L.G., Rickaby, R.E.M., Shaw, S. (2011). The role of SO4 in the switch from calcite to aragonite seas. *Geology*, **39**(4), pp. 331–334.

Boylan, A.A., Stewart, D.I., Graham, J.T., Trivedi, D., Burke, I.T. (2016). Mechanisms of inorganic carbon-14 attenuation in contaminated groundwater: Effect of solution pH on isotopic exchange and carbonate precipitation reactions. *Applied Geochemistry*, pp. 1–11.
URL: *http://dx.doi.org/10.1016/j.apgeochem.2016.12.006*

Burton, W.K., Cabrera, N., Frank, F.C. (1951). The Growth of Crystals and the Equilibrium Structure of their Surfaces. *Philosophical Transactions of the Royal Society A: Mathematical, Physical and Engineering Sciences*, **243**(866), pp. 299–358.

Bush, R.P., Smith, G.M., White, I.F. (1984). Carbon-14 waste management. Technical report, Commission of the European Communities, Luxembourg.

Chakrabarty, D., Mahapatra, S. (1999). Aragonite crystals with unconventional morphologies. *J. Mater. Chem.*

Chavagnac, V., Ceuleneer, G., Monnin, C., Lansac, B., Hoareau, G., Boulart, C. (2013). Mineralogical assemblages forming at hyperalkaline warm springs hosted on ultramafic rocks: A case study of Oman and Ligurian ophiolites. *Geochemistry, Geophysics, Geosystems*, **14**(7), pp. 2474–2495.

Cook, G.T., MacKenzie, A.B., McDonald, P., Jones, S.R. (1997). Remobilization of Sellafield-derived radionuclides and transport from the north-east Irish Sea. *Journal of Environmental Radioactivity*, **35**(3), pp. 227–241.

Cruickshank, J. (2012). Findings of the Sellafield Contaminated Land & Groundwater Management Project and the Next Steps for the Land Quality Programme. Technical report.

Cummins, N., Garrard, G., Day, J. (2016). Phase 2 Report Permeable Reactive Barrier Contents. Technical report, CH2M Hill.

Curti, E. (1997). *Coprecipitation of radionuclides: basic concepts, literature review and first applications*. Paul Scherrer Institut.

Debenedetti, P.G. (1996). *Metastable liquids: concepts and principles*. Princeton University Press.

Defra (2002). UK strategy for radioactive discharges 2001–2020. Technical Report July, Defra.

Doerner, H.A., Hoskins, W.M. (1925). Co-Precipitation of Radium and Barium Sulfates. *Journal of the American Chemical Society*, **47**(3), pp. 662–675.

Dorvee, J.R., Veis, A. (2013). Water in the formation of biogenic minerals: Peeling away the hydration layers. *Journal of Structural Biology*, **183**(2), pp. 278–303. **URL:** *http://dx.doi.org/10.1016/j.jsb.2013.06.007*

El-Ghonemy, H. (2004). SCLS Phase 1 – Sellafield Groundwater. Technical Report March, BNFL.

Fairchild, I.J., Smith, C.L., Baker, A., Fuller, L., Spötl, C., Mattey, D., McDermott, F., E.I.M.F. (2006). Modification and preservation of environmental signals in speleothems. *Earth-Science Reviews*, **75**(1), pp. 105–153.

Fairhall, G.A., Palmer, J.D. (1992). The encapsulation of Magnox Swarf in cement in the United Kingdom. *Cement and Concrete Research*, **22**(2-3), pp. 293–298.

Fenter, P., Sturchio, N.C. (2012). Calcite (104)-water interface structure, revisited. *Geochimica et Cosmochimica Acta*, **97**, pp. 58–69. **URL:** *http://dx.doi.org/10.1016/j.gca.2012.08.021*

Fujita, Y., Ferris, F.G., Lawson, R.D., Colwell, F.S., Smith, R.W. (2000). Calcium carbonate precipitation by ureolytic subsurface bacteria. *Geomicrobiology Journal*, **17**(4), pp. 305–318.

García Carmona, J., Gómez Morales, J., Rodríguez Clemente, R. (2003). Rhombohedral-scalenohedral calcite transition produced by adjusting the solution electrical conduc-

tivity in the system Ca(OH)2-CO2-H2O. *Journal of colloid and interface science*, **261**(2), pp. 434–40.

Garrard, G., Simpkin, T., J, D., R, L. (2016). In-ground options to mitigate leaks from the MSSS: Overview report. Technical report, CH2M Hill.

Gebauer, D., Cölfen, H. (2011). Prenucleation clusters and non-classical nucleation.

Gebauer, D., Volkel, A., Colfen, H. (2008). Stable Prenucleation Calcium Carbonate Clusters. *Science*, **322**(5909), pp. 1819–1822.
URL: *http://www.sciencemag.org/cgi/doi/10.1126/science.1164271*

Gibbs, J. (1878). *The Collected Works. Vol.1. Thermodynamics*. Yale University Press.

Glynn, P.D., Reardon, E.J. (1990). Solid-solution aqueous-solution equilibria: thermodynamic theory and representation.
URL: *http://earth.geology.yale.edu/ ajs/1990/02.1990.02Glynn.pdf*

Guggenheim, E. (1937). The theoretical basis of Raoult's law. *Transactions of the Faraday Society*.
URL: *http://pubs.rsc.org/en/content/articlepdf/1937/tf/tf9373300151*

Hahn, O. (1936). *Applied Radiochemistry*. Cornell University Press.

Hazen, R. (2004). Chiral crystal faces of common rock-forming minerals. *Progress in Biological Chirality*, pp. 137–151.

Hedges, L.O., Whitelam, S. (2011). Limit of validity of Ostwalds rule of stages in a statistical mechanical model of crystallization. *Journal of Chemical Physics*, **135**(16).

Helz, G.R., Holland, H.D. (1965). The solubility and geologic occurrence of strontianite. *Geochimica et Cosmochimica Acta*, **29**(12), pp. 1303–1315.

Hoefs, J. (2013). *Stable Isotope Geochemistry*. Springer Science & Business Media.

Jung, W.M., Kang, S.H., Kim, W.S., Choi, C.K. (2000). Particle morphology of calcium carbonate precipitated by gas–liquid reaction in a Couette–Taylor reactor. *Chemical Engineering Science*, **55**(4), pp. 733–747.

Kapel, M. (2011). *The essentials of chemical thermodynamics*. Book Guild.

Kasha, A., Al-Hashim, H., Abdallah, W., Taherian, R., Sauerer, B. (2015). Effect of Ca2+, Mg2+ and SO42− ions on the zeta potential of calcite and dolomite particles aged with stearic acid. *Colloids and Surfaces A: Physicochemical and Engineering Aspects*, **482**, pp. 290–299.

Kinsman, D.J.J., Holland, H.D. (1969). The co-precipitation of cations with CaCO3—IV. The co-precipitation of Sr2+ with aragonite between 16° and 96°C. *Geochimica et Cosmochimica Acta*, **33**(1), pp. 1–17.

Kulp, J.L., Schulert, A.R. (1962). Strontium-90 in man V. *Science*, **136**(3516), pp. 619–632.
URL: *http://www.jstor.org/stable/1708653*

LaMer, V., Dinegar, R. (1950). Theory, production and mechanism of formation of monodispersed hydrosols. *Journal of the American Chemical . . .* , **72**(8), pp. 4847–4854.
URL: *http://pubs.acs.org/doi/abs/10.1021/ja01167a001*

Lancefield, R., Garrard, G., Day, J. (2016). Phase 2 Report In-Situ Redox Manipulation and Other Injectable Technologies Contents. Technical Report May, CH2M Hill.

Larsen, K., Bechgaard, K., Stipp, S. (2010). The effect of the Ca2+ to activity ratio on spiral growth at the calcite surface. *Geochimica et Cosmochimica Acta*, **74**(7), pp. 2099–2109.

Lorens, R.B. (1981). Sr, Cd, Mn and Co distribution coefficients in calcite as a function of calcite precipitation rate. *Geochimica et Cosmochimica Acta*, **45**(4), pp. 553–561.

Loste, E., Wilson, R.M., Seshadri, R., Meldrum, F.C. (2003). The role of magnesium in stabilising amorphous calcium carbonate and controlling calcite morphologies. *Journal of Crystal Growth*, **254**(1–2), pp. 206–218.

Ma, Y., Gao, Y., Feng, Q. (2010). Effects of pH and temperature on CaCO3 crystallization in aqueous solution with water soluble matrix of pearls. *Journal of Crystal Growth*, **312**(21), pp. 3165–3170.

Maiwa, K., Plomp, M., van Enckevort, W., Bennema, P. (1998). AFM observation of barium nitrate {111} and {100} faces:. *Journal of Crystal Growth*, **186**(1-2), pp. 214–223.

Massaro, F.R., Bruno, M., Rubbo, M. (2014). Surface structure, morphology and (110) twin of aragonite. *CrystEngComm*, **16**(4), p. 627.

Matsunuma, S., Kagi, H., Komatsu, K., Maruyama, K., Yoshino, T. (2014). Doping incompatible elements into calcite through amorphous calcium carbonate. *Crystal Growth & Design*, **14**(11), pp. 5344–5348.

Meece, D.E., Benninger, L.K. (1993). The coprecipitation of Pu and other radionuclides with CaCO3. *Geochimica Et Cosmochimica Acta*, **57**(7), pp. 1447–1458.

Mitchell, A.C., Ferris, F.G. (2005). The coprecipitation of Sr into calcite precipitates induced by bacterial ureolysis in artificial groundwater: Temperature and kinetic dependence. *Geochimica et Cosmochimica Acta*, **69**(17), pp. 4199–4210.

Mullin, J.W. (1972). *Crystallisation*. Book, Whole. London: Butterworths.

Nielsen, L.C., De Yoreo, J.J., DePaolo, D.J. (2013). General model for calcite growth kinetics in the presence of impurity ions. *Geochimica et Cosmochimica Acta*, **115**, pp. 100–114.
URL: *http://dx.doi.org/10.1016/j.gca.2013.04.001*

Nielsen, M.H., Aloni, S., De Yoreo, J.J. (2014). In situ TEM imaging of CaCO3 nucleation reveals coexistence of direct and indirect pathways. *Science*, **345**(6201), pp. 1158–1162.

Nilsson, Ö., Sternbeck, J. (1999). A mechanistic model for calcite crystal growth using surface speciation. *Geochimica et Cosmochimica Acta*, **63**(2), pp. 217–225.

Ostwald, W. (1897). Studien über die Bildung und Umwandlung fester Körper. 1. Abhandlung: Übersättigung und Überkaltung. *Zeitschrift für Physikalische Chemie*, **22**, pp. 289–330.

Palmisano, A., Hazen, T. (2003). Bioremediation of metals and radionuclides: What it is and how it works. Technical report, Lawrence Berkeley National Laboratory.

Pingitore Jr, N.E., Eastman, M.P. (1986). The coprecipitation of Sr2+ with calcite at 25°C and 1 atm. *Geochimica et Cosmochimica Acta*, **50**(10), pp. 2195–2203.

Pingitore Jr, N.E., Lytle, F.W., Davies, B.M., Eastman, M.P., Eller, P.G., Larson, E.M. (1992). Mode of incorporation of Sr2+ in calcite: Determination by X-ray absorption spectroscopy. *Geochimica et Cosmochimica Acta*, **56**(4), pp. 1531–1538.

Plummer, L.N., Wigley, T.M.L., Parkhurst, D.L. (1978). The Kinetics of Calcite Dissolution in CO2-Water Systems at 5°C to 60°C and 0.0 to 1.0 ATM CO2. *Americal Journal of Science*, **278**, pp. 179–216.

Pouget, E.M., Bomans, P.H.H., Goos, J.A.C.M., Frederik, P.M., de With, G., Sommerdijk, N.A.J.M. (2009). The initial stages of template-controlled CaCO3 formation revealed by cryo-TEM. *Science*, **587**(March), pp. 2007–2010.

Raz, S., Weiner, S., Addadi, L. (2000). Formation of High-Magnesian Calcites via an Amorphous Precursor Phase: Possible Biological Implications. *Advanced Materials*, **12**(1), pp. 38–42.

Reeve, P., Eilbeck, K. (2007). Contaminated land and groundwater management at Sellafield, a large operational site with significant legacy and contaminated land challenges. Proceedings of the 11th International Conference on Environmental Remediation and Radioactive Waste Management ICEM2007, pp. 1–7.

Richens, D.T. (1993). *The chemistry of aqua ions of biological importance*, volume 2. Wiley.
URL: *http://agris.fao.org/agris-search/search.do?recordID=US201300029619*

Rodriguez-Blanco, J.D., Shaw, S., Benning, L.G. (2011). The kinetics and mechanisms of amorphous calcium carbonate (ACC) crystallization to calcite, viavaterite. *Nanoscale*, **3**(1), pp. 265–271.

Sand, K.K., Tobler, D., Dobberschütz, S., Larsen, K.K., Makovicky, E., Andersson, M.P., Wolthers, M., Stipp, S.L.S. (2016). Calcite growth kinetics: Dependence on

saturation index, Ca 2+ :CO 3 2- activity ratio and surface atomic structure. *Crystal Growth & Design*, **16**(7), p. acs.cgd.5b01792.

Sleutel, M., Lutsko, J., Van Driessche, A.E.S., Durán-Olivencia, M.A., Maes, D. (2014). Observing classical nucleation theory at work by monitoring phase transitions with molecular precision. *Nature communications*, **5**, p. 5598.

Smith, E.B. (1990). *Basic chemical thermodynamics: Fourth edition*. Imperial College Press.
URL: *http://pubs.acs.org/doi/abs/10.1021/ed068pA232.1*

Söhnel, O., Mullin, J.W. (1982). Precipitation of calcium carbonate. *Journal of Crystal Growth*, **60**(2), pp. 239–250.

Somasundaran, P., Agar, G. (1967). The zero point of charge of calcite. *Journal of Colloid and Interface Science*, **24**(4), pp. 433–440.

Song, R.Q., Cölfen, H. (2010). Mesocrystals–ordered nanoparticle superstructures. *Advanced materials (Deerfield Beach, Fla.)*, **22**(12), pp. 1301–30.

Stamoulis, K.C., Assimakopoulos, P.A., Ioannides, K.G., Johnson, E., Soucacos, P.N. (1999). Strontium-90 concentration measurements in human bones and teeth in Greece. *Science of the Total Environment*, **229**(3), pp. 165–182.

Stamper, A., Coughlin, D., Bowes, A., Ruddick, P., Laws, F. (2014). Groundwater Monitoring at Sellafield Annual Data Review 2013. Technical Report LQRD000077.

Stranski, I. (1928). Zur theorie des kristallwachstums. *Z. phys. Chem.*

Szecsody, J., Williams, M., Burns, C., Girvin, D., Moore, R., Mckinley, J., Fruchter, J., Truex, M., Vermeul, V., Phillips, J. (2007). Hanford 100-N Area Apatite Emplacement: Laboratory Results of Ca-Citrate-PO4 Solution Injection and Sr-90 Immobilization in 100-N Sediments. Technical report, US Department of Energy.

Tesoriero, A.J., Pankow, J.F. (1996). Solid solution partitioning of Sr2+, Ba2+, and Cd2+ to calcite. *Geochimica et Cosmochimica Acta*, **60**(6), pp. 1053–1063.

Thriveni, T., Um, N., Nam, S. (2014). Factors affecting the crystal growth of scalenohedral calcite by a carbonation process. *Journal of the Korean ...*.

Ukrainczyk, M., Gredičak, M., Jerić, I., Kralj, D. (2014). Interactions of Scalenohedral Calcite Crystals with Acidic Amino Acid Derivatives of Salicylic Acid. *Crystal Growth & Design*, **14**(9), pp. 4335–4346.

Vekilov, P.G. (2010). Nucleation. *Crystal Growth and Design*, **10**(12), pp. 5007–5019.

Volmer, M. (1939). Kinetik der Phasenbildung. *Zeitschrift für Elektrochemie und angewandte physikalische Chemie*, p. 220.

Wallace, S.H., Shaw, S., Morris, K., Small, J.S., Fuller, A.J., Burke, I.T. (2012). Effect of groundwater pH and ionic strength on strontium sorption in aquifer sediments: Implications for 90Sr mobility at contaminated nuclear sites. *Applied Geochemistry*, **27**(8), pp. 1482–1491.

Wang, H., Zeuschner, J., Eremets, M., Troyan, I., Willams, J. (2016). Stable solid and aqueous H2CO3 from CO2 and H2O at high pressure and high temperature. *Scientific Reports*, **6**(January), p. 19902.
URL: *http://www.nature.com/articles/srep19902*

Wei, W., Ma, G.H., Hu, G., Yu, D., Mcleish, T., Su, Z.G., Shen, Z.Y. (2008). Preparation of hierarchical hollow CaCo3 particles and the application as anticancer drug carrier. *Journal of the American Chemical Society*, **130**(47), pp. 15808–15810.

Weiner, S., Sagi, I., Addadi, L. (2005). Choosing the Crystallization Path Less Traveled. *Science*, **309**(5737), pp. 1027–1028.
URL: *http://www.sciencemag.org/content/309/5737/1027.short http://www.sciencemag.org/content/309/5737/1027.full.pdf*

Woodruff, D.P. (2015). How does your crystal grow? A commentary on Burton, Cabrera and Frank (1951) 'The growth of crystals and the equilibrium structure of their surfaces'. *Philosophical Transactions of the Royal Society A: Mathematical, Physical and Engineering Sciences*, **373**(2039), pp. 20140230–20140230.

World Nuclear Association (2016). Nuclear Power Today | Nuclear Energy - World Nuclear Association.
URL: *http://www.world-nuclear.org/information-library/country-profiles/countries-t-z/united-kingdom.aspx http://www.world-nuclear.org/information-library/current-and-future-generation/nuclear-power-in-the-world-today.aspx*

Yim, M.S., Caron, F. (2006). Life cycle and management of carbon-14 from nuclear power generation. *Progress in Nuclear Energy*, **48**(1), pp. 2–36.

Part II

Methodology

Chapter 3

Experimental set-up

3.1 Lab set-up

Experiments were designed to investigate the removal of contaminants from groundwater, however, to enable the effects of individual ions to be isolated a deionised water (DIW) stimulant was used. Boylan et al. (2016) showed that below pH 9.3 ^{14}C de-gasses as $^{14}CO_2$ as such wherever ^{14}C was desired to be in solution NaOH or $Ca(OH)_2$ was added to ensure the pH was greater than 9.3.

Experiments were carried out using Carbon-14 as this allowed us to separate the removal of ^{14}C from other TIC that was in gassing into the solution. ^{14}C was added as $^{14}HCO_3^-$ which is predicted to be the main ^{14}C bearing phase underlying Sellafield (Boylan et al., 2016). A concentration of 100 KBq L^{-1} was selected, this is approximately 2 times the maximum concentration of ^{14}C in Sellafield groundwater. Such a high concentration of ^{14}C was selected as this allowed for accurate detection of ^{14}C following removal by several orders of magnitude.

Strontium was added as non-active $SrCl_2 \cdot 6H_2O$. Non-active Sr was used as there was no secondary source of Sr in these experiments. Furthermore the Sr concentration in Sellafield groundwater is low (0.16-5.35 μM), and this treatment would not distinguish between active and non-active Sr. A concentration of 10 ppm (114 μM) was used, this is approximately 20$\times$ the maximum Sr concentration at Sellafield.

Calcium was added to the solutions as Calcium Hydroxide ($Ca(OH)_2$). This was selected as a reagent as it is a readily available material with a wide array of applications, including steel manufacture and construction (Moorehead, 1986). Because of this it can be purchased cheaply and in large quantities. Calcium hydroxide has the added benefit of containing OH^- ions, acting as an alkaline buffer and maintaining ^{14}C solubility.

Sodium Carboante (Na_2CO_3) was selected as the carbonate source for these experiments. Similarly to $Ca(OH)_2$ it is a cheap and widely used chemical, mainly used in glass manufacture (Garrett, 1992). In the Sellafield groundwater inorganic carbon is present at moderate concentrations (1.23 mM) Graham (2013). Therefore it is unlikely that the final treatment will require the addition of further carbonate.

pH was measured using an Orion 420 pH meter with a VWR SJ113 probe calibrated at pH 7.0, 10.01 and 12.46.

3.1.1 Free-Drift precipitation

In Chapter 4 data is presented from a series of free-drift calcite precipitation experiments. In these experiments a 100 mL alkaline solution (pH 12) was created using 99 mL DIW and a 1 mL of a 1M NaOH stock solution. This solution was then transferred to a

500 mL polypropylene conical flask (ThermoFisher Scientific, USA). 10 KBq of ^{14}C activity was added as a 100 μL aliquot of $^{14}HCO_3$ solution (the TIC concentration of this solution was negligible). 1 mL of 1000 ppm $SrCl_2{\cdot}6H_2O$ was added to achieve 10 ppm in solution. Calcium Hydroxide was added as a solid, with masses of 0.0074, 0.074 and 0.74g. Na_2CO_3 was added as an aliquot taken from a 1 M solution, with volumes of 0.1, 1 and 10 mL.

Free-drift experiments in Chapter 5 used a solution as the source of $Ca(OH)_2$ rather than solid powder. This solution was prepared by dialysis filtration in 1 L Schott flasks. The flasks were filled with Milli-Q water and bubbled with N_2 gas for 30 minutes to ensure they were free from CO_2. A mass of 20 g of $Ca(OH)_2$ powder was mixed into a slurry with a small volume of MQ water and subsequently inserted into a section of dialysis tubing which was then sealed at both ends. This tubing was inserted into the 1 L flask of MQ water, the N_2 tube removed and the cap screwed firmly on. $Ca(OH)_2$ flasks were allowed to equilibrate for 1 week to ensure equilibrium had been reached. For the experiments in Chapter 5 this saturated calcium hydroxide solution was diluted 1:1 with DIW which yielded a 8.92 ± 0.87 mM $Ca(OH)_2$ solution.

3.1.2 Constant composition precipitation

A 150 mL spherical reaction vessel was selected as a vessel for the constant composition reactor. Inlets were created with two 19 gauge needles, which were pierced through rubber valves. An overflow in the top of the vessel was included to allow the solution and precipitate to flush through the reactor, and a magnetic stirrer bar was included to ensure effective mixing. The Calcium Hydroxide reagent was prepared by dialysis filtration

as previously discussed however for these experiments the solution concentration was adjusted by conductivity and pH to ensure a more uniform concentration (8.73 ± 0.34 mM). A sodium carbonate solution with a concentration of 50 ± 0.024 mM was created by dissolving Na_2CO_3 powder in MQ water. These two solution were fed into the reactor at a constant rate of 135 mL h^{-1} (1.18mmol h^{-1}) and 15 mL h^{-1} (0.75 mmol h^{-1}) respectively.

3.1.3 Cement encapsulation

Strontium bearing calcite was prepared via the methods of Littlewood et al. (2017), which yielded a calcite with 6.52 Wt.% Sr. This was mixed into a composite of Ordinary Portland Cement (OPC) and Ground Granulated Blast Furnace Slag (GGBFS) and placed on a ball mill for 1 hour to ensure good mixing. 20 g of the subsequent cement blend was then thoroughly mixed with 10 g DIW to form a uniform paste which was cast in 50 ml cylindrical polypropylene tubes. Casting was carried out in a CO_2 free fume cupboard to allow ^{14}C in the sample to be tracked.

After curing for a set period of time (0.5,1,7,28 days) the sample was crushed and and dried using Isopropyl Alcohol (IPA), ether and a hot plate. At the end point (28 days) another sample was prepared using a low speed isomet to cut a slice of the cement cylinder which was embedded in resin for analysis on a SEM-EDS.

3.1.4 Filtration

All sections of this work have involved separating calcite from solutions. To achieve this a Buchner vacuum filter with Sartorius Stedim Polycarbonate Track-Etch Membrane filter paper was used. Precipitate was rinsed with IPA to remove water and stored in a desiccator.

3.2 Analytical Techniques

3.2.1 Brunauer, Emmet, and Teller (BET)

The BET technique was used to measure the surface area of precipitates throughout this study. BET relies on the adsorption of nitrogen gas to the sample at the boiling point of nitrogen (77 K). Under these conditions it is assumed that the nitrogen forms a mono-layer over the sample surface and that its adsorption is homogeneous across the surface of the crystal. With these assumptions the amount of absorbed nitrogen can be linked to the surface area of the precipitate.

The linear BET equation is presented in (Eq. 3.1), where v is the volume of adsorbed gas, v_m is the volume of the monolayer, p is the pressure of the gas at equilibrium,p_0 is the pressure at saturation while c is the BET constant. Once plotted the volume of adsorbed gas is equal to 1/(slope+intercept). Which allows the the surface area to be calculated with (Eq. 3.2), where, N is Avogadro's number A is the Surface area of a gas molecule, m is the mass of sample and 2240 is the volume of one mole of gas at standard temperature and pressure (Brame and Griggs, 2016).

$$\frac{1}{v[(\frac{p}{p_0})-1]} = \frac{c-1}{v_m c} \times (\frac{p}{p_0}) + \frac{1}{v_m c} \tag{3.1}$$

$$S = \frac{v_m NA}{2240 \times m} \tag{3.2}$$

3.2.2 Flow Injection Analysis (FIA)

Total Inorganic Carbon was analysed using flow injection analysis methods modified after (Hall and Aller, 1992).

Two eluent streams were used, one comprising of 10 mM NaOH and the second comprising HCl. The strength of the HCl stream needs to be adjusted depending on the alkalinity of the samples used. Ranging from 10-30 mM for fresh water samples, to 100 mM for high pH samples (pH=12). The NaOH was made fresh each day using MQ water that had been bubbled with N_2 to prevent CO_2 in-gassing. These streams were driven by a peristaltic pump operating at 0.86 ml min^{-1} into the reaction block.

The streams feed into the Flow Injection Analysis (FIA) cell, comprising of 2 perspex blocks with a groove for fluid flow (Figure 3.1). A strip of PTFE tape was placed between the blocks to separate the groove into 2 channels, with the NaOH and HCl occupying separate channels. Injecting a sample into the acid stream causes all the TIC to be converted to CO_2. This CO_2 is able to travel across the PTFE tape where it dissolves in the NaOH. The dissolution of the CO_2 in the NaOH causes a change in it's conductivity which is measured and quantified by a conductivity meter, this change in conductivity can be compared to a series of standards to give the TIC concentration in

the sample (Hall and Aller, 1992).

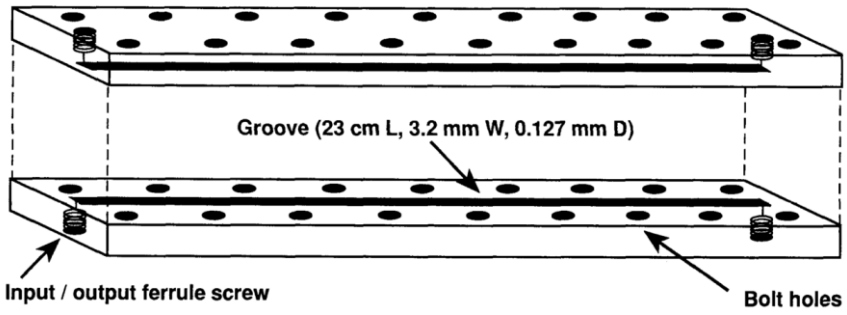

Figure 3.1: Schematic of FIA cell taken from (Hall and Aller, 1992)

Samples of approximately 1 ml were taken, passed through a 0.2 μm Minisart PES syringe filter and stored in microcentrifuge tubes at -10 °C to prevent degassing of CO_2. After thawing at room temperature for 1-2h the samples were withdrawn with a 1 ml syringe and injected into a 0.2 ml sample loop. The HCl flow path was switched to pass through this loop and mix with the sample. Standards were prepared using Na_2CO_3 solutions at a range of concentrations bracketing the expected sample range. These were made fresh prior to the analysis using MQ water which had been purged with Nitrogen to eliminate any dissolved CO_2. With this technique 95 % confidence limits of $\pm$0.4 mM were achieved.

3.2.3 Inductively Coupled Plasma Optical Emission Spectrometry

Ca, Mg, Sr, Na and S concentration was measured by ICP-OES on a ThermoFisher iCAP 7400 ICP-OES Analyzer.

ICP-OES is able to quantify the concentration of a range of elements in a solution by nebulizing the sample into an inductively coupled argon plasma at 5000-10000 K.

The high temperature vaporizes the sample, individual elements are ionized and their electrons excited from the ground state. As these electrons relax to their ground state certain characteristic wavelengths are emitted which are picked up and quantified by an optical emission spectrometer (Hou Xiandeng, 2000).

Samples were prepared by removing an aliquot from the reaction vessel and passing through a 0.2 μm Minisart PES filter into a microcentrifuge tube. 0.5 ml of this filtered aliquot was removed via pipette and added to 9.5 ml of ICP grade nitric acid. In experiments were ^{14}C was present after mixing with acid the sample was left un-capped for 10 mins to allow ^{14}C to be de-gassed.

3.2.4 Liquid Scintillation Counting (LSC)

Liquid scintillation counting was carried out using a Tri-Carb 2100TR liquid scintillation counter, PerkinElmer, was used to detect ^{14}C and ^{90}Sr activity in samples.

In LSC the emission of radioactivity from a sample is measured by first suspending it in a solvent alongside an emulsifier which ensures proper mixing and intimate contact between the solvent and the radionuclide. As beta particles are emitted solvent molecules become excited. This energy is conducted to a fluor molecule which is capable of converting the energy received from the decaying radionuclide to light. The intensity of the light emitted can be correlated to the energy of the beta particle which can be used to differentiate different sources of radiation.

There are a number of factors which may interfere with LSC. The efficiency of energy transfer from the radioactive decay event to the fluor molecule may be reduced by a

process called Quenching, which may be either chemical or optical. Chemical quenching is a result of energy loss between the emission from the radionuclide and the emission of light energy from the fluor molecule. After the energy has been converted to light by the fluor it's energy my be decreased by interactions with the solute or vial material, this is Optical quenching. The Tri-Carb 2100TR quantifies the degree of quenching a sample has undergone by using a ^{133}Ba external standard. This standard emits a known amount of gamma radioactivity, which in turn generates Compton electrons. These electrons interact with the scintillant as beta particles and are counted. By subtracting the sample counts from the Compton counts the counts due to the external standard is derived and this is compared to the theoretical spectrum which allows the effects of quenching to be accounted for.

Hionic-Fluor cocktail was used to count ^{14}C, due to its advertised efficiency with alkaline samples, high ionic strength tolerance and fast chemiluminescence decay (Perkin-Elmer). Energy from the ^{14}C nucleus was measured in the band 10-156 eV.

Samples for analysis in Hionic-Fluor were prepared by first adding 100 μl of saturated NaOH solution to 9 ml of Hionic-Fluor. Next an aliquot was removed from the reaction vessel and passed through a 0.2 μm Minisart Polyethersulfone (PES) filter into a microcentrifuge tube. 0.5 ml of this filtered aliquot was removed via pipette and transferred to the vial. Effort was made to minimise the amount of light the sample was exposed to, however all samples were dark calibrated for 24 h to minimise any effects. The LSC outputs the amount of counts the detector made per minute this was converted to sample activity by Eq. 3.3.

$$Activity = \frac{Count\ rate}{efficiency}/60 \tag{3.3}$$

3.2.5 Scanning Electron Microscopy (SEM)

A light microscope relies on focusing light waves in order to create a magnified image of a sample. In SEM the light is replaced with electrons which are accelerated at 2-1000 keV which gives significantly smaller wavelengths than that of light (Vernon-Parry, 2000). In the FEI Quanta 650 FEG SEM, used for imaging in this study, a field emission gun is used as the source of electrons. An electric current is applied to a needle formed from single crystal of tungsten. This results in a strong electric field forming at the ultra fine tip. Electrons are drawn by this current and flow off the tip towards the anodes. Two anodes are used which accelerate the electrons towards the sample. A vacuum of $>10^{10}$ Torr is required to stabilise the electron emission (Zhou et al., 2007).

As the high energy beam of electrons strike the sample surface they will interact with the top 1 μm of the sample. Some of the incident electrons will be deflected with minimal energy loss to the sample through an angle of >90°. These electrons are called backscattered electrons (BSE). Other electrons will interact more substantially with the sample, imparting energy significant enough to expel an electron from an atom within the sample. These expelled electrons are called secondary electrons (SE) (Vernon-Parry, 2000).

The SE signal is primarily used to form an image of the sample. These electrons have a lower energy relative to BSE and thus only escape from the upper portion of the sample

surface, giving greater resolution. The BSE signal may be used for imaging although, due to the greater depth of penetration a lower resolution is achieved. BSE however, are able to give compositional information on a sample. The proportion of electrons which will be backscattered towards the source is a function of the positive charge in the nucleus of the target atom. Therefore atoms with a higher atomic number will produce greater backscatter signals and result in these areas appearing brighter (Zhou et al., 2007).

3.2.6 Energy Dispersive X-Ray Spectroscopy (EDX)

During the emission of a SE a void is left within the electron orbital called a core hole. This leaves the atoms in an unstable position which is solved by an outer shell electron dropping to fill the void. As this electron falls a characteristic X-Ray photon will be produced. The energy of these X-Rays can be analysed to provide valuable information about the chemical composition of the sample (Zhou et al., 2007). X-ray photons may be emitted from anywhere within the interaction volume of the electron beam which results in a slightly lower resolution for this technique than for SE image analysis (Vernon-Parry, 2000).

3.2.7 Thermo-Gravimetric Analysis (TGA)

Thermogravimetric analysis was used in Chapter 7 in order to determine the amount of $CaCO_3$ that was dissolved during cement hydration. During TGA a sample is heated from 20-1000 °C in a crucible which is situated on a balance. As the sample passes through certain temperature thresholds thermal decomposition of phases within the

sample will occur. For example calcium carbonate will decompose at approximately 450 °C to CaO and CO_2. The mass loss of the sample is measured, which for $CaCO_3$ can can ascribed to CO_2 loss. This is then converted to the % calcite in the sample using the tangent method Eq. 3.4 (Adu-Amankwah et al., 2017). Where m_0 and m_1 are the weight loss before and after the calcium carbonate decomposition, m_{1000} is the mass remaining at 1000 °C and M_{CO_2} is the molar mass of CO_2.

$$\%W = \frac{(m_0 - m_1)}{m_1} \times 100 \tag{3.4}$$

$$\%CaCO_3 = \frac{\%W \times (100/m_{1000})}{M_{CO_2}} \times 100 \tag{3.5}$$

3.2.8 X-ray Diffraction (XRD)

Different crystal morphologies may be characterised by the distinctive planes that their crystal lattices form. One way of measuring these lattice planes and thus determining the crystal morphologies present in a powder sample is through XRD.

X-rays which are fired at a powder sample will be reflected due to interactions with lattice ions. At most angles of incidence the reflected X-rays will interfere with each other resulting in background noise, however, at some angles of incidence the X-rays will synchronise and reinforce each other to produce an increase in the reflected X-Ray intensity. The angles at which this reinforcement will occur an be calculated using Bragg's law (Eq. 3.6) which states that for constructive interference to occur the lattice spacing must be such that the flight distances of X-rays reflecting from parallel lattice

layers will differ by an integer number of wavelengths (Bragg, 1913). By measuring the angles at which different peaks form it is possible to characterise the crystal lattice under examination. For example the XRD spectra of the three carbonate phases are presented in Fig. 3.3.

$$n\lambda = 2d\sin\theta \tag{3.6}$$

XRD peaks rely on the D spacing between planes of atoms. If an atom is replaced by an atom with a larger or smaller ionic radius there will be a localised strain resulting in either contraction or expansion of the D spacing. This altered D spacing results in changes in the peak position. As the crystal lattice is compressed the diffraction angle shifts to smaller $2\theta^{\circ}$ (Warren and Averbach, 1950, 1952).

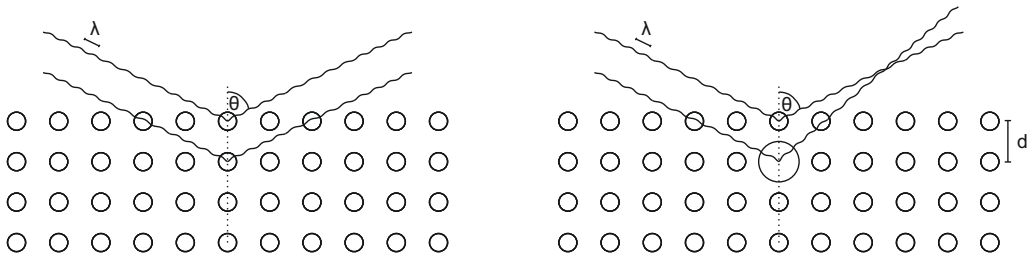

Figure 3.2: The role of lattice parameters in generating XRD signals

3.2.9 X-Ray Absorption Spectroscopy (XAS)

For experiments presented in chapter 6 of this manuscript X-Ray Absorption Spectroscopy (XAS) was carried out at B18, Diamond Light Source, Harwell, UK. This technique was selected in order to probe the local coordination environment of Sr within the calcite lattice.

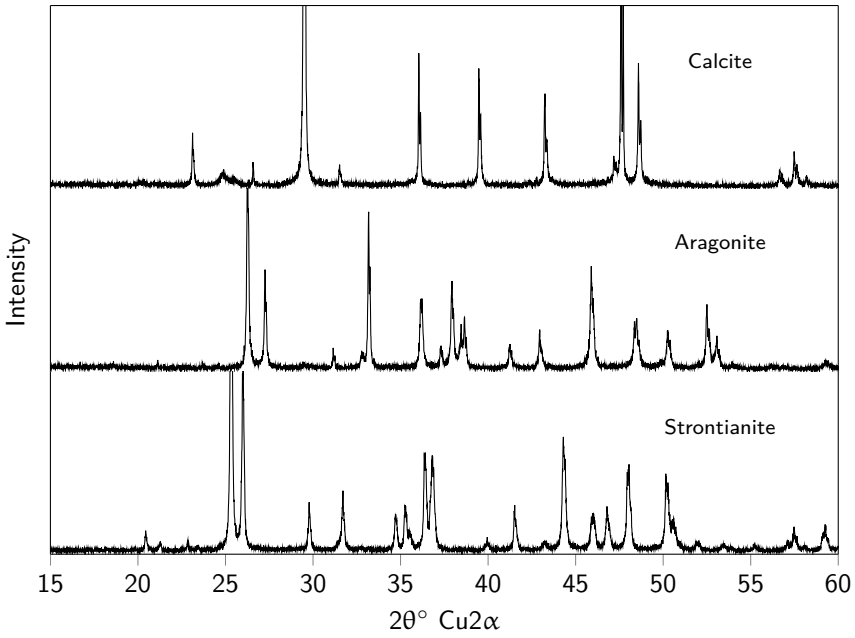

Figure 3.3: XRD data for Calcite and Aragonite using data from rruff.info (Downs et al.)

Synchrotron radiation

The Diamond Light Source is a synchrotron that is capable of generating intense X-Rays which enable the studying atomic scale phenomenon. These X-Rays are formed by generating particles using an electron gun which are subsequently accelerated through a Linac and Booster synchrotron before being stored in a storage ring half a kilometre in circumference (Fig. 3.4).

The storage ring at Diamond consists of a series of 48 straight segments connected with bending magnets. As the particles reach speeds approaching the speed of light they begin to emit large amounts of radiation, most of which is in the direction of particle movement. The bending magnets are used to manipulate the beam path to meet the next straight line segment however as this occurs energy is emitted as X-Rays which continue to travel tangentially to the previous straight line segment. This energy comprises a

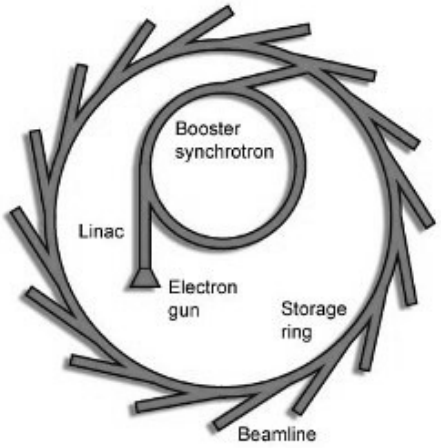

Figure 3.4: Schematic of a Synchrotron (Diamond-Light-Source)

broad spectrum and is subsequently tuned with a monochromator to filter out unwanted energies. The resultant beam is then focused onto a sample and the amount of energy absorbed by the sample is measured (Alp, E.E., Mini, S.M. and Ramanathan, 1990; Diamond-Light-Source).

Synchrotron analysis

During analysis the sample is exposed to X-Rays at a range of energies. If the energy of these X-Rays is insufficient to excite core electrons there will be little absorption by with the sample, this defines the pre-edge region of an XAS spectrum (Fig. 3.5). As the X-Ray energy reaches that required to excite core electrons a sharp increase in adsorption is observed, called the adsorption edge. The adsorption edge is named relative to the electron that is promoted. In this study the Sr K-edge was used which represents the promotion of the electron in the 1st shell ($1s^1$) of the Sr atom (Penner-Hahn, 2003). The core binding energies of a given atom are well known (the binding energy of the Sr K 1s electron is known to be 16105 eV) which means that XAS data collection can be tuned to target a certain atom within the sample (Thompson et al.,

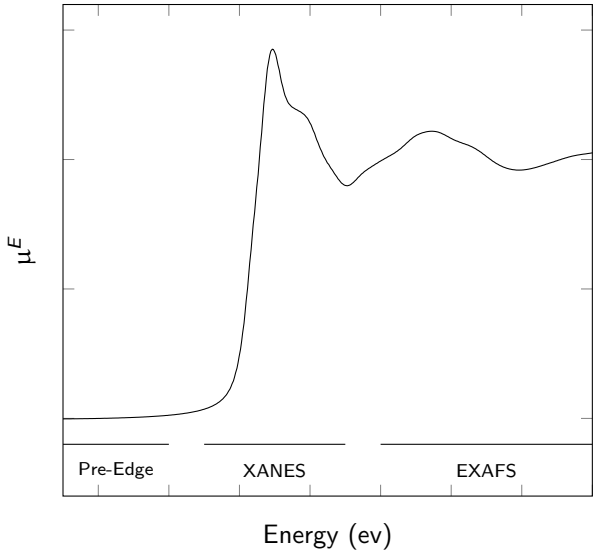

Figure 3.5: Relative positions of the Pre-Edge, XANES, and EXAFS regions on a XAS spectrum Adapted from (Alp, E.E., Mini, S.M. and Ramanathan, 1990)

2009).

When a core electron is excited it leaves behind a core hole which is highly unstable and will be rapidly filled by one of two mechanisms. Both involve a higher energy electron dropping down to fill the hole, this can either result in the emission of a characteristic fluorescence energy or the emission of a second electron (termed Auger emission) (Newville, 2014).

XAS data can be collected in one of two modes, transmission and fluorescence. In transmission mode the intensity of the X-Ray beam is measured before and after interacting with the sample, this can be used to determine the amount of energy absorbance by the sample Eq. 3.7 where $\mu(E)$ is the absorption coefficient and I is the Intensity (Newville, 2014).

$$\mu(E) = \ln \frac{I_{Initial}}{I_{Final}} \tag{3.7}$$

Fluorescence is used for samples with lower concentrations of the target species. Absorbance is determined from the intensity of X-Ray fluorescence produced during the relaxation of a higher energy electron to fill a core hole Eq. 3.8 (Newville, 2014).

$$\mu(E) \propto \frac{I_{Fluorescence}}{I_{Final}}/ \tag{3.8}$$

XANES

The analysis of XAS data near to the adsorption edge is termed X-Ray Adsorption Near Edge Structure. Due to the lower kinetic energy of photoelectrons in the XANES region they have a longer mean free path, allowing them to interact with multiple neighbouring atoms. The greater number of scattering events creates a complex signal but allows for information to be gained about the oxidation state and bond angles of the target atom (Alp, E.E., Mini, S.M. and Ramanathan, 1990; Penner-Hahn, 2003).

EXAFS

At energies above the binding energy of the core electron photoelectrons will be emitted from the atom. These will interact with surrounding atoms, called backscattering atoms. This interaction generates waves which will interact (either constructively or destructively) with each other and producing a variation in the absorption coefficient. Important information can be gained by studying these interactions, such as the bond lengths and coordination of the target atom and the neighbouring atoms (Penner-Hahn, 2003).

EXAFS data is usually plotted in terms of the wave number of the photo-electron (k) rather than the X-Ray energy (Eq. 3.9) where E_0 is the absorption edge energy, m is the electron mass and $\hbar$ is Planks constant.

$$k = \sqrt{\frac{2m(E - E_0)}{\hbar^2}} \tag{3.9}$$

The $\chi^{(k)}$ is calculated by subtracting the baseline absorption (μ_0) from the observed absorption coefficient (μ) to isolate the effects of EXAFS absorptions and subsequently dividing by the baseline to normalise (Eq. 3.10). Since the baseline cannot be measured an approximation can be made by fitting a spline through the data (Penner-Hahn, 2003). The number of scattering atoms can be derived from the amplitude of the oscillations in the $\chi^{(E)}$ while the distance between the absorber and scatterer is inversely proportional to the frequency of the oscillations (Newville, 2014).

$$\chi^{(E)} = \frac{\mu - \mu_0}{\mu_0} \tag{3.10}$$

The $\chi^{(k)}$ is calculated by the EXAFS equation (Eq. 3.11). This equation contains two key terms that describe the local atomic environment of the target atom. N is the number of atoms surrounding the target and R, their distance from the neighbouring atom. These are coupled with scattering properties $f(k)$ and $\sigma(k)$, and σ^2, the disorder in the distance between the neighbours and the target.

EXAFS data commonly displays a decrease in the amplitude of its oscillations at higher k values. To remedy this the EXAFS is commonly k weighted, in this study a k-weight of 3 was used to amplify the signal at higher k value (Newville, 2014). The fourier

transform of the $\chi(k)$ signal is taken which converts the wave number (k) to (R). A window is selected over which to correct the sample for our analysis a k-range of 3-13 was selected. In the transformed data the number of peaks represent the number of backscattering atoms surrounding the Sr atom. (Rehr et al., 2017).

$$\chi^{(k)} = \sum_j \frac{N_j f_i(k) e^{-2k^2\sigma_j^2}}{kR_j^2} \sin[2kR_j + \delta_j(k)] \tag{3.11}$$

Synchrotron Technique

Five samples containing 0.02, 0.37, 2.45, 4.35, and 9.36 Wt. % Sr were taken to Diamond for analysis. XAS data was collected on the Sr K-edge, using transmission mode and in fluorescence mode for low concentration samples, using a 9 element Ge solid state detector. Samples were mounted in a liquid nitrogen cryostat (80 K) to improve the signal to noise ratio.

Multiple scans were summed and averaged in Athena (version 0.9.25) (Ravel and Newville, 2005) in order to maximise the signal to noise ratio. These scans were then normalised and compared to spectra for a series of standards. EXAFS data was fitted in K-space using Artemis (version 0.9.25) (Ravel and Newville, 2005) using a published calcite model structure (Markgraf and Reeder, 1985) as a basis and performing a series of iterative refinements in order to minimise the Debye-Waller factor and R-factor.

Bibliography

Adu-Amankwah, S., Zajac, M., Stabler, C., Lothenbach, B., Black, L. (2017). Influence of limestone and anhydrite on the hydration of Portland cements. *Cement and Concrete Research*, pp. 96–109.
URL: *http://dx.doi.org/10.1016/j.cemconres.2017.05.013*

Alp, E.E., Mini, S.M. and Ramanathan, M. (1990). Synchchrotron X-ray Sources and New Opportunities in the Soil and Environmental Sciences: Workshop Report. *US Department of Energy*.

Boylan, A.A., Stewart, D.I., Graham, J.T., Trivedi, D., Burke, I.T. (2016). Mechanisms of inorganic carbon-14 attenuation in contaminated groundwater: Effect of solution pH on isotopic exchange and carbonate precipitation reactions. *Applied Geochemistry*, pp. 1–11.
URL: *http://dx.doi.org/10.1016/j.apgeochem.2016.12.006*

Bragg, W.H. (1913). The Reflection of X-rays by Crystals. *Proceedings of the Royal Society A: Mathematical, Physical and Engineering Sciences*, **89**(610), pp. 246–248.
URL: *http://www.jstor.org/stable/93501*

Brame, J., Griggs, C. (2016). Surface Area Analysis Using the Brunauer-Emmett-Teller (BET) Method: Scientific Operation Procedure Series : SOP-C.

Diamond-Light-Source (). How Diamond Works.
URL: *http://www.diamond.ac.uk/Home/About/How-Diamond-Works.html#*

Downs, B., Robinson, S., Yang, H., Mooney, P. (). rruff.info.

Garrett, D.E. (1992). *Natural Soda Ash: Occurrences, Processing and Use*. Van Nostrand Reinhold.

Graham, J. (2013). ERT Trial Groundwater Analysis – Rounds 16 – 19. NNL Technical Memorandum LP06489/06/10/07. Technical report, NNL.

Hall, O.J., Aller, R.C. (1992). Rapid, small-volume, flow injection analysis for ΣCO2 and NH4+ in marine and fresh waters. *Limmology and Oceanography*, **37**(5), pp. 1113–1119.

Hou Xiandeng, J.B.T. (2000). Inductively Coupled Plasma–Optical Emission Spectrometry. In *Encyclopedia of Analytical Chemistry R.A. Meyers*, 1. John Wiley & Sons Ltd, pp. 9465–9485.

Littlewood, J.L., Shaw, S., Peacock, C.L., Bots, P., Trivedi, D., Burke, I.T. (2017). Mechanism of Enhanced Strontium Uptake into Calcite via an Amorphous Calcium Carbonate Crystallization Pathway. *Crystal Growth and Design*, **17**(3), pp. 1214–1223.

Markgraf, S., Reeder, R. (1985). High-temperature structure refinements of calcite and magnesite. *Am. Mineral.*, **70**, pp. 590–600.
URL: *http://scholar.google.com/scholar?hl=en&btnG=Search&q=intitle:High-temperature+structure+refinements+of+calcite+and+magnesite#0*

Moorehead, D.R. (1986). Cementation by the carbonation of hydrated lime. *Cement and Concrete Research*, **16**(5), pp. 700–708.

Newville, M. (2014). Fundamentals of XAFS. *Reviews in Mineralogy and Geochemistry*, **78**(1), pp. 33–74.
URL: *http://rimg.geoscienceworld.org/cgi/doi/10.2138/rmg.2014.78.2*

Penner-Hahn, J.E. (2003). *X-ray Absorption Spectroscopy*. Elsevier Ltd.

Perkin-Elmer (). Hionic-Fluor.
URL: *http://www.perkinelmer.com/product/hionic-fluor-2-5-l-6013319*

Ravel, B., Newville, M. (2005). ATHENA, ARTEMIS, HEPHAESTUS: Data analysis for X-ray absorption spectroscopy using IFEFFIT. In *Journal of Synchrotron Radiation*, 4. pp. 537–541.

Rehr, J.J., Kas, J.J., Vila, F.D., Newville, M. (2017). *XAFS Techniques for Catalysts, Nanomaterials, and Surfaces*.
URL: *http://link.springer.com/10.1007/978-3-319-43866-5*

Thompson, A., Attwood, D., Gullikson, E., Howells, M., Kim, K.J., Kirz, J., Kortright, J., Lindau, I., Liu, Y., Pianetta, P., Robinson, A., Scofield, J., Underwood, J., Williams, G., Winick, H. (2009). X-ray data booklet.

Vernon-Parry, K. (2000). Scanning electron microscopy: an introduction. *III-Vs Review*, **13**(4), pp. 40–44.

Warren, B.E., Averbach, B.L. (1950). The effect of cold-work distortion on x-ray patterns. *Journal of Applied Physics*, **21**(6), pp. 595–599.

Warren, B.E., Averbach, B.L. (1952). The separation of cold-work distortion and particle size broadening in x-ray patterns [1]. *Journal of Applied Physics*, **23**(4), p. 497.

Zhou, W., Apkarian, R.P., Wang, Z.L. (2007). Fundamentals of Scanning Electron Microscopy. *Scanning Microscopy for Nanotechnology*, pp. 1–40.

Part III

Experimental Data Chapters

Chapter 4

Coprecipitation of ^{14}C and Sr with carbonate precipitates: The importance of reaction kinetics and recrystallization pathways

4.1 Summary

This study investigated the simultaneous removal of Sr^{2+} and $^{14}CO_3^{2-}$ from (pH >12) $Ca(OH)_2$ solution by the precipitation of calcium carbonate. Initial Ca^{2+}:CO_3^{2-} ratios ranged from 10:1 to 10:100 (mM: mM). Maximum removal of ^{14}C and Sr^{2+} both occurred in the system containing 10 mM Ca^{2+} and 1 mM CO_3^{2-} (99.7% and 98.6% removal, respectively). A kinetic model is provided that describes ^{14}C and Sr removal in terms of mineral dissolution and precipitation reactions. The removal of ^{14}C was achieved during the depletion of the initial TIC in solution, and was subsequently significantly affected by recrystallization of a calcite precipitate from an elongate to isotropic morphology. This liberated >46% of the ^{14}C back to solution. Sr^{2+} removal

occurred as Ca^{2+} became depleted in solution and was not significantly affected by the recrystallization process. This reaction could form the basis for low cost remediation scheme for ^{90}Sr and ^{14}C in radioactively contaminated waters (<$0.25 reagent cost per m^3 treated).

4.2 Introduction

The mining, milling and refining of nuclear fuels, accidents occurring during the operation of nuclear power facilities, and nuclear fuel reprocessing have left a legacy of groundwater pollution by radionuclides (Kersting et al., 1999; Naftz et al., 2002; Panias et al., 2005). Radioactively contaminated ground and groundwater pose a potential threat to a number of receptors including drinking water resources, humans and non-human biota (Palmisano and Hazen, 2003; Stewart et al., 2006). Also the presence of even low levels of groundwater pollution will require continued oversight, and thus may negatively impact on the restoration of nuclear sites to beneficial use (NDA, 2013). ^{90}Sr is a high yield fission product that if ingested can substitute for Ca in bone (Nielsen, 2004). It is mobile in groundwater as the $^{90}Sr^{2+}$ ion and is a contaminant of concern at nuclear sites across the world (Gray et al., 1995; Saunders and Toran, 1995; Standring et al., 2002; Thompson and Steefel, 2010). ^{14}C is a long lived neutron capture product that can be taken up by biota during assimilative respiration and growth Amiro and Ewing (1992). ^{14}C is an important component of all radioactive wastes and is potentially very mobile in groundwater as $H^{14}CO_3^-$. As a result ^{14}C is a contaminant of concern at many nuclear sites (Aquilonius and Hallberg, 2005; Dias et al., 2009; Magnusson et al., 2007; Roussel-Debet et al., 2006), and is known to have been released in large

quantities at some sites (e.g. ^{14}C emissions averaged 8.13 TBq year^{-1} between 1994 and 2013 at the UK Sellafield nuclear site Tierney et al. (2016)).

At Sellafield, off-site measurements of groundwater ^{90}Sr and ^{14}C activities were below detection limits in 2013. However, in the same year within the site boundary, activities of up to 42 kBq L^{-1} of ^{90}Sr and 44 kBq L^{-1} of ^{14}C were reported (well above the WHO drinking water guidelines of 0.1 and 0.01 kBq L^{-1} respectively)(Stamper et al., 2014). While the WHO guidelines are not regulated concentration limits, treatment of these groundwaters may ultimately be necessary prior to eventual site closure. ^{90}Sr (as Sr^{2+}) and ^{14}C (as HCO_3^-) are in places co-located, therefore, a technique that can remove both ions in a single process would have advantages over other methods of groundwater treatment. Cation exchange media (e.g. zeolites and resins) are the primary technology currently used to remove ^{90}Sr from nuclear plant effluents, and to treat incoming plant make-up water (Marinin and Brown, 2000; National-Nuclear-Laoratory). Their operation relies on the displacement of weakly bound cations from a matrix by aqueous $^{90}Sr^{2+}$ ions. The approach can be very effective for the removal of high concentrations of ions from effluents; however, their applicability to low concentrations in groundwater is potentially problematic owing to the presence of competing ions (Barton et al., 2004). Contaminated groundwater tends to contain $^{90}Sr^{2+}$ ions in concentrations of ng/L-pg/L whereas other divalent metals such as Ca^{2+} and Mg^{2+} are present in mg/L concentrations. The competition from these groundwater ions for exchange sites can greatly reduce the effectiveness of any proposed treatment scheme based on ion exchange media. In addition, anionic contaminants such as ^{14}C in bicarbonate and carbonate ions (HCO_3^- and CO_3^{2-}) would require a separate anion exchange process

with similar competing ion issues from non-radioactive species.

Induced carbonate precipitation is an alternative approach that could potentially remove both ^{90}Sr and ^{14}C in a single process (Fujita et al., 2000; Mitchell and Ferris, 2005; Achal et al., 2012). Calcium hydroxide ($Ca(OH)_2$) is a relatively low cost reagent that is produced on a large scale for use in the construction and agricultural industries (National-Lime-Association). Addition of calcium hydroxide to water containing HCO_3^- or CO_3^{2-} results in the rapid precipitation of calcium carbonate (Eq. 4.1–4.4)(Clark et al., 1992). Rapid precipitation of calcium carbonate can result in the co-precipitation of other metal ions(Curti, 1997).

$$Ca(OH)_{2(s)} \rightleftharpoons Ca^{2+}_{(aq)} + 2OH^- \tag{4.1}$$

$$CO_{2(g)} \rightleftharpoons CO_{2(aq)} \tag{4.2a}$$

$$CO_{2(aq)} + OH^- \rightleftharpoons HCO^-_{3(aq)} \tag{4.2b}$$

$$H_2CO_{3(aq)} \rightleftharpoons HCO^-_{3(aq)} + H^+ \rightleftharpoons CO^{2-}_{3(aq)} + H^+ \tag{4.2c}$$

$$Ca^{2+}_{(aq)} + CO^{2-}_{3(aq)} \rightleftharpoons CaCO_{3(s)} \tag{4.3}$$

Thus the net reaction is:

$$Ca(OH)_2 + CO_2 \rightleftharpoons CaCO_3 + H_2O \tag{4.4}$$

Coprecipitation of trace metals in carbonates occurs because of a similarity in the valence and ionic radius of the major carbonate M^{2+} ion (Ca^{2+}) and a range of minor

ions (Sr^{2+}, Fe^{2+}, Cd^{2+}, Cu^{2+}). These minor ions may replace calcium within the carbonate lattice or adsorb to the growing mineral, causing their accumulation in the solid phase (Curti, 1997). Much of the early work on coprecipitation into carbonates focused on marine limestone and calcifying organisms (Holland et al., 1964; Katz et al., 1972; Pingitore Jr et al., 1992). When treating ^{90}Sr and ^{14}C in contaminated groundwater sub-saturated with respect to carbonate it is likely that the precipitate formed will undergo eventual dissolution. Therefore in these regimes it is likely that the groundwater will need to be extracted and treated ex-situ to give better process control, improve efficiency and facilitate the safe disposal of the radionuclide containing carbonates that are produced.

One of the factors which may affect the efficiency of ^{90}Sr and ^{14}C incorporation into carbonates will be the crystallization pathways the precipitate undergoes. Neo-formed precipitates are often unstable and their recrystallization can occur over time (Fernández-Díaz et al., 2010). Due to wide interest in the fundamentals of carbonate nucleation and growth, the crystallisation pathways that occur during the precipitation of aqueous Ca^{2+} and CO_3^{2-} and eventual transformation to thermodynamically stable calcite have received a lot of attention (Zhang and Dawe, 2000; Gebauer et al., 2008; Nielsen et al., 2014). Ostwald's rule of stages describes one of the common causes of morphological transitions during precipitation (Ostwald, 1897). This rule states that during nucleation the first formed phase is the most kinetically accessible, but this may not be the most thermodynamically stable. As precipitation progresses this kinetically accessible phase will transform to a thermodynamically stable one, potentially thorough a series of intermediaries. The consequences of recrystallization for trace metal co-precipitation

have not yet been fully determined.

This paper reports an investigation of ^{14}C-carbonate and Sr uptake during calcium carbonate precipitation in both closed systems and systems that were open to atmospheric CO_2. We have characterized the crystallization pathways that were observed and the associate effects on ^{14}C and Sr uptake. A simple kinetic model is then proposed which identifies the controlling factors at different stages of the alkaline precipitation process, and indicates reaction stages that control the rate of ^{14}C and Sr uptake. Finally, the implications of the experimental results for a low cost treatment scheme for $^{14}C/^{90}Sr$ contaminated groundwater are discussed.

4.3 Experimental Section

Calcium carbonate precipitation from alkaline solutions was investigated in triplicate batch experiments conducted in 500 ml polypropylene conical flasks (ThermoFisher Scientific, USA). The initial solution comprised of 100 ml of 0.01 M NaOH. This solution was used to provide an initial pH of 12 as it has been shown that at pH <10 atmospheric exchange of ^{14}C is significant (Boylan et al., 2016). Sr was added as $SrCl_2{\cdot}6H_2O$ to a concentration of 0.114 mM Sr^{2+} (10 ppm) and ^{14}C was added as $Na_2^{14}CO_3$ to an activity of 100 Bq ml^{-1}. These concentrations were used because they are easily measurable but remain close to the observed contamination levels at Sellafield (see Table 1 below). Natural groundwater Sr concentrations are low so the treatment strategy is to remove all aqueous Sr, thus it was unnecessary to use radiostrontium. However the possibility of CO_3^{2-}/HCO_3^- exchange with atmospheric

CO_2 meant it is important to understand the fate of aqueous ^{14}C. The solution was mixed by swirling on an orbital shaker. Calcium was then added as solid $Ca(OH)_2$ to a concentration equivalent to 10 mM, and simultaneously carbonate was added as Na_2CO_3 to concentrations of 1, 5, 10 and 100 mM. Thus the initial Ca^{2+}:CO_3^{2-} ratios were 10:1, 10:5. 10:10 and 10:100 (mM:mM) (hereafter referred to as [Ca]10:[CO3]1 etc...)

Air-permeable foam bungs were placed in the top of the conical flasks to prevent sample contamination, and the flasks were placed on an orbital shaker at 100 rpm for 200 h. Periodically the temperature and pH of the solution in the flask were measured and sub-samples were taken for chemical and mineralogical analysis. The sampling interval was increased from 30 s to 200 h as the experiment progressed to give data at approximately equal intervals of log(time).

Separate closed system experiments were carried out in 40 ml sealed reaction vessels with minimal headspace. These were ran for 24 h and sampled at the same time intervals as the open system experiments.

Chemical analysis

Temperature and pH were measured using an Orion 420 pH meter with a VWR SJ113 probe calibrated at pH 4.01, 7.0 and 10.01. All aqueous samples were filtered using 0.2 μm Polyethersulfone hydrophilic filters. Sub-samples for metal analysis (0.5 mL) were added to 9.5 mL of 0.1 M Aristar® grade HNO3 (VWR International, USA) for storage and analysed using ion-coupled plasma, optical emission spectrometer (Thermo iCAP 7400, Thermo Fisher Scientific, Inc, USA). Carbon-14 was measured by liquid

scintillation counting (Tri-Carb 2100TR, PerkinElmer, USA); sub-samples of 0.5 mL were added to 9 mL of Hionic Fluor Liquid Scintillation Cocktail (PerkinElmer, USA) and 100 μl of 2M NaOH and stored in the dark for 24 h before counting.

TIC (Total Inorganic Carbon) was analysed in a parallel series of experiments using the same starting conditions (excluding ^{14}C). Filtered aqueous samples were stored in a 1.5 ml Eppendorf vials and frozen to prevent degassing of CO_2. TIC determinations were made by Flow Injection Analysis (FIA) following the method of Hall and Aller (Hall and Aller, 1992).

Mineralogical analysis

A series of sacrificial experiments were carried out to recover solids for x-ray diffraction (XRD) and scanning electron microscope (SEM) analysis from the [Ca]10:[CO3]1 experiment. These employed the same starting conditions (excluding ^{14}C) as the precipitation experiments described above. Periodically an entire replicate was sacrificed and the solution was passed through a Buchner filter with Sartorius Stedim Polycarbonate Track-Etch Membrane filter paper. Solids were washed with isopropyl alcohol, and then stored in a desiccator.

The mineralogy of solids recovered by vacuum filtration was analysed using a Bruker D8 XRD with a Cu Kα source. Rietveld analysis (Rietveld, 1969) was carried out using Topas 4-2 to calculate relative proportions of carbonate polymorphs and $Ca(OH)_2$. The morphology of precipitates was observed using a FEI Quanta 650 FEG SEM. This also enabled observations to be made on changes in crystal size distribution and morphology, as well as looking for amorphous intermediaries.

4.4 Results and discussion

The pH of all the precipitation experiments displayed a similar pattern with time regardless of the initial Ca^{2+}:CO_3^{2-} molar ratio (Figure 4.1). In all cases the pH was initially fairly stable at a value 12.18 $\pm$ 0.26 for approximately 24 h, and then decreased with time until the end of the tests. The rate of pH change was more rapid in experiments with lower initial CO_3^{2-} concentrations. The experimental series displayed a systematic increase in final pH, from 8.99 for [Ca]10:[CO_3]1 to 10.08 for [Ca]10:[CO3]100. Temperature measurements indicated a temperature of 19.6 $\pm$ 0.8 during all experiments.

The Ca concentration varied systematically with the initial Ca^{2+}:CO_3^{2-} molar ratio. Experiments where Ca^{2+} was present in molar excess to the initial amount of CO_3^{2-} exhibited significant Ca^{2+} concentrations in solution (>10% Co) for at least the first 8 h, before this dropped to less than 1% Co. In contrast, the Ca^{2+} concentration in experiments where there were initially equal amounts of Ca^{2+} and CO_3^2-, or an excess of CO_3^{2-}, dropped rapidly to less than 1% Co over the first 5min. In all experiments the Ca^{2+} concentration reached a minimum of 11.6 μM $\pm$ 1.1, before there was a slight increase contemporaneously with the decrease in pH. The final Ca^{2+} concentration was 20.9 μM $\pm$ 9.7 in all tests.

The strontium concentration decreased from 114 μM to 0.02 μM $\pm$ 0.1 in all experiments. In all cases Sr removal from solution started after most of the Ca (>80%) had been removed from solution. The [Ca]10:[CO_3]5 experiment displayed a pause in Sr removal between 8 min–6 h. Strontium showed a similar remobilization to calcium

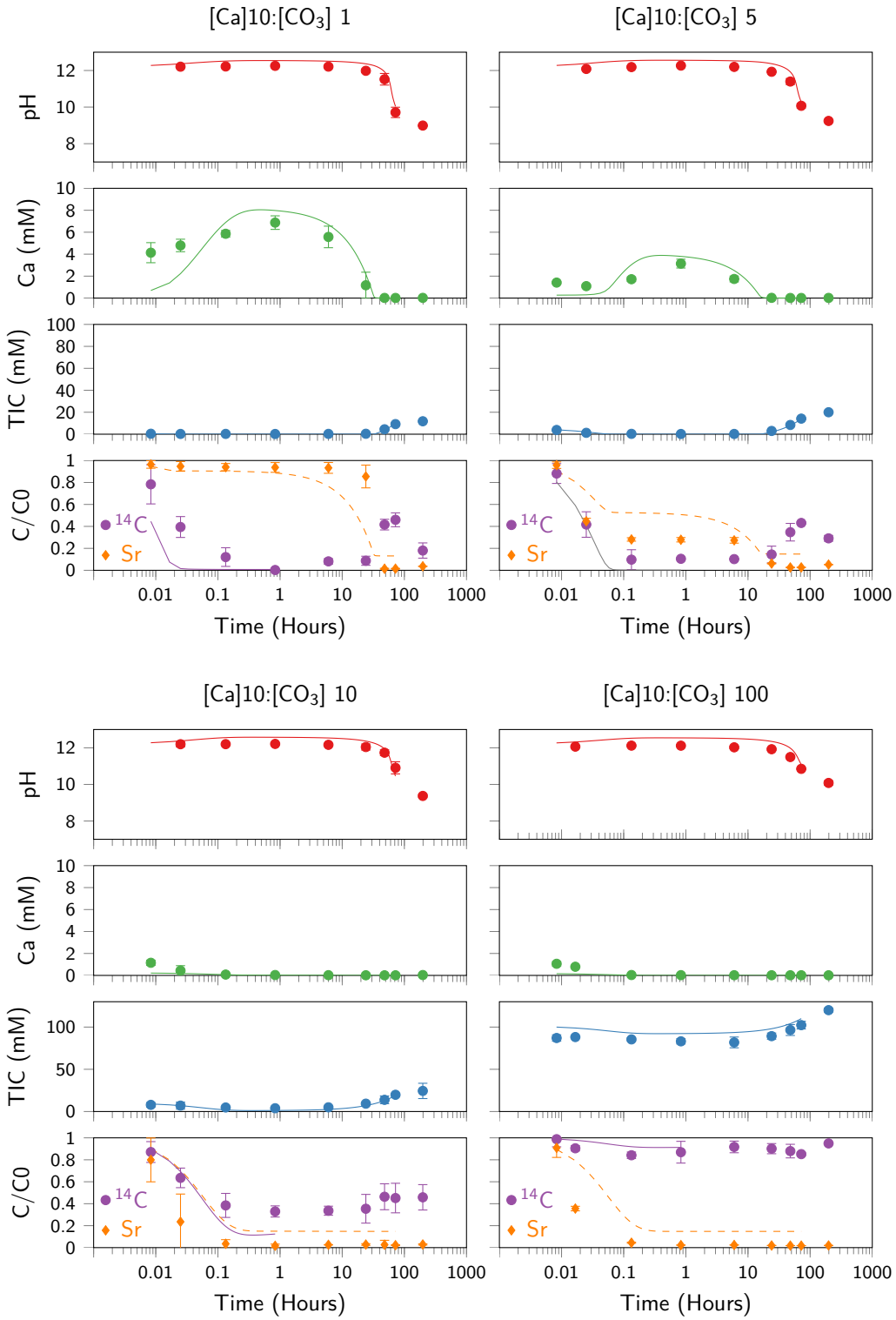

Figure 4.1: Solution composition for the open system experiments alongside model data computed in PHREEQC. The model for ^{14}C removal was run until max TIC depletion which occurred at 50min, after which in-gassing became important. All other data was modelled for 72 h.

after 100 h increasing from 0.02 μM $\pm$ 0.1 to 0.4 μM $\pm$ 0.2 by 200 h.

All experiments displayed an initial decrease in TIC concentration lasting until 8min in high Ca^{2+}:CO_3^{2-} molar ratios and 50min in experiments with low Ca^{2+}:CO_3^{2-} molar ratios. In experiments with high Ca^{2+}:CO_3^{2-} molar ratios the initial decrease in TIC was followed by an interval of uniformly low TIC after which TIC began to accumulate. Experiments with low Ca^{2+}:CO_3^{2-} molar ratios did not display this interval of uniform TIC concentration, instead showed immediate TIC accumulation following the initial depletion.

Carbon-14 removal varied systematically with the experimental conditions. Maximum removal (99.7%) was observed at 50min during the [Ca]10:[CO_3]1 experiment, however this experiment also displayed a significant remobilization starting after 50min, which reached a maximum after 72 h. Experiments with higher Ca^{2+}:CO_3^{2-} molar ratios displayed progressively less ^{14}C removal but with lower remobilization.

The XRD analysis of precipitate recovered from the [Ca]10:[CO_3]1 sacrificial experiments showed that the initial precipitate (t=1.5min) was calcite, and that this was the only new crystalline phase identified during the experiments (Appendix Figure A.1). SEM analysis indicates an elongate morphology characterized by an average length of 490 nm and width of 110 nm was present after 1.5min, which displayed growth along the elongate axis to 590 nm by 110 nm by 50min (Figure 4.2 and Appendix Figure A.2). After 50min the morphology of the precipitate changed, becoming more isotropic (460 nm by 410 nm), this transition was complete by 190 h.

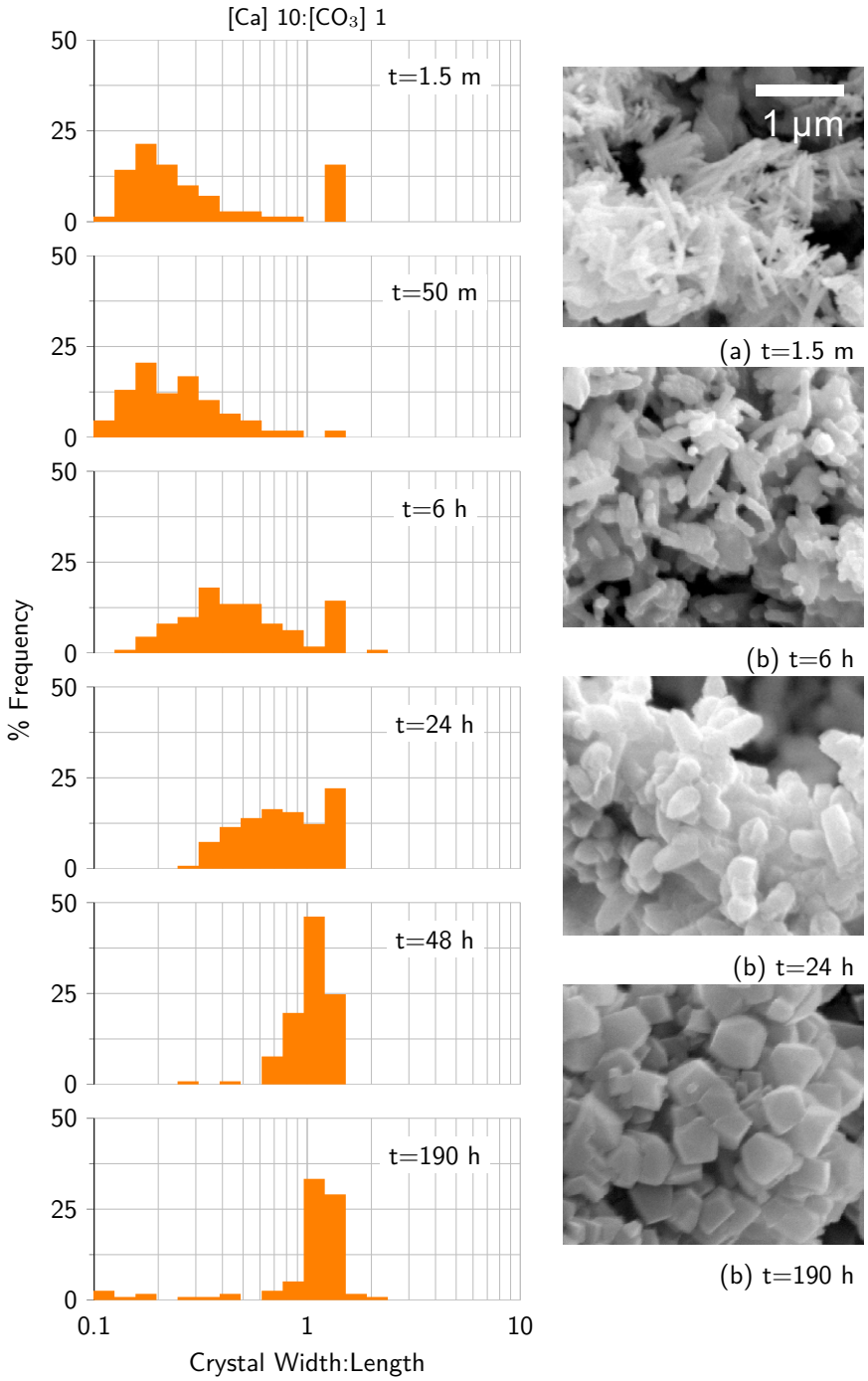

Figure 4.2: Histograms displaying crystal width:length ratios of >100 crystals at 6 time points throughout the [Ca]10:[CO_3]1 experiment, with key SEM images for illustration.

Closed system experiments (Figure 4.3) displayed a stable pH>12 throughout the experiments. Initial calcium trends were similar to those observed in the equivalent open system experiments; in experiments where there were initially equal amounts of

Ca^{2+} and CO_3^{2-}, or an excess of CO_3^{2-}, the Ca^{2+} concentrations reduced rapidly to less than 1% of initial concentrations (C_0) over the first 5min, but where Ca^{2+} was present in molar excess a significant aqueous Ca^{2+} concentrations developed over the first hour. However, in the closed [Ca]10:[CO_3]1 system there was no subsequent drop in aqueous Ca^{2+} concentration at longer time periods. Near complete strontium removal occurred the systems where [CO_3]$\geq$[Ca], but very little strontium removal was observed where Ca^{2+} was present in molar excess to CO_3^{2-}. A small amount of strontium was remobilized after 24 h in the experiment where initial Ca^{2+} and CO_3^{2-} concentrations were close to stoichiometric balance. The removal of ^{14}C was less effective in the closed system systems than in the equivalent open systems (e.g. a maximum of 90% removal was observed in the closed [Ca]10:[CO_3]1 system versus 99.7% removal in the open systems), but there was no significant remobilization of ^{14}C over time.

4.4.1 Interpretation

The pH of all the precipitation experiments was initially controlled by NaOH and the subsequent rapid dissolution of $Ca(OH)_2$. Where there was in-gassing of atmospheric CO_2, the pH was buffered downwards by hydroxylation (Eq. 4.2b), and the system transitioned to a carbonate buffered system after 24 h. Closed system experiments did not show this pH drop due to the lack of atmospheric CO2 in-gassing.

Calcium hydroxide was added as a solid but will have dissolved until it became saturated. The [Ca]10:[CO_3]1 and [Ca]10:[CO_3]5 experiments displayed an increase in the concentration of Ca^{2+} corresponding to this dissolution between 30s and 50min. The rate of increase will have been a function of both $Ca(OH)_2$ dissolution and cal-

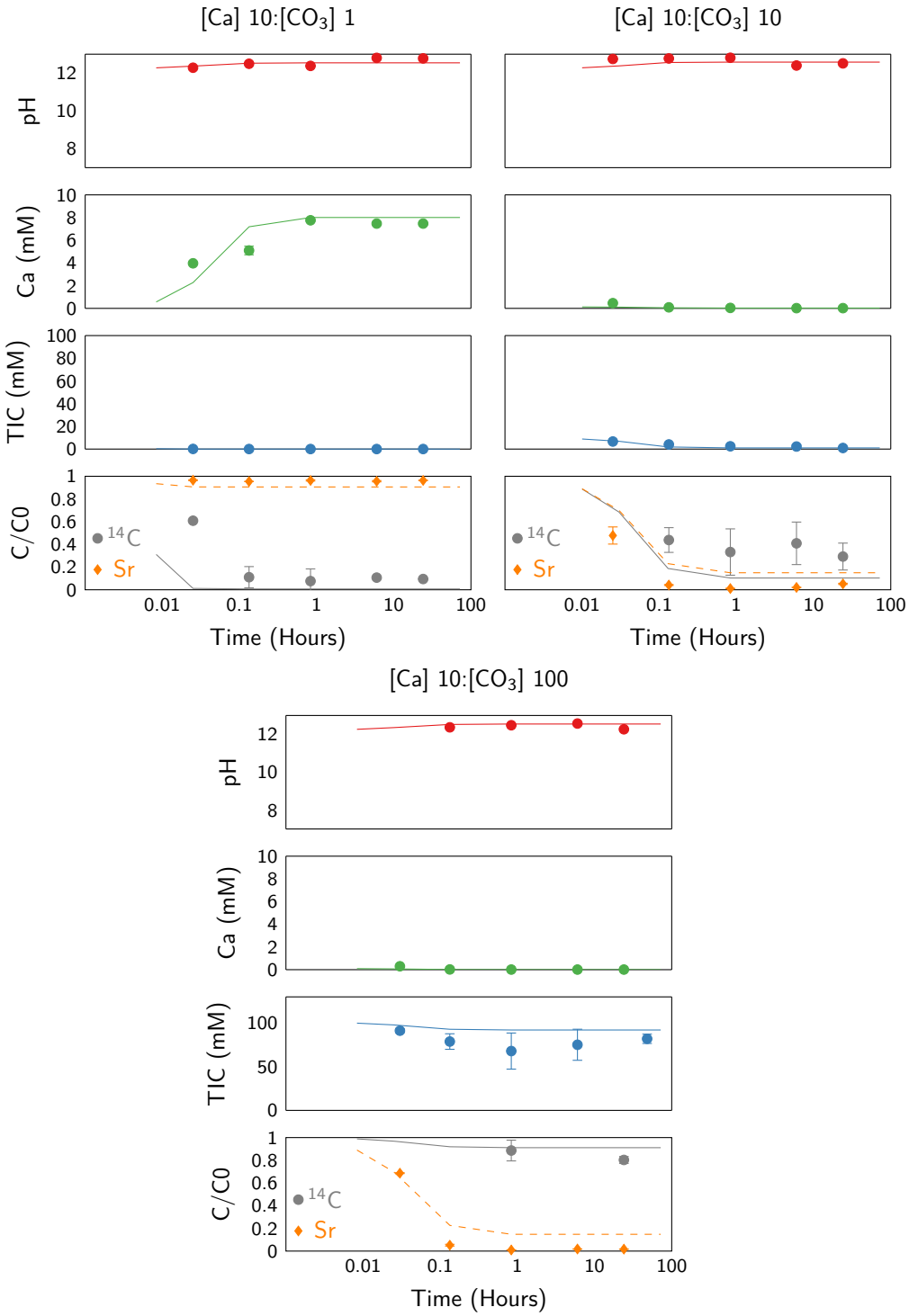

Figure 4.3: Data from the closed system experiment series potted alongside model data computed in PHREEQC

cium carbonate precipitation. Once the solid $Ca(OH)_2$ was exhausted, all the open experiments displayed a trend of decreasing aqueous Ca^{2+} concentration with time. This was due to the precipitation of calcium carbonate, which is supported by both the SEM images and the XRD analysis of the [Ca]10:[CO_3^{2-}]1 system. Where there was stoichiometric excess of CO_3^{2-} in the initial solution the removal of Ca^{2+} was rapid, because Ca^{2+} from the dissolving $Ca(OH)_2$ was able to react immediately with CO_3^{2-} in the initial solution. These systems displayed a rate of calcium carbonate precipitation that was controlled by the rate of $Ca(OH)_2$ dissolution. In the [Ca]10:[CO_3^{2-}]1 and [Ca]10:[CO_3^{2-}]5 experiments, where there was stoichiometric excess of Ca^{2+}, the aqueous Ca^{2+} concentration initially increased, and only decreased once the solid $Ca(OH_2$ was exhausted and in-gassing of atmospheric CO_2 into the alkaline solution resulted in calcium carbonate formation. In these systems the rate of calcium carbonate formation was controlled by the rate of CO_2 in-gassing once the CO_3^{2-} in the initial solution was exhausted.

The control of CO_2 in-gassing on the calcite precipitation rate is supported by the TIC trend, which displays depletion to minimum values within 8 min in experiments with initial stoichiometric excess of Ca^{2+}. This depletion was followed by an interval where TIC was maintained at low concentrations, indicating any TIC in-gassing was being rapidly used by carbonate precipitation. Experiments with initial stoichiometric excess of CO_3^{2-} also show an initial depletion of TIC. However this depletion was immediately followed by an increase in TIC (observed at the end of all experiments) caused by in-gassing of CO_2 in the absence of carbonate precipitation.

The initial morphology of solids recovered from the sacrificial [Ca]10:[CO_3]1 experi-

ments was similar to that observed by Jung et al. (2000) under excess Ca conditions. It was suggested that the elongate shaped calcite results from excess Ca adsorption at the growth surface of the rhombohedral {104} faces which slows their growth. After 50 min a transition from elongate to isotropic calcite occurred which continued until the end of the experiment at 198 h. The cause of this transition is unclear as it initiated around the peak aqueous Ca^{2+} concentration when aqueous CO_3^{2-} was negligible (an interval during which the elongate form should be strongly favoured).

4.4.2 Modelling

Kinetic modelling was carried out using PHREEQC version 3 (Parkhurst and Appelo, 2013) and the Hatches database (Cross and Ewart, 1991) to better explain the key trends observed in the data (the full input text is available in Appendix A. Review of the data suggests the variation in the bulk chemistry of the reaction with time depends on the kinetics of at least three processes: the rate of $Ca(OH)_2$ dissolution, the rate of calcite precipitation, and the rate of CO_2 in-gassing.

$Ca(OH)_2$ dissolution

Calcium hydroxide dissolution was modelled using the rate equation (Eq. 4.5) (Johannsen and Rademacher, 1999).

$$R_{Port} = k_r \times S_p \times (K_{sp} - a\{Ca^{2+}\} \times a\{OH^-\}^2) \tag{4.5}$$

Where S_p is the surface area of the dissolving $Ca(OH)_{2(S)}$ and $a\{X\}$ is the aqueous

activity of X (calculated in PHREEQC from aqueous concentration using the Debye-Hückel formula (Parkhurst and Appelo, 1999)). Implicitly equation (Eq. 4.5) assumes that the rate limiting step controlling the rate of the reverse reaction is a tri-molecular elementary reaction. The forward and reverse constants suggested by Johannsen and Rademacher are $k_f = 1 \times 10^{-5}$ mol L^{-1} s^{-1} m^{-1} and k_r=2.1 L^2 mol^{-2} s^{-1} m^{-2} at 20°C Johannsen and Rademacher (1999). The ratio of the forward and reverse rate constants imply a solubility product for calcium hydroxide dissolution of $4.8 \times 10{-}6$. This value is fractionally lower than the commonly used value of K_{sp}=5.5×10^{-6}, (Lide, 2001) but the difference is probably associated with the sensitivity of the reverse reaction to the amount of solid present (Johannsen and Rademacher, 1999).

The surface area of the $Ca(OH)_2$ starting material was calculated from triplicate BET analyses using a Micromeritics Gemini VII 2390a instrument. A sample size of 0.479 g was used and dried overnight at a temperature of 105°C while being flushed with nitrogen gas. The sample was then re-weighed to account for any moisture loss. A dead-space volume measurement was taken using helium which was then removed via vacuum and triplicate measurements were taken, using nitrogen as an absorbent at -196°C. Results are presented in Table 4.1. A specific surface area of 4.18 m^2 g^{-1} was obtained. In order to account for decreasing particle size during the dissolution the initial surface area was multiplied by the ratio of current moles to initial moles of $Ca(OH)_{2(s)}$. The initial amount of $Ca(OH)_2$ added to the system was assumed to be 9.2 mmol (rather than 10 mmol) to account for the 8% $\pm$ 3% calcite impurities observed in the $Ca(OH)_2$ stock, identified by XRD and quantified by Rietveld analysis.

The output from this model was compared to XRD data obtained for the percentage

Table 4.1: BET analysis of the Ca(OH)2 starting material

	BET surface area (m^2 g^{-1})	BET constant (C)	r^2
a	4.2236±0.043	274.1	0.9996
b	4.1449±0.041	211.9	0.9996
c	4.1594±0.043	254.2	0.9996
Average	4.176±0.068	246.73	0.9996

calcite in the solid phase, converted to [Ca] by multiplying the percentage by the expected final concentration and dividing by 100. As well as conductivity data obtained from dissolving 10 mmol of $Ca(OH)_2$ in 100ml of 0.01M NaOH. The conductivity data was converted to % dissolved by dividing by the stable conductivity achieved after 30 minutes and multiplying by 100. This was then converted to [Ca] by multiplying by the expected final concentration/100.

Estimating the surface area of $Ca(OH)_{2(S)}$ from its mass would slightly underestimate the rate of dissolution if the $Ca(OH)_{2(S)}$ consisted of uniform equidimensional particles, as volume would decrease with the nominal particle size more quickly than would the surface area. However if the $Ca(OH)_{2(S)}$ assemblage contained a range of particle sizes, then the complete dissolution of fine crystals on short time scales would result in a decrease in the overall dissolution rate over longer time periods. Separate $Ca(OH)_2$ dissolution experiments were conducted to investigate the rate of $Ca(OH)_{2(S)}$ dissolution under the conditions used in this study (Figure 4.4). These show that the rate equation assumed in the model underestimates the rate of dissolution over the first 2 min, and then overestimates the rate slightly; however, the Johannsen and Rademacher rate equation provides a good approximation to the observed data.

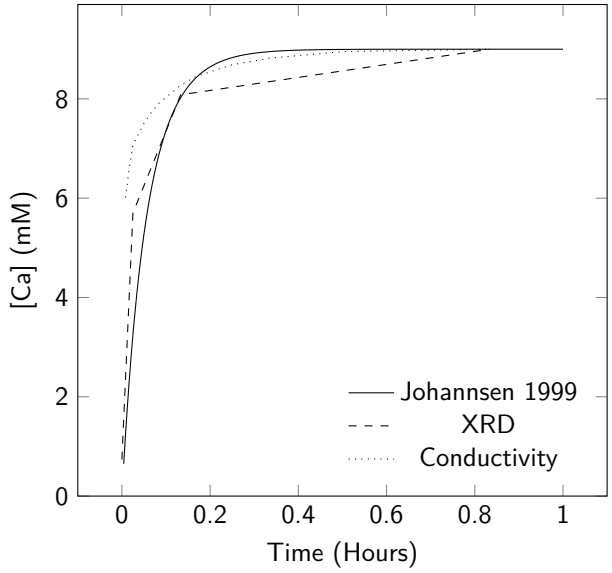

Figure 4.4: Comparison of published $Ca(OH)_2$ dissolution rate to experimental data. XRD data obtained through Rietveld refinement on powders generated during the experimental series, and conductivity data obtained during separate triplicate experiments.

Calcite kinetics

The Nancollas and Reddy model (Nancollas and Reddy, 1971) was used to predict calcium carbonate precipitation rates. This model was selected as it is based on the direct reaction of Ca^{2+} ions with CO_3^{2-} ions to form $CaCO_3$ (Eq. 6), which is believed to be the main reaction pathway at pH>9 (Inskeep and Bloom, 1985).

$$R_{Cal} = k_f \times S_c \times (a\{Ca^{2+}\} \times a\{CO_3^{2-}\} - K_{sp}) \tag{4.6}$$

Where k_f is the second order rate constant for calcite precipitation (k_f=118 dm^6 mol^{-1} m^{-2} s^{-1}, (Inskeep and Bloom, 1985)), K_{sp} is the solubility product constant for calcite ($K_{sp} = 10^{-8.44}$ (Lide, 2001)), and S_c is the calcite surface area available for reaction.

The surface area of neo-formed calcite could not be estimated from BET analysis due to low precipitate yields as well as the presence of Ca(OH)2 alongside the early formed

precipitate. Surface areas were instead calculated from the average crystal dimensions from SEM images using an assumed calcite density of 2.7 g cm^{-3} and assuming a cubic shape for rhombic crystals and a cylindrical shape for prismatic crystals.The rhombic crystals yielded a surface area of 5.37 m^2 g^{-1} while the prismatic crystals displayed a significantly larger surface area of 76.19 m^2 g^{-1}. If it assumed that by the end of testing 10 mmol of Ca forms $CaCO_3$ (formula weight 100 g mol^{-1}) then the rhombic end-point population would have an expected surface area of:

$$SA = 5.37 \times (0.01 \times 100) = 5.37\ m^2\ L^{-1} \tag{4.7}$$

The initial rhombic calcite has a larger specific surface area but smaller mass so the overall surface area is minimal (the initial concentration of seed crystals in the $Ca(OH)_2$ was calculated at 8.16% of the 1 mmol $Ca(OH)_2$):

$$SA = 76.19 \times (0.01 \times 100) = 6.2\ m^2\ L^{-1} \tag{4.8}$$

Due to uncertainties in the mass of $CaCO_3$ precipitated at early time points a value of 5.4 m^2 g^{-1} was used, which reflects the maximum surface area associated with the rhombic endpoint (based on the conversion of 10 mM of $Ca(OH)_2$ to $CaCO_3$). The estimated surface area value used is consistent with those observed in the literature (Table 4.2).

Table 4.2: Surface area and crystal sizes taken from literature values and SEM images

	Crystal Length (μm)	Surface area ($m^2\ g^{-1}$)	Morphology
Inskeep and Bloom (1985)	4-20	0.7	Rhombic
Schultz et al. (2013)	<0.5	14–17	Nano–Rhombic
Nancollas and Reddy (1971)	10	0.3	Prismatic
Huang et al. (1991)	0.7	8.63	Prismatic
This Study	0.41	5.2	Rhombic
This Study	0.5	76	Prismatic

CO_2

The chemical equation for the uptake of $CO_{2(aq)}$ into an aqueous solution are shown in Eq. 4.2a–4.2c (Clark et al., 1992). Deprotonation reactions such as Eq. 4.2c are rapid in aqueous solution, therefore in systems not limited by mixing, the rate at which atmospheric CO−2 enters solution will be controlled either by dissolution (Eq. 4.2a) or hydroxylation (Eq. 4.2b).

Noyes et al. (Noyes et al., 1996) suggest that the dissolution of CO_2 into an aqueous solution can be explained by contact between a gas phase and a homogenous solution when the reaction vessel was stirred vigorously enough to prevent a saturated surface layer forming. They report that gas dissolution flux of CO_2 per unit interface area (mol $cm^{-2}\ s^{-1}$) was:

$$J_{CO2} = k_{tr} \times ([CO_{2(aq)}^{equilibrium}] - [CO_{2(aq)}]) \tag{4.9}$$

Where K_{tr} is the exchange coefficient $k_{tr} = 5.4 \times 10^{-4}$ cm s^{-1}, $[CO_{2(aq)}]$ is the aqueous concentration of CO_2 and $[CO_{2(aq)}]$equilibrium is the aqueous CO_2 concentration at equilibrium, calculated by Henry's law (Eq. 8) (Atkins and De Paula, 2006):

$$[CO_{2(aq)}^{equilibrium}] = K_H \times P_{CO2} \tag{4.10}$$

Where P_{CO2} is the partial pressure of CO_2 in the atmosphere ($P_{CO2} = 4 \times 10^{-4}$) and K_H is the Henry's law constant ($K_H = 0.034$ mol L^{-1} atm^{-1} for the dissolution of CO_2 in water (Sander, 2015)). Thus $[CO_{2(aq)}]$equilibrium is 1.36×10^{-5} mol L^{-1}. The maximum rate of CO_2 dissolution will occur when $[CO_{2(aq)}]$=0 and is equal to 7.34 $\times$ 10^{-9} mol cm^{-2} s^{-1}. If the solution surface area in a 100ml flask is 56 cm^2 (10.5 cm diameter) the CO_2 dissolution rate will be 1.48 mmol hr^{-1}.

The subsequent hydroxylation of this $CO_{2(aq)}$ by hydroxyl ions will have a forward reaction rate of the form:

$$R_{hyd} = k_{hyd} \times [CO_2(aq)] \times [OH^-] \tag{4.11}$$

Where the rate constant $k_{hyd} = 5900$ L mol^{-1} s^{-1}, (Pinsent et al., 1956). The theoretical maximum hydroxylation rate occurs when there is equilibrium between atmospheric and dissolved CO_2. At pH 12.3 ($[OH^-]$ 0.02 mol L^{-1}) this rate is equal to 5777 mmol L^{-1} hr^{-1}. Thus in a 100 mL solution at pH 12.3 the theoretical maximum hydroxylation rate of CO_2 is 578 mmol hr^{-1}. This suggests that in a highly alkaline system, that is initially very under-saturated with respect to carbonate species, the CO_2 dissolution rate will control the carbonate flux.

Figure 4.5L shows the variation in $Ca_{(aq)}^{2+}$ in the [Ca]10:[CO_3]1 test for the time period between 50min and 6 h. This system has a stoichiometric excess of Ca^{2+}, and during this time period, after the calcium hydroxide had dissolved but while the pH>12, it

is believed that the aqueous calcium concentration is controlled by the CO_2 flux to solution. If this assumption is correct, the experimental observed flux of CO_2 into solution is constant during this time period, and equivalent to 0.25 mmol hr^{-1} into 100 mL of solution.

Figure 4.5R shows the increase in TIC in the [Ca]10:[CO_3]10 test for the time period between 50 min and 72 h. This system was initially in stoichiometric balance, but the data are for the time once Ca^{2+} had been removed from solution, and while the pH>12. During this period it is believed that the dissolved TIC concentration is controlled by the CO_2 flux to solution. If this assumption is correct, the experimental observed flux of CO_2 into solution is constant during this time period, and equivalent to 0.22 mmol hr^{-1} into 100 mL of solution. This is very similar to the CO^2 flux observed in the [Ca]10:[CO_3]1 test, and both about one sixth of the theoretical maximum dissolution flux of 1.48 mmol hr^{-1} calculated from (Eq. 4.10).

The maximum $CO_{2(g)}$ dissolution rate predicted by (Eq. 4.10) is equivalent to consuming the total amount of CO_2 in the headspace of a 500 mL conical flask (500 mL) in 40s. The neck of the conical flasks were "stoppered" with foam bungs designed to stop contamination with atmospheric dust, but allow gas exchange with atmosphere by diffusion. It is probable that diffusion through the foam bung was unable to match the maximum rate of CO_2 dissolution, and the partial pressure CO_2 within the head-space of the flask was below its atmospheric value. An atmospheric P_{CO2} of 6.75×10^{-5} ($1/6^{th}$ atmospheric) yields a forward rate consistent with the experimental data.

The experimental rate begins to deviate from 0.25 mmol hr^{-1} as TIC accumulates in solution. As TIC accumulates the [$CO_{2(aq)}$] will increase and the reverse term in

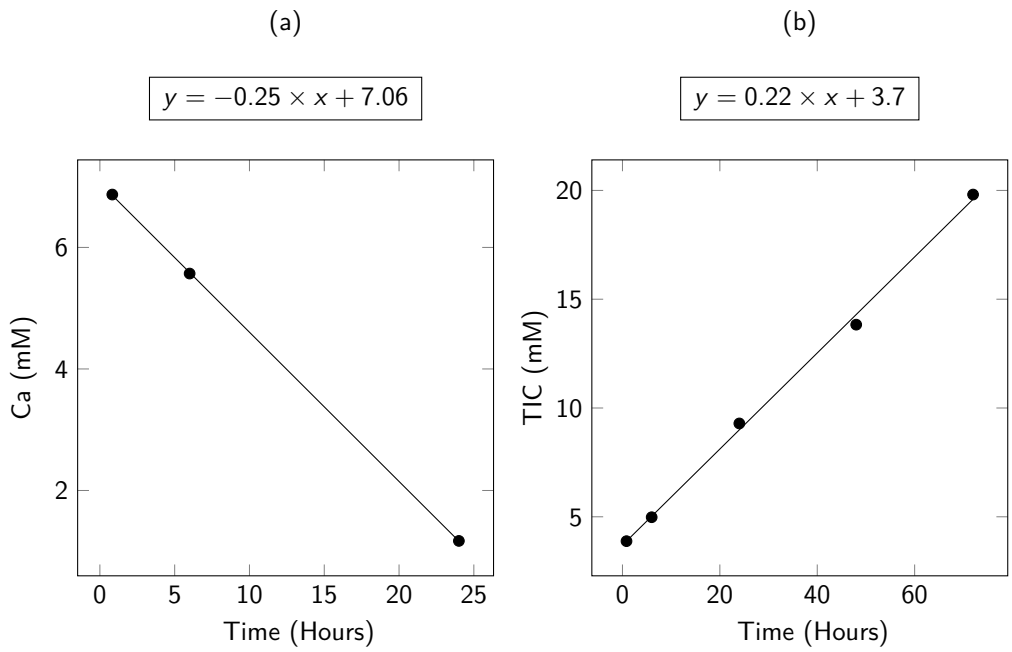

Figure 4.5: Excerpt from the [Ca]10:[CO_3]1 Ca plot between 50 m - 6 h R) Excerpt from the [Ca]10:[CO_3]10 TIC plot displaying a linear trend between 50 m - 72 h

equation (Eq. 4.9) becomes important. Without this reverse term the in-gassing would proceed unrestricted and predict a lower than observed final pH (4.6). PHREEQC distributes $CO_{2(aq)}$ into the H_2CO_3 "pool" therefore the [H_2CO_3] was used in the model in place of [$CO_{2(aq)}$]. This reverse rate will therefore be an overestimation of the out-gassing, however due to the low concentrations of H_2CO_3 and $CO_{2(aq)}$ at high pH this effect will be minimal. Figure 4.6 shows that the models including and excluding this reverse term are able to bracket the observed data.

Contaminant removal

Carbon-14 removal was modelled assuming its removal would be proportional to that of initial TIC, and that isotopic affects are minimal. The ^{14}C C/C_0 modelling shown in figure 4.1 is terminated at the point of maximum ^{14}C removal (after the initial TIC

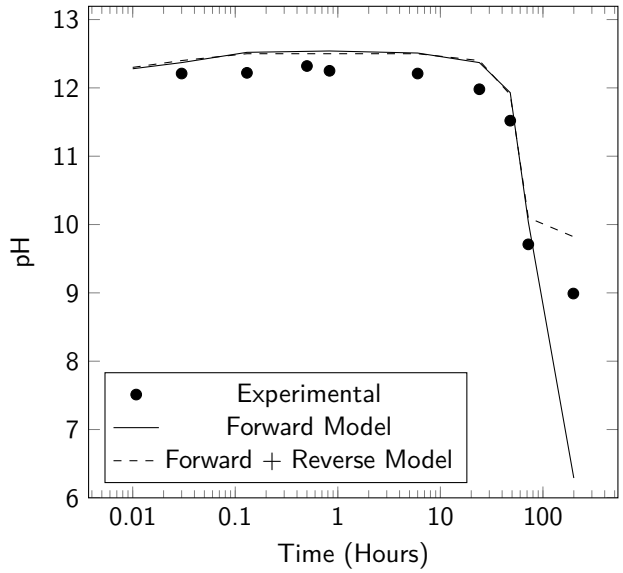

Figure 4.6: Experimental CO_2 data from the [Ca]10:[CO_3]1 experiment plotted against 3 model curves

Table 4.3: Average strontium distribution coefficients for each triplicate series

Experiment	Ca_{ppt}	Ca_{sol}	Sr_{ppt}	Sr_{sol}	D_{Sr}
10_ 1	9.980	0.020	0.011	4.15×10^{-4}	0.0508
10_ 5	9.984	0.016	0.011	5.93×10^{-4}	0.0287
10_ 10	9.912	0.034	0.011	3.28×10^{-4}	0.1120
10_ 100	9.988	0.012	0.011	2.25×10^{-4}	0.0606
Average	9.966	0.020	0.011	3.90×10^{-4}	0.0566

is depleted) as CO_2 in-gassing affects this trend. This was the case for all systems apart from the [Ca]10:[CO_3]1 experiment which showed significantly more rapid ^{14}C depletion than TIC. This could be due to errors in the TIC measurements (near to the limit of detection), which become less significant at higher concentrations.

Sr removal was modelled assuming that (Sr,Ca)CO_3 is an ideal solid solution with a distribution coefficient of 0.057. This value was chosen as an average of experimental values (table 4.3) and concurs with literature values (Curti, 1997).

$$D_{Sr} = \frac{[Sr]/[Ca]_{ppt}}{[Sr]/[Ca]_{sol}} \tag{4.12}$$

4.4.3 Discussion

Carbon-14 uptake was controlled by the depletion of TIC from the solution. This was achieved most effectively where there was a stoichiometric excess of Ca^{2+} in solution. However, a recrystallization process which started after about 50min caused a remobilization of ^{14}C to the solution. This remobilization indicates that the recrystallization involved a significant amount of dissolution which returned the lattice material to the solution, where the ^{14}C was diluted by $^{12}CO_2$ from in-gassing. Between 50 min and 24 h the remobilization observed in the [Ca]10:[CO_3]1 experiment was limited and ^{14}C removal remains >89%. In this case the remobilization was limited because the $^{14}CO_3^{2-}$ was released into a solution with high Ca and low TIC and therefore was re-precipitated. After 24 h TIC began to accumulate in solution and so $^{14}CO_3^{2-}$ released by recrystallization also accumulated in solution. This suggests that if a net negative flux of TIC was maintained during the recrystallization ^{14}C would not accumulate in the solution.

In the closed system experiments the lack of CO_2 in-gassing ensured minimal TIC in solution to dilute any ^{14}C remobilized. However, this lack of CO_2 appears to have resulted in a lower ^{14}C removal across all experiments, likely due to the lower overall volume of calcite precipitated.

Sr was removed in exceedance of 97% under all experimental conditions (the maximum observed removal was 98.6% in the [Ca]10:[CO_3^{2-}]1 experiment). Sr removal occurred within the first 8min in experiments with a stoichiometric excess of TIC, this Sr removal was associated with a depletion of Ca. Experiments with stoichiometric excess of Ca displayed a lag before the removal of Sr. Between 6-24 h 4.4 mmol of Ca (47%) was

precipitated, accompanied by 0.78 ppm of Sr (7.8%). During the following interval (24-48 h) 1.2 mmol of Ca was precipitated (13%), accompanied by 8.4 ppm of Sr (84%). This suggests that an incorporation mechanism was operating between 24-48 hours that was not occurring during the preceding interval.

A possible mechanism that explains the observed changes in Sr uptake involves the mode of Sr adsorption to the calcite surface. As Sr^{2+} concentration increases relative to Ca^{2+}, Sr incorporation may proceed via a strontianite like precursor rather than simple substitution for Ca in calcite (Parkman et al., 1998), producing a higher overall Sr uptake to solids (as observed in the later stages our experiments). Further work would be required to prove this mechanism, however the results are consistent with a more effective incorporation route following the depletion of solution Ca; potentially indicating the concentration of Sr relative to Ca may play a role in the effective removal of Sr. The [Ca]10:[CO_3]5 experiment showed composite behaviour of the two series. Initially Sr was removed rapidly due to low concentration of Ca in solution simultaneous with dissolution of $Ca(OH)_2$ and precipitation of $CaCO_3$. Following this initial depletion there was a period during which Sr concentration remained stable ($\pm$0.1ppm). This is due to the accumulation of Ca in solution following the dissolution of Ca(OH)2 into a TIC depleted solution.

A similar strontium removal from solution was achieved in all systems. It is possible that Sr was also remobilized during calcite recrystallization in the [Ca]10:[CO_3]1 experiment, however, in contrast to the situation with ^{14}C, there is no additional source of M^{2+} cations in the solution and as such Sr was immediately re-precipitated and did not accumulate in solution.

The Sr and Ca concentration at the final time-points in all experiments were higher than the concentrations at the penultimate time points. This is a function of decreasing solution pH, which will have caused the dissolution of calcite. In the experiments where there was an initial stoichiometric excess of Ca^{2+} there is a loss of ^{14}C from solution in the final stages of experiments. These experiments reached a final pH<9.3, and so this loss is attributed to isotopic exchange of aqueous ^{14}C with atmospheric $^{12}CO_2$ (this has be found to be a significant process in solutions with pH$\leq$9.324).

4.4.4 Implications for groundwater treatment

A representative composition for groundwater in the Sellafield Separation Area is reported in (table 4.4) Graham (2013). Dosing such groundwater with calcium hydroxide to produce a solution with a pH>12 and a stoichiometric excess of Ca^{2+} over CO_3^{2-} (i.e. conditions similar to those in the [Ca]10:[CO_3^{2-}]1 experiment) is a promising method for removing ^{14}C-carbonates and ^{90}Sr. This would be most effective if it were operated as a two stage treatment scheme. The first stage would comprise of adding $Ca(OH)_2$ in a closed system to remove TIC, and thus the ^{14}C, from solution. After separation of the precipitate, the aqueous effluent would then be sparged with air to promote CO_2 in-gassing and induce further carbonate precipitation, which would co-precipitate the ^{90}Sr.

Only $Ca(OH)_2$ will need to be added to run the proposed treatment scheme. TIC content in the groundwater is sufficient such that the addition of 840.3 g of $Ca(OH)_2$ per m_3 would achieve a 10:1 Ca:CO_3 molar ratio and yield an approximate pH of 11.6 which would be sufficient to minimise de-gassing of ^{14}C. Costing information for this reagent

Table 4.4: Concentration of selected Sellafield groundwater ions and the range of reported ^{14}C and ^{90}Sr activities.Graham (2013)

GW species	Concentration
pH	7
Ca	0.96 mM
HCO_3	1.23 mM
Mg	0.19 mM
K	0.18 mM
Na	1.12 mM
Cl	1.40 mM
SO4	0.21 mM
Sr	1.40 μM
^{14}C	1-50 KBq L^{-1}
^{90}Sr	0.1-44 KBq L^{-1}

Table 4.5: Costing information for the proposed treatment scheme. Prices quoted from Singleton Birch 01652 686000 (19/11/2015)

Reagent	$Ca(OH)_2$
Amount require per m^3	840.3 g
Cost per ton of reagent	$260
Cost per m^3 of groundwater	$0.22

is provided in Table 4.5.

Mass balance calculations using the maximum removal efficiencies observed in our experiments suggest that a m^3 of the most contaminated groundwater present at Sellafield would precipitate 287 grams of calcite during the ^{14}C removal phase, which would contain 49.85 MBq of ^{14}C. The ^{90}Sr removal phase would yield a further 943 grams of calcite which would contain 43.38 MBq of ^{90}Sr. This would constitute a material with a total β activity of 75 GBq/ton (>6$\times$ the upper limit for Low Level Waste (Laker et al., 2010)); however, treatment of lower activity groundwater, would in practice produce materials with much lower activities.

This process would also produce discharge water containing 0.15 KBq L^{-1} of ^{14}C and 0.62 KBq L^{-1} of ^{90}Sr. This effluent could be further treated by Ion Exchange media

(having reduced the competing ions Ca and Mg during the calcite precipitation process) or simply discharged, depending on acceptable discharge limits. Finally, it is noted that the proposed two-stage treatment scheme would create separate waste products for ^{14}C and ^{90}Sr and does not result in an increase in liquid volume. It would also produce an effluent stream buffered to pH<9 (which is typically a desired pH limit for effluent discharges to surface waters (Mayes et al., 2009)). Therefore, this treatment shows significant potential as a working remediation technique but further work is still required to understand how this treatment scheme would function in site specific groundwater regimes. For example it is not known how the presence of Mg^{2+} and SO_4^{2-} in groundwater would affect the treatment (as these groundwater ions can affect the morphology and allotropes of carbonate precipitates (Bots et al., 2011)), or how the treatment efficiencies would scale to a smaller Sr^{2+} concentrations (i.e. 1.4 μM vs 114 μM). The overall cost effectiveness of this treatment will also be affected by in-situ rates of contaminant desorption/dissolution from solids, which may result in the need for continued groundwater removal and treatment over long time periods.

Conclusion

The precipitation of calcium carbonate has been shown to be a viable mechanism for the removal of ^{14}C and Sr from a solution. Overall, the maximum achieved removal of ^{14}C and Sr was 99.7% and 98.6% respectively. However, the chemical and morphological data suggest that the crystallization pathways involved in precipitation can have a significant impact on the removal of ^{14}C from a solution. If re-crystallization occurs it returns the lattice material to the solution, where it mixes with atmospheric CO_2. This

mixing allows dilution of ^{14}C by ^{12}C which results in a lower incorporation of ^{14}C into the re-precipitated calcite. If a treatment system based on calcium hydroxide dosing were applied to the most contaminated groundwater present at the UK Sellafield site, these removals would produce just over 1 kg solid residue (containing 100 MBq total beta activity) per m^3 treated and produce an effluent with a pH$\leq$9, containing 0.15 KBq L^{-1} of ^{14}C and 0.62 KBq L^{-1} of Sr after a single application.

Supporting information

This includes additional experimental and XRD data, groundwater compositions, Sr distribution coefficients and reagent costings. Further details of our kinetic model development are also provided along with the full PHREEQC input script. This material is available in Appendix B.

Bibliography

Achal, V., Pan, X., Zhang, D. (2012). Bioremediation of strontium (Sr) contaminated aquifer quartz sand based on carbonate precipitation induced by Sr resistant Halomonas sp. *Chemosphere*, **89**(6), pp. 764–8.

Amiro, B., Ewing, L. (1992). Physiological conditions and uptake of inorganic carbon-14 by plant roots. *Environmental and Experimental Botany*, **32**(3), pp. 203–211.

Aquilonius, K., Hallberg, B. (2005). Process-oriented dose assessment model for 14C due to releases during normal operation of a nuclear power plant. *Journal of environmental radioactivity*, **82**(3), pp. 267–83.

Atkins, P., De Paula, J. (2006). Atkins' physical chemistry. *New York: WH Freman*.

Barton, C.S., Stewart, D.I., Morris, K., Bryant, D.E. (2004). Performance of three resin-based materials for treating uranium-contaminated groundwater within a PRB. *Journal of hazardous materials*, **116**(3), pp. 191–204.

Bots, P., Benning, L.G., Rickaby, R.E.M., Shaw, S. (2011). The role of SO4 in the switch from calcite to aragonite seas. *Geology*, **39**(4), pp. 331–334.

Boylan, A.A., Stewart, D.I., Graham, J.T., Trivedi, D., Burke, I.T. (2016). Mechanisms of inorganic carbon-14 attenuation in contaminated groundwater: Effect of solution pH on isotopic exchange and carbonate precipitation reactions. *Applied Geochemistry*, pp. 1–11.
URL: *http://dx.doi.org/10.1016/j.apgeochem.2016.12.006*

Clark, I.D., Fontes, J.C., Fritz, P. (1992). Stable isotope disequilibria in travertine from high pH waters: Laboratory investigations and field observations from Oman. *Geochimica et Cosmochimica Acta*, **56**(5), pp. 2041–2050.

Cross, J.E., Ewart, F.T. (1991). HATCHES—a thermodynamic database and management system. *Radiochimca Acta*, **52**(2), pp. 421–422.

Curti, E. (1997). *Coprecipitation of radionuclides: basic concepts, literature review and first applications*. Paul Scherrer Institut.

Dias, C.M., Stenström, K., Bacelar Leão, I.L., Santos, R.V., Nícoli, I.G., Skog, G., Ekström, P., da Silveira Corrêa, R. (2009). 14CO2 dispersion around two PWR nuclear power plants in Brazil. *Journal of environmental radioactivity*, **100**(7), pp. 574–80.

Fernández-Díaz, L., Fernández-González, Á., Prieto, M. (2010). The role of sulfate groups in controlling CaCO3 polymorphism. *Geochimica et Cosmochimica Acta*, **74**(21), pp. 6064–6076.

Fujita, Y., Ferris, F.G., Lawson, R.D., Colwell, F.S., Smith, R.W. (2000). Calcium carbonate precipitation by ureolytic subsurface bacteria. *Geomicrobiology Journal*, **17**(4), pp. 305–318.

Gebauer, D., Volkel, A., Colfen, H. (2008). Stable Prenucleation Calcium Carbonate Clusters. *Science*, **322**(5909), pp. 1819–1822.
URL: *http://www.sciencemag.org/cgi/doi/10.1126/science.1164271*

Graham, J. (2013). ERT Trial Groundwater Analysis – Rounds 16 – 19. NNL Technical Memorandum LP06489/06/10/07. Technical report, NNL.

Gray, J., Jones, S.R., Smith, A.D. (1995). Discharges to the environment from the Sellafield site, 1951-1992. *Journal of Radiological Protection*, **15**(2), pp. 99–131.

Hall, O.J., Aller, R.C. (1992). Rapid, small-volume, flow injection analysis for ΣCO2 and NH4+ in marine and fresh waters. *Limmology and Oceanography*, **37**(5), pp. 1113–1119.

Holland, H.D., Holland, H.J., Munoz, J.L. (1964). The coprecipitation of cations with CaCO3—II. The coprecipitation of Sr+2 with calcite between 90° and 100°C. *Geochimica et Cosmochimica Acta*, **28**(8), pp. 1287–1301.

Huang, Y.C., Fowkes, F.M., Lloyd, T.B., Sanders, N.D. (1991). Adsorption of calcium ions from calcium chloride solutions onto calcium carbonate particles. *Langmuir*, **7**(8), pp. 1742–1748.

Inskeep, W.P., Bloom, P.R. (1985). An evaluation of rate equations for calcite precipitation kinetics at pCO2 less than 0.01 atm and pH greater than 8. *Geochimica et Cosmochimica Acta*, **49**(10), pp. 2165–2180.

Johannsen, K., Rademacher, S. (1999). Modelling the Kinetics of Calcium Hydroxide Dissolution in Water. *Acta hydrochimica et hydrobiologica*, **27**(2), pp. 72–78.

Jung, W.M., Kang, S.H., Kim, W.S., Choi, C.K. (2000). Particle morphology of calcium carbonate precipitated by gas–liquid reaction in a Couette–Taylor reactor. *Chemical Engineering Science*, **55**(4), pp. 733–747.

Katz, A., Sass, E., Starinsky, A., Holland, H.D. (1972). Strontium behavior in the aragonite-calcite transformation: An experimental study at 40–98°C. *Geochimica et Cosmochimica Acta*, **36**(4), pp. 481–496.

Kersting, A.B., Efurd, D.W., Finnegan, D.L., Rokop, D.J., Smith, D.K., Thompson, J.L. (1999). Migration of plutonium in ground water at the Nevada Test Site. *Nature*, **397**(6714), pp. 56–59.

Laker, A., Ashton, C., Cummings, R. (2010). Waste Acceptance Criteria - Low Level Waste Disposal. Technical report, Low Level Waste Repository Ltd.

Lide, D.R. (2001). *CRC handbook of physics and chemistry*. CRC.

Magnusson, Å., Stenström, K., Adliene, D., Adlys, G., Dias, C., Rääf, C., Skog, G., Zakaria, M., Mattsson, S. (2007). Carbon-14 levels in the vicinity of the Lithuanian nuclear power plant Ignalina. *Nuclear Instruments and Methods in Physics Research Section B: Beam Interactions with Materials and Atoms*, **259**(1), pp. 530–535.

Marinin, D.V., Brown, G.N. (2000). Studies of sorbent/ion-exchange materials for the removal of radioactive strontium from liquid radioactive waste and high hardness groundwaters. *Waste Management*, **20**(7), pp. 545–553.

Mayes, W., Batty, L., Younger, P., Jarvis, A., Kõiv, M., Vohla, C., Mander, U. (2009). Wetland treatment at extremes of pH: A review. *Science of The Total Environment*, **407**(13), pp. 3944–3957.

Mitchell, A.C., Ferris, F.G. (2005). The coprecipitation of Sr into calcite precipitates induced by bacterial ureolysis in artificial groundwater: Temperature and kinetic dependence. *Geochimica et Cosmochimica Acta*, **69**(17), pp. 4199–4210.

Naftz, D., Morrison, S.J., Fuller, C.C., Davis, J.A. (2002). *Handbook of groundwater remediation using permeable reactive barriers: applications to radionuclides, trace metals, and nutrients*. Academic Press.

Nancollas, G.H., Reddy, M.M. (1971). The crystallization of calcium carbonate. II. Calcite growth mechanism. *Journal of Colloid and Interface Science*, **37**(4), pp. 824–830.

National-Lime-Association (). Building Construction.
URL: *https://lime.org/lime-basics/uses-of-lime/construction/building-construction/*

National-Nuclear-Laoratory (). Effluent treatment.
URL: *http://www.nnl.co.uk/inventory-management/case-studies-and-materials/using-chemical-and-process-modelling-to-design-understand-and-improve-an-effluent-treatment-plant/*

NDA (2013). 5 year Research and Development Plan. Technical report, NDA.

Nielsen, M.H., Aloni, S., De Yoreo, J.J. (2014). In situ TEM imaging of CaCO3 nucleation reveals coexistence of direct and indirect pathways. *Science*, **345**(6201), pp. 1158–1162.

Nielsen, S. (2004). The biological role of strontium. *Bone*.

Noyes, R.M., Rubin, M.B., Bowers, P.G. (1996). Transport of carbon dioxide between the gas phase and water under well-stirred conditions: Rate constants and mass accommodation coefficients. *The Journal of Physical Chemistry*, **100**(10), pp. 4167–4172.

Ostwald, W. (1897). Studien über die Bildung und Umwandlung fester Körper. 1. Abhandlung: Übersättigung und Überkaltung. *Zeitschrift für Physikalische Chemie*, **22**, pp. 289–330.

Palmisano, A., Hazen, T. (2003). Bioremediation of metals and radionuclides: What it is and how it works. Technical report, Lawrence Berkeley National Laboratory.

Panias, D., Xenidis, A., Krestou, A. (2005). *Long-term Performance of Permeable Reactive Barriers*, volume 7. Gulf Professional Publishing.

Parkhurst, B.D.L., Appelo, C.a.J. (1999). User's Guide To PHREEQC (version 2) — a Computer Program for Speciation, and Inverse Geochemical Calculations. *Exchange Organizational Behavior Teaching Journal*, **D**(Version 2), p. 326.

Parkhurst, D.L., Appelo, C.A.J. (2013). Description of input and examples for PHREEQC version 3: a computer program for speciation, batch-reaction, one-dimensional transport, and inverse geochemical calculations. Technical Report 2328-7055, US Geological Survey.

Parkman, R.H., Charnock, J.M., Livens, F.R., Vaughan, D.J. (1998). A study of the interaction of strontium ions in aqueous solution with the surfaces of calcite and kaolinite. *Geochimica et Cosmochimica Acta*, **62**(9), pp. 1481–1492.

Pingitore Jr, N.E., Lytle, F.W., Davies, B.M., Eastman, M.P., Eller, P.G., Larson, E.M. (1992). Mode of incorporation of Sr2+ in calcite: Determination by X-ray absorption spectroscopy. *Geochimica et Cosmochimica Acta*, **56**(4), pp. 1531–1538.

Pinsent, B.R.W., Pearson, L., Roughton, F. (1956). The kinetics of combination of carbon dioxide with hydroxide ions. *Transactions of the Faraday Society*, **52**, pp. 1512–1520.

Rietveld, H. (1969). A profile refinement method for nuclear and magnetic structures. *Journal of applied Crystallography*, **2**(2), pp. 65–71.

Roussel-Debet, S., Gontier, G., Siclet, F., Fournier, M. (2006). Distribution of carbon 14 in the terrestrial environment close to French nuclear power plants. *Journal of environmental radioactivity*, **87**(3), pp. 246–59.

Sander, R. (2015). Compilation of Henry's law constants (version 4.0) for water as solvent. *Atmospheric Chemistry and Physics*.

Saunders, J.A., Toran, L.E. (1995). Modeling of radionuclide and heavy metal sorption around low- and high-pH waste disposal sites at Oak Ridge, Tennessee. *Applied Geochemistry*, **10**(6), pp. 673–684.

Schultz, L.N., Andersson, M.P., Dalby, K.N., Müter, D., Okhrimenko, D.V., Fordsmand, H., Stipp, S.L.S. (2013). High surface area calcite. *Journal of Crystal Growth*, **371**, pp. 34–38.

Stamper, A., Coughlin, D., Bowes, A., Ruddick, P., Laws, F. (2014). Groundwater Monitoring at Sellafield Annual Data Review 2013. Technical Report LQRD000077, Sellafield Ltd.

Standring, W.J.F., Oughton, D.H., Salbu, B. (2002). Potential Remobilization of 137 Cs, 60 Co, 99 Tc, and 90 Sr from Contaminated Mayak Sediments in River and Estuary Environments. *Environmental Science & Technology*, **36**(11), pp. 2330–2337.

Stewart, D.I., Csõvári, M., Barton, C.S., Morris, K., Bryant, D.E. (2006). Performance of a functionalised polymer-coated silica at treating uranium contaminated groundwater from a Hungarian mine site. *Engineering Geology*, **85**(1-2), pp. 174–183.

Thompson, A., Steefel, C. (2010). Contaminant desorption during long-term leaching of hydroxide-weathered Hanford sediments. ... *science & technology*.

Tierney, K.M., Muir, G.K.P., Cook, G.T., MacKinnon, G., Howe, J.A., Heymans, J.J., Xu, S. (2016). Accumulation of Sellafield-derived radiocarbon ((14)C) in Irish Sea and West of Scotland intertidal shells and sediments. *Journal of environmental radioactivity*, **151 Pt 1**, pp. 321–7.

Zhang, Y., Dawe, R.A. (2000). Influence of Mg2+ on the kinetics of calcite precipitation and calcite crystal morphology. *Chemical Geology*, **163**(1–4), pp. 129–138.

Chapter 5

Potential amendments to the Carbonate precipitation scheme

5.1 Summary

A range of amendments to the reaction scheme presented in chapter 4 were tested in an attempt to improve the incorporation and stability of Sr and ^{14}C. These included sulphate, pH and the presence of seed crystals. Increased sulphate concentration was unable to favour aragonite precipitation and instead inhibited the removal of strontium by forming $SrSO_4$ complexes in solution which depresses the $SI_{Strontianite}$. Under high SO_4 conditions carbonate morphology displayed a clear variation with pH with vaterite favoured at low pH, aragonite at circumneutral and calcite at high pH. The presence of seed crystals was not significantly beneficial to the long term stability of the calcite although did create a more rapid removal of ^{14}C (likely due to the depressed $SI_{Calcite}$) and an enhanced removal of Sr due to the presence of a large surface area of negatively charged calcite.

5.2 Introduction

The calcium carbonate crystal system comprises of a Ca^{2+} ion bound to a CO_3^{2-} ion in a repeating pattern forming a crystal lattice. Due to the abundance of M^{2+} ions in nature the Ca^{2+} site in the carbonate lattice commonly experiences substitution of trace elements. The incorporation of trace elements into this site in carbonates has received interest from a variety of fields, including understanding the lithification of carbonate sediments (Kinsman and Holland, 1969), as a proxy for sea surface temperature in corals (Marshall and McCulloch, 2002), and more recently as a potential remediation technique for groundwater contamination (Fujita et al., 2000; Mitchell and Ferris, 2005).

Previous work has detailed the potential for a pump and treat scheme for the removal of Sr and ^{14}C from groundwater (Chapter 4). This work showed high removals for ^{14}C (99.7%) however this was subject to significant remobilization due to the recrystallization of the metastable precipitate. A slightly lower removal of ^{90}Sr was observed (98.6%) this removal was however stable.

This section will aim to test some of the published factors which have been shown to affect the coprecipitation of Sr and ^{14}C into calcium carbonate. A brief discussion of these factors will follow.

The bond lengths and angles between atoms in the carbonate lattice may vary resulting in 3 major polymorphs, Calcite, Aragonite, and Vaterite (in order of decreasing thermodynamic stability). Due the differences in atom coordination different polymorphs will favour the incorporation of different trace ions. The M^{2+} site in aragonite is coordinated by nine oxygen atoms, as opposed to six oxygen atoms in calcite. This greater

coordination number in aragonite results in larger M^{2+} lattice sites which allows larger ions, such as Sr^{2+}, to coordinate more effectively (Blanco-Gutierrez et al., 2014). This is backed up by experimental synchrotron data from Finch and Allison (2007) which suggests that Sr substitutes ideally for calcium in aragonite, causing minor lattice distribution. However, in the rhombohedral calcite structure Sr substitutes in an octahedral coordination which imparts significant strain on the lattice.

Magnesium is another ion capable of substituting into calcium sites in the carbonate lattice. As Mg^{2+} incorporates at the calcite surface it inhibits the calcite growth rate which makes the formation of this polymorph in high Mg systems less favorable. Magnesium it is not compatible in aragonite however, due to the larger lattice sites, and so does not inhibit the growth of this polymorph (Cabrera and Vermilyea, 1958; Finch and Allison, 2007). Under the high pH conditions used in this work however Mg^{2+} will precipitate out as Brucite ($Mg(OH)_2$) which makes it infeasible to study the effects of this ion on our system.

Sulphate substitution into carbonate sites within the calcium carbonate lattice is possible due to this molecule's similar ionic radius and charge to the carbonate molecule. However this molecule introduces disorder into the lattice, due to its larger ionic radius than carbonate. Due to differing lattice site geometries the degree of this disorder varies depending on the polymorph it is hosted in. Modelling of the effect of sulphate on the lattice energy of the 3 carbonate polymorphs was carried out by Fernández-Díaz et al. (2010). This showed an increase in lattice energy for both aragonite and calcite across 0-4 % SO_4^{2-} incorporation. Aragonite displayed a greater increase in lattice energy for a given % SO_4^{2-}, suggesting its incorporation into aragonite is particularly

unfavourable. Conversely vaterite displayed a decrease in lattice energy where the substitution was > 2% indicating % SO_4^{2-} incorporation would make this polymorph more stable. This modelling suggests that % SO_4^{2-} favours the precipitation of vaterite > calcite > aragonite. A series of constant composition experiments carried out by Bots et al. (2011) found that high SO_4^{2-} concentrations (>36 mM) the aragonite fraction of carbonate increased, with vaterite also present. It is therefore not entirely clear if % SO_4^{2-} will promote or inhibit the precipitation of aragonite.

The role of pH in controlling carbonate polymorphism was investigated by Tai and Chen (1998), who reported a significant correlation between the two. Their findings for a system absent of additives suggest that there exists a rapid change in the main carbonate polymorph precipitated between pH 11-12. With aragonite the major polymorph at pH 11 and calcite taking over around pH 11.7.

The recrystallization of a metastable precipitate and subsequent remobliization of ^{14}C was observed in Chapter 4. A potential mechanism to overcome this recrystallization is to use rhombic seed crystals in the initial solution to force the crystallization pathway. Seed crystals are important due to the presence of an energy barrier to be overcome during the nucleation of a crystalline phase. This energy barrier results from the energy required to form an interface in a solution. By providing an excess surface area for the precipitating phase to nucleate onto, the energy barrier is reduced and precipitation may proceed.

This section will test methods of improving the incorporation and stability of Sr and ^{14}C in carbonates precipitated from high pH solutions. Sulphate will be tested as a mechanism of favouring aragonite formation,with a range of pH values tested to

observe any thresholds. A stable rhombohedral calcite seed crystal will be tested as a mechanism for negating any recrystallization of the carbonate precipitate, utilizing a range of surface areas.

5.3 Methods

Solution set-up

Experiments were carried out as triplicate batch experiments conducted in 500 ml polypropylene conical flasks (ThermoFisher Scientific, USA). $Ca(OH)_2$ solution was prepared by dialysis filtration to form a saturated solution of 17.5 $\pm$ 2.5 mM $Ca(OH)_2$ solution. This solution was diluted 1:1 with DIW to form a solution with a Ca^{2+} concentration 8.92 $\pm$ 0.87 mM. $SrCl_2{\cdot}6H_2O$, $H^{14}CO_3$ and NaOH were added at concentrations of 10 ppm, 100 Bq ml^{-1} and 10 mM respectively, achieving a total volume of 100 ml. After which 1 mM Na_2CO_3 was added to commence the reaction, this starting solution had an initial pH of approximately 12.3. Experiments were re-ran in order ^{14}C to enable TIC measurement by FIA to take place.

Sulphate experiments

Sulphate has been reported to destabilise the aragonite lattice and, to a lesser extent, the calcite lattice, favouring the precipitation of vaterite (Fernández-Díaz et al., 2010). Bots et al. (2011) however found that high sulphate concentration (57.6 mM) caused a mixture of aragonite and vaterite to be precipitated (30% aragonite 70% vaterite). The

effect of sulphate on carbonate precipitation at high pH was tested by using varying sulphate concentrations. The base solution was amended by the addition of a Na_2SO_4 solution to achieve a concentration of 10, 25 and 50 mM. These concentrations were selected based on previous work from (Bots et al., 2011) which suggests over 50 mM SO_4 (even with a Mg:Ca=0) calcite is absent and vaterite and aragonite are the sole carbonate polymorphs. Intermediate concentrations were then selected to observe any systematic trends. Variations in carbonate morphology and polymorphs were observed with SEM and XRD analyses carried out on solid samples obtained by vacuum filtration. LSC and ICP-OES was carried out on solution samples to observe variation in ^{14}C and Sr removal and solution chemistry.

pH experiments

To further test the effect of pH on carbonate polymorphism the 50 mM sulphate experiment was repeated across a range of pH values. This was achieved by using an autotitrator set up with 0.5 mM HCl and 1 mM NaOH to maintain a constant pH of 8,9,10,11 and 12. Temperature control was achieved with a water bath situated on a stirrer plate, with a feedback device to maintain a constant temperature of 20°C. Solid samples were collected and analysed by XRD and SEM to determine carbonate morphology and polymorphism.

Seed crystal experiments

The role of seed crystals was tested by using a range of seed crystal surface areas during carbonate precipitation. Rhombohedral calcite seed crystals, purchased from Sigma

Aldrich, were first measured by BET analysis. Triplicate analysis revealed a surface area of 0.207 m^2 g^{-1} $\pm$ 0.01 m^2 g^{-1}. Masses of 0.484 g and 0.968 g were added to produce seed crystal surface areas of 1 and 2 m^2 L^{-1}. Comparison of these could then be made to the dialysis filtration experiments, which are assumed to have close to 0 m^2 L^{-1} seed. Samples were analysed by Liquid Scintillation Counting and ICP-OES to observe the variations in ^{14}C and ^{90}Sr removal, and SEM/XRD to observe the effect of the seeds on calcite morphology.

5.4 Results

5.4.1 The role of Sulphate

Data for the role of sulphate on carbonate precipitation under high pH conditions are presented in Figure 5.1. pH displayed no systematic variance across the series, all experiments displayed an initial pH of 12.26 $\pm$ 0.11 which progressed to 9.18 $\pm$ 0.19 after 196 hrs.

Calcium removal was mostly complete within the first 48 h. This removal was slightly retarded during the 10-25 mM SO_4 experiments, and further retarded in the 50 mM SO_4 experiment.

Magnesium was present at low concentrations during the first 1:30 mins of the experiment. A maximum concentration of 0.06 mM was observed in the 10 mM SO_4 experiment, this is likely from impurities in the Na_2SO_4 and $Ca(OH)_2$ and at such low concentrations is unlikely to have significantly affected precipitation.

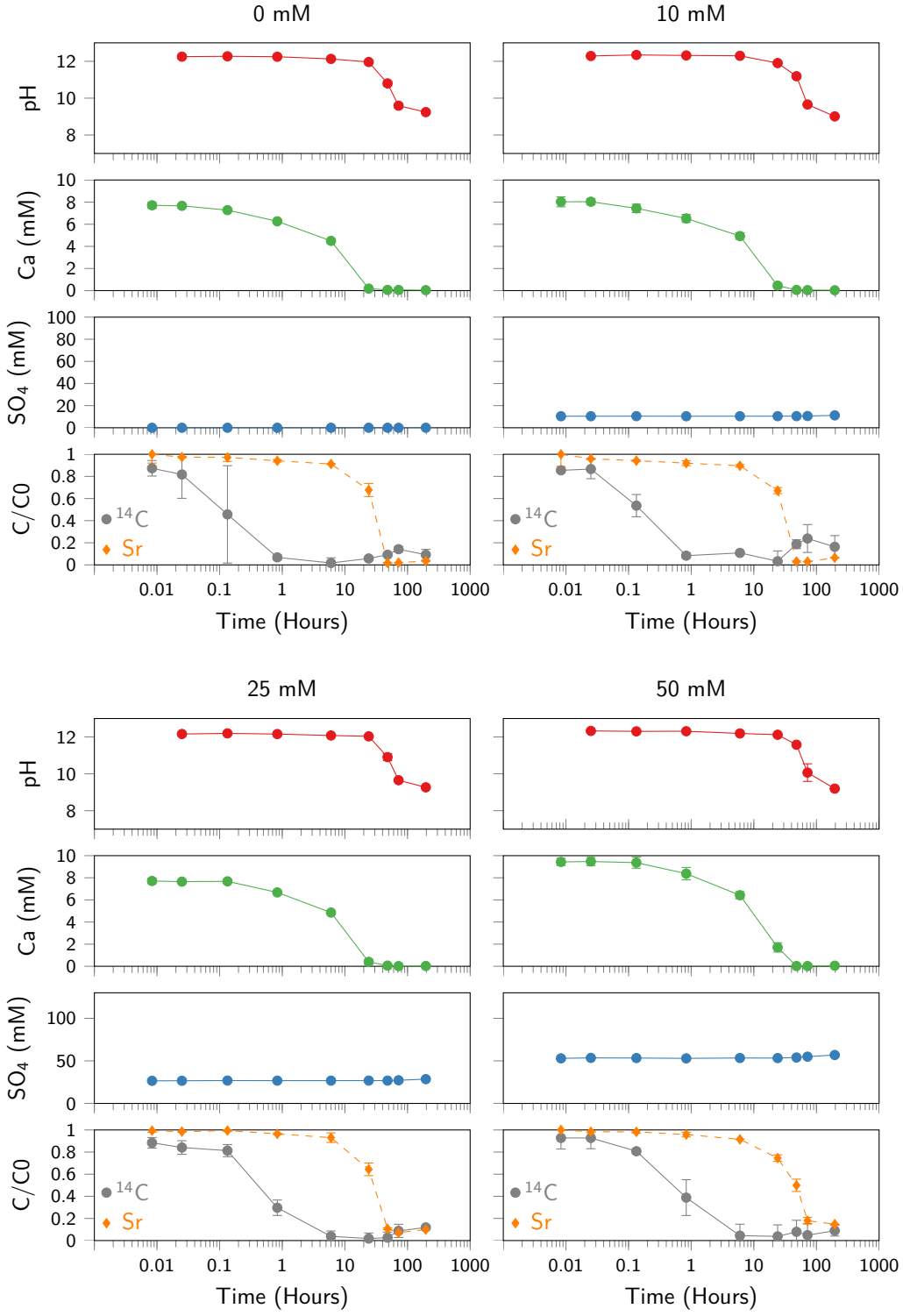

Figure 5.1: Complied data from the 0, 10, 25 and 50 mM sodium sulphate systems

The maximum removal of Sr in the varying sulphate experiments is displayed in Figure 5.2. This displays a near linear decrease in the Sr coprecipitation due to increasing concentrations of SO_4^{2-}, with a drop of 12.8 % maximum removal observed from the 0 mM SO_4^{2-} to the 50 mM SO_4^{2-} experiments.

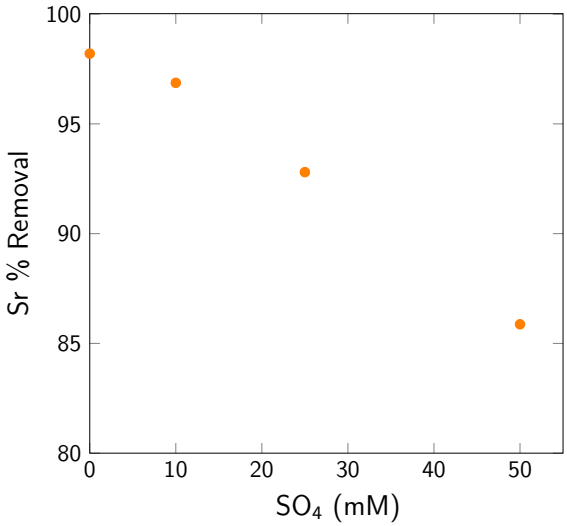

Figure 5.2: Effect of sulphate concentration on maximum removal of Sr in the 0, 10, 25 and 50 mM Na_2SO_4 experiments

XRD data taken from the batch experiment comprising 50 mM $Na_2SO_4^{2-}$ (Appendix Figure B.1) indicate that early in the experiment (8 min) Na_2SO_4 was present. After 1 h the Na_2SO_4 had dissolved and been replaced by a mixture of $CaSO_4$ and calcite. By 6 hrs calcite was present and was the only observed carbonate polymorph in all subsequent samples.

SEM images of precipitates from end member systems (0 mM and 50 mM SO_4) are presented in Appendix Figure B.6. In the sulphate free experiment precipitates presented as hemispheric crystal aggregates approximately 10.39 μm in diameter after 50 min, which grew to 27.1 μm after 72 h. The 50 mM SO_4 experiment precipitates presented as a combination of hemispheric aggregates and some "dumbbell shaped" crystals with

an average size of 6.0 μm after 50 min, these grew to 30.6 μm after 72 h. The end point morphologies from the 0 mM and 50 mM SO_4 systems were both hemispheric aggregates of rhombic crystals, with some finer more disordered material coating the surface.

Sulphate concentration had a minimal effect on the removal of ^{14}C (Table 5.1). The main effect was a slightly slower induction time which resulted in slightly less remobilization. However, this is mostly within error.

Table 5.1: Affect of Na_2SO_4 concentration on the removal of ^{14}C with 95% confidence limits

	Max ^{14}C % removal				
Na_2SO_4	I	II	III	Mean	$\pm$
0 mM	99.93	99.89	94.95	98.3	7.12
10 mM	100.01	90.08	99.95	96.7	14.2
25 mM	94.63	99.93	99.87	98.1	7.56
50 mM	99.94	99.86	88.87	96.2	15.8

5.4.2 pH effect

In the experiment that comprised 50 mM Na_2SO_4 with a constant pH (controlled by an autotitrator) that was varied from 9-12 a clear trend was observed in the carbonate polymorph formed which is presented in Figure 5.3 (raw data Appendix Figure B.4). At lower pH vaterite was the dominant morphology as predicted by (Fernández-Díaz et al., 2010) with a mixture of vaterite, aragonite and calcite at pH 11 progressing to pure calcite at pH 12.

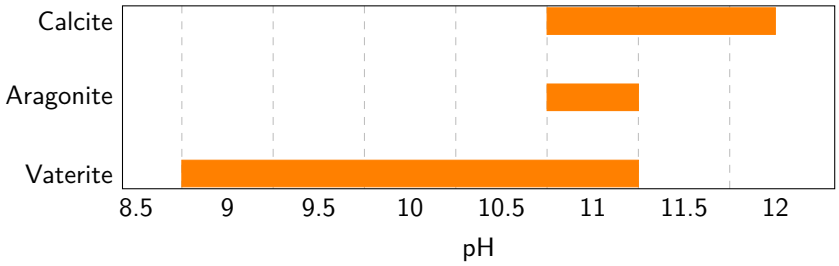

Figure 5.3: Changes in carbonate polymorphism with pH in 50 mM sulphate system

5.4.3 Seed crystal addition

The effects of seed crystals on the coprecipitation of ^{14}C and Sr into calcite is summarised in table 5.2. This indicates that as seed crystal surface area increases the removals of both ^{14}C and Sr are enhanced. With >1 m^2 L^{-1} of seed crystal surface area Sr was removed below the limits of detection of the ICP-OES (1.03×10^{-6} mM) which, correcting for dilution suggests a maximum solution concentration of 2.05×10^{-5} mM.

Table 5.2: Maximum observed removals of ^{14}C and Sr with changing calcite seed crystal surface area.

Seed crystal SA	^{14}C Removal	Sr Removal	Average ^{14}C	Average Sr
m^2 L^{-1}	%	%	%	%
0	99.92	98.20		
0	99.89	98.00	98.25	98.2
0	94.95	98.40		
1	99.93	>99.99		
1	99.92	>99.99	99.91	>99.99
1	99.89	>99.99		
2	99.89	>99.99		
2	99.95	>99.99	99.94	>99.99
2	99.98	>99.99		

The kinetics of Sr removal does not vary significantly across the range of surface areas used. ^{14}C removal however does show a systematic trend with increasing surface area

figure 5.4. The data suggest that larger calcite surface areas result in faster removal of ^{14}C from solution (>80% of the ^{14}C to be removed within the first 30 seconds). After 6 hours the ^{14}C appears to show a slight increase until 24 hours, after which a further increase was observed. The ^{14}C increase observed in the seeded experiments was greater and outside the errors in the unseeded experiments. Early time intervals (30s, 1:30 min and 8 min) for the unseeded experiment display a significant variation in their ^{14}C removal.

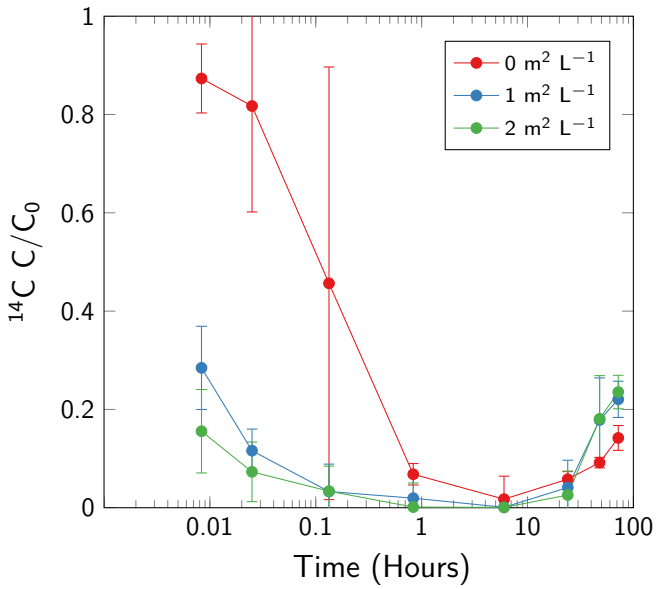

Figure 5.4: Effect of seed crystal surface area on removal of ^{14}C

SEM images from the unseeded systems are presented as the 0 mM SO_4 images on the left of Appendix figure B.6. These show that in the absence of seed crystals precipitates commonly nucleated on the surface of the reaction vessel presenting as hemispheric aggregates. Individual crystals within these aggregates appear to be rhombic in structure, by 72 h aggregates are coated in more disordered particles. SEM images from seeded experiments are presented in Appendix Figure B.8 no morphology other than the initial rhombic calcite was observed. After 24 h these calcite rhombs showed some surface

pitting, which can be seen in Appendix Figure B.8d (a higher magnification image has been included in Appendix Figure B.9).

5.5 Discussion

Sulphate had a systematic effect on the removal of Sr from the solution, with higher sulphate concentrations leading to lower incorporation of Sr into the calcium carbonate. XRD data suggests that the presence of Na_2SO_4 did generate a slightly different crystallization pathway than sulphate free experiments. At the 8 minute time point Na_2SO_4 was present (Figure B.1), likely due to crystallization in the stock solution, which was near saturation. Gypsum was observed after 1 hr alongside calcite, and calcite was the only phase observed after 6 hrs. It was after 6 hrs when most Sr was precipitated (6-48 h). This interval was dominated by the calcite polymorph so the intermediaries are unlikely to have affected the coprecipitation of Sr.

PHREEQC modelling suggests that as SO_4^{2-} concentration increases the complexation of both Ca^{2+} and Sr^{2+} by SO_4^{2-} increases. This leads to a reduction in the aqueous ion activity for these ions and thus a reduction in the saturation indices for both Calcite and Strontianite (Figure 5.5). This complexation of Sr by sulphate is most likely the reason for its lower D_{Sr} in the high sulphate experiments, as previous experiments found that Sr was most effectively removed from batch precipitation experiments after TIC had accumulated sufficiently to supersaturate strontianite. Due to the lower activity of Sr^{2+} in the high SO_4^{2-} experiments a greater accumulation of TIC will be required to supersaturate strontianite.

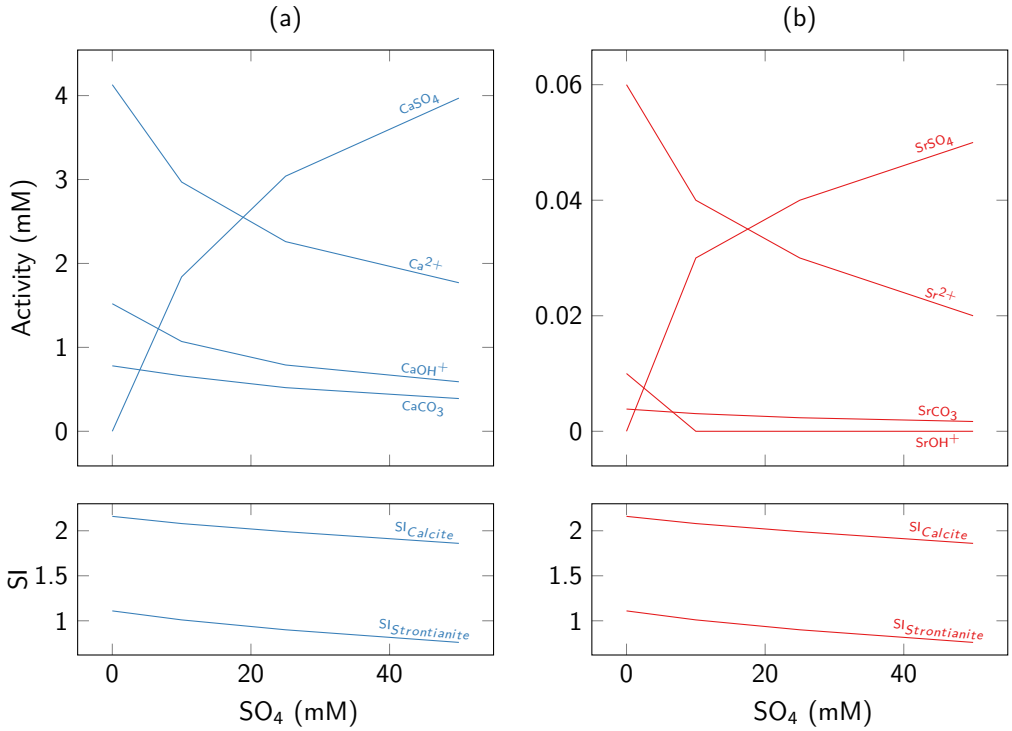

Figure 5.5: Distribution of (a) Ca and (b) Sr solution species with increasing solution SO_4 plotted with changing Saturation indices for Calcite and Aragonite.

Figure 5.6 shows the evolution of solution Sr^{2+} with time. All systems show a gradual decline in the Ca:Sr over the first 24 hrs. This is a result of Ca^{2+} being preferentially incorporated in the calcite over Sr^{2+}. In the absence of sulphate the decrease in Ca:Sr was followed by a rebound caused by enhanced Sr^{2+} incorporation, suggesting a new mechanism of Sr^{2+} into the calcite. The strength of this rebound shows a systematic decline with increasing sulphate, which suggests that the sulphate is inhibiting the enhanced Sr^{2+} uptake at low Ca:Sr.

5.5.1 Aragonite inhibition

All experiments aimed at producing aragonite failed to achieve their goal. It is therefore clear that the precipitation mechanism that favours aragonite at low pH does not operate

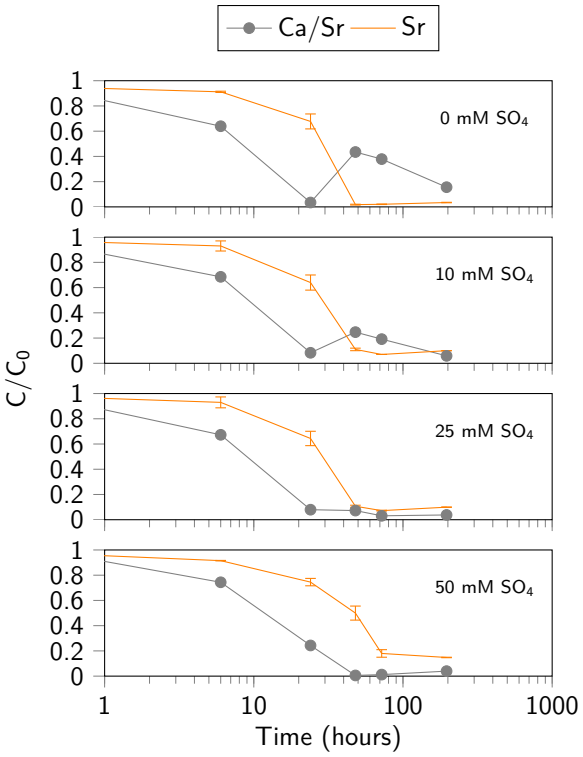

Figure 5.6: Effect of increasing sulphate concentration on the Ca:Sr ratio of the solution

effectively at high pH. A key difference between a low and high pH solution, in terms of carbonate precipitation is the speciation of TIC. In solutions with pH >10.3 The majority of solution TIC is speciated as CO_3^{2-} rather than HCO_3^-. Gebauer et al. (2008) suggest that under high pH conditions, with more carbonate ions present, calcium ions are more effectively bound in prenuleation clusters. It is therefore possible that a change in prenucleation structure could generate the differences observed in polymorphs across the range of pH's studied (Hu et al., 2015).

Another potential difference is the effect of high pH on the calcite surface. At pH 8.2 calcite has a neutral surface charge, as the pH increases a negative charge is generated by deprotonation of hydroxyl groups bound to the calcite surface (Fenter et al., 2000). The effect of this change in surface charge is unclear however it may prevent the aggregation

of calcite particles as well as affecting the interfacial free energy of the calcite changing how effectively it can act as seed particles (Chevalier, 2014). If the increased surface charge generated at high pH were able to stabilise the calcite surface it can be predicted to be the dominant high pH carbonate polymorph (as most other polymorphs are formed due to processes destabilising calcite in solution).

5.5.2 Role of seed crystals

The presence of calcite seed crystals allowed carbonate precipitation to proceed at a faster rate. This resulted in a decreased induction period and a more rapid removal of ^{14}C. The remobilization of ^{14}C which, in the unseeded system, has been shown to be caused by the recrystallization of an metastable precipitate, was present regardless of the seed crystal surface area and increased slightly with increasing seed surface area. SEM images are presented in figure B.8. These suggest that the precipitate inherited the structure of the seed crystals as no other morphologies were observed. However, due to the volume of seed crystals it was only possible to observe a small fraction of these under the SEM. Due to uncertainties in the precipitation mechanism the explanation of the observed ^{14}C remobilization increase remains unclear. The timing, contemporaneous with the remobilization in the 0 m^2 L^{-2} system, suggests the same cause (the recrystallization of a metastable precipitate) however, SEM images were inconclusive in determining whether the precipitates are inheriting the seed crystal morphology or nucleating as separate crystals with a distinct morphology. If the ^{14}C calcite is precipitated with the same morphology as the seed crystals it is possible that the remobilization was caused by dissolution of the calcite surface as the pH dropped.

From 6-24 h, the window in which the remobilization commenced, a pH decrease of 0.51 pH units was observed due to CO_2 in-gassing. This mechanism explains the enhanced remobilization in the seeded experiments as these will have reached equilibrium more rapidly and thus be further from equilibrium as the pH fell.

Sr removal was facilitated by the presence of seed crystals with removals in excess of the ICP-OES limit of detection (99.8%) observed. The most effective Sr removal was achieved between 24-48 h, after the Ca concentration had been reduced to 0.058 mM. During this interval 0.08 mM Sr was removed alongside 0.05 mM Ca. This suggests that either the Sr is precipitating as a strontianite like phase or is removed through sorption to the calcite surface. The removal of Sr through sorption fits with the observation that Sr removal is enhanced by larger seed crystal surface areas.

5.6 Conclusions

pH appears to play a significant role in determining which carbonate polymorph will precipitate from a solution. Controls on carbonate polymorphism at circumneutral pH have been well established, with Mg^{2+} binding to the calcite surface and inhibiting the subsequent attachment of Ca^{2+} ions, SO_4 substituting for CO_3^{2-} in calcite and aragontite, inhibiting both polymorphs; and high temperature (>35°C) inhibiting calcite and favouring aragonite.

Alkaline conditions appear to have a significant impact on the nucleation of calcium carbonate polymorphs. Mg^{2+} is not soluble, Sulphate appears to slightly inhibit calcite precipitation (figure 5.6) however its effect is minimal. The presence of seed crystals

did not negate the remobilization of ^{14}C observed in previous experiments. However, seeding did lead to a significantly shorter induction period, with >50% of ^{14}C removed within the first 30 s. This produced a removal window, lasting from 50 min - 6 h during which the ^{14}C removal in all systems was 99.9-94.4 %. This stable removal window of 5 h is potentially valuable for a remediation scheme and may make the separation of the ^{14}C calcite before its recrystallization viable.

Increased seed crystal surface area also had a beneficial impact on the removal of Sr from solution, potentially due to adsorption of Sr^{2+} to the negatively charged calcite surface, or lowering the effective supersaturation required for calcite precipitation.

Bibliography

Blanco-Gutierrez, V., Demourgues, A., Jubera, V., Gaudon, M. (2014). Eu(III)/Eu(II)-doped (Ca 0.7 Sr 0.3) CO3 phosphors with vaterite/calcite/aragonite forms as shock/temperature detectors. *J. Mater. Chem. C*, **2**(46), pp. 9969–9977.

Bots, P., Benning, L.G., Rickaby, R.E.M., Shaw, S. (2011). The role of SO4 in the switch from calcite to aragonite seas. *Geology*, **39**(4), pp. 331–334.

Cabrera, N., Vermilyea, D.A. (1958). Growth and perfection of crystals. *Wiley, New York*, p. 393.

Chevalier, N.R. (2014). Do surface wetting properties affect calcium carbonate heterogeneous nucleation and adhesion? *Journal of Physical Chemistry C*, **118**(31), pp. 17600–17607.

Fenter, P., Geissbühler, P., DiMasi, E., Srajer, G., Sorensen, L.B., Sturchio, N.C. (2000). Surface speciation of calcite observed in situ by high-resolution X-ray reflectivity. *Geochimica et Cosmochimica Acta*, **64**(7), pp. 1221–1228.

Fernández-Díaz, L., Fernández-González, Á., Prieto, M. (2010). The role of sulfate groups in controlling CaCO3 polymorphism. *Geochimica et Cosmochimica Acta*, **74**(21), pp. 6064–6076.

Finch, a.a., Allison, N. (2007). Coordination of Sr and Mg in calcite and aragonite. *Mineralogical Magazine*, **71**(October 2007), pp. 539–552.

Fujita, Y., Ferris, F.G., Lawson, R.D., Colwell, F.S., Smith, R.W. (2000). Calcium

carbonate precipitation by ureolytic subsurface bacteria. *Geomicrobiology Journal*, **17**(4), pp. 305–318.

Gebauer, D., Volkel, A., Colfen, H. (2008). Stable Prenucleation Calcium Carbonate Clusters. *Science*, **322**(5909), pp. 1819–1822.
URL: *http://www.sciencemag.org/cgi/doi/10.1126/science.1164271*

Hu, Y.B., Wolthers, M., Wolf-Gladrow, D.A., Nehrke, G. (2015). Effect of pH and phosphate on calcium carbonate polymorphs precipitated at near-freezing temperature. *Crystal Growth and Design*, **15**(4), pp. 1596–1601.
URL: *http://pubs.acs.org/doi/abs/10.1021/cg500829p*

Kinsman, D.J.J., Holland, H.D. (1969). The co-precipitation of cations with CaCO3—IV. The co-precipitation of Sr2+ with aragonite between 16° and 96°C. *Geochimica et Cosmochimica Acta*, **33**(1), pp. 1–17.

Marshall, J.F., McCulloch, M.T. (2002). An assessment of the Sr/Ca ratio in shallow water hermatypic corals as a proxy for sea surface temperature. *Geochimica et Cosmochimica Acta*, **66**(18), pp. 3263–3280.

Mitchell, A.C., Ferris, F.G. (2005). The coprecipitation of Sr into calcite precipitates induced by bacterial ureolysis in artificial groundwater: Temperature and kinetic dependence. *Geochimica et Cosmochimica Acta*, **69**(17), pp. 4199–4210.

Tai, C.Y., Chen, F.B. (1998). Polymorphism of CaCO3, precipitated in a constant-composition environment. *AIChE Journal*, **44**(8), pp. 1790–1798.

Chapter 6

Enhanced Crystallographic incorporation of Strontium(II) ions to Calcite via Preferential Adsorption at Obtuse Sites during Spiral Growth

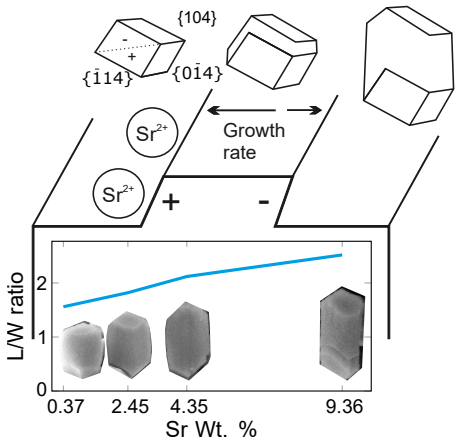

6.1 Summary

Sr-containing calcium carbonates were precipitated from solutions containing $Ca(OH)_2$, $SrCl_2$ and Na_2CO_3 in a reactor where constant solution composition was maintained.

The total concentration of divalent ions was same in all experiments, but the Sr/Ca ratio was varied between 0.002 and 0.86, and the pH value was between 12.02 and 12.25. All solutions were oversaturated with respect to calcite ($SI_{calcite}$ = 1.1-1.4). Calcite was the only product formed at low Sr/Ca ratios, but at Sr/Ca $\geq$ 0.45 strontianite was detected in some systems. Sr-rich precipitate was observed in both a surface layer on (6.9-6 μm) rhombic calcite seed crystals and as smaller (> 3.64-1.96 μm) calcite crystals that were elongated along their C-axis. The degree of crystal elongation increased with the Sr/Ca ratio in those crystals. Precipitates recovered from low Sr/Ca ratio experiments exhibited an XRD spectrum identical to that of rhombic calcite, however the peaks attributed to Sr-containing calcite shifted progressively to lower 2θ values with increasing solution Sr/Ca ratio, indicating increased lattice volume. Sr K-edge EXAFS analysis of the precipitates showed that the shift in morphology and lattice volume is accompanied by a change in the local coordination of Sr^{2+} in calcite. The Sr-O bond lengths were similar to the Ca-O bond lengths in calcite, but Sr-O coordination increased from 6 fold in crystals containing 0.21 Wt. % Sr, to 8 fold in crystals containing 9.47 Wt. % Sr, and the Sr-Ca coordination decreased from 6 and 6 (for the first and second Sr-Ca shells respectively) to 4 and 1. It is suggested that Sr^{2+} undergoes preferential incorporation at obtuse (+) growth sites on the calcite surface due to its large ionic radius (1.13 Å), and this increases the growth rate parallel to the C-axis, resulting in the observed elongation in this direction.

6.2 Introduction

The transfer of trace elements from solution to solid calcium carbonate has received a significant amount of interest across a range of fields. The Sr content of biogenic carbonates, both aragonite and calcite, has been used to reconstruct paleo-climatic conditions (Weber, 1973; de Villiers et al., 1994; Stoll et al., 2002; Ruiz-Agudo et al., 2011). Trace element incorporation has been used to understand crystal growth (Yoreo and Dove, 2004; Davis et al., 2004; Paquette and Reeder, 1995). Furthermore the coprecipitation of Sr into calcium carbonates has been proposed as an attenuation and remediation mechanism for ^{90}Sr contamination in groundwater (Fujita et al., 2000; Warren et al., 2001; Mitchell and Ferris, 2005).

The three main polymorphs of calcium carbonate found in geological deposits are calcite, aragonite and vaterite in order of decreasing stability. Calcite is characterised by rhombohedral coordination, with the central calcium atom surrounded by 6 oxygen atoms with Ca-O bond lengths of 2.36 ; this is the most stable polymorph in most environmental settings. Aragonite has a more open structure. The central calcium atom is surrounded by 9 oxygen atoms with Ca-O bond lengths of 2.42-2.66 (Blanco-Gutierrez et al., 2014). Vaterite is the lest stable calcium carbonate morphology, with the central calcium atom surrounded by 8 oxygen atoms with Ca-O bond lengths of 2.29-2.90 Å(Blanco-Gutierrez et al., 2014). Aragonite formation is favoured by high temperature/pressure environments (Burton and Walter, 1987), and by the presence of Mg^{2+} and SO_4^{2-} ions (Davis et al., 2004; Bots et al., 2011). Sulphate ions compete for the carbonate site and, due to the larger sites in aragonite, sulphate hinders the growth of this polymorph the least (Fernández-Díaz et al., 2010). Magnesium ions

compete for the calcium sites. Mg^{2+} ions are smaller than Ca^{2+} ions, and therefore preferentially adsorb to calcite over aragonite, due to the smaller calcium sites therein. However, due to its higher hydration energy (Rodriguez-Cruz et al., 1999) Mg^{2+} retards growth at the calcite surface after adsorption, favouring the precipitation of aragonite. Furthermore, due to the presence of acute and obtuse growth sites at the calcite surface (which affects the geometry/size/adsorption properties of the calcite sites), Mg^{2+} affects the morphology of the calcite crystals by preferentially adsorbing to the acute sites due to its small ionic radius (Davis et al., 2004).

The incorporation of Sr^{2+} into carbonates is dependent on a number of factors. Strontium may substitute for calcium in the carbonate lattice due to similarities in their ionic radius and charge. However, strontium's larger ionic radius (Ca=1.0 Sr=1.13) introduces strain to the mineral lattice, eventually destabilising it at high incorporation rates (Tesoriero and Pankow, 1996; Nielsen et al., 2013).

It has been proposed that while incorporation of low levels of Sr^{2+} into the calcite lattice may be favourable (although the effect may be within error), increasing Sr^{2+} concentrations result in a sharp decrease in step growth speed at both obtuse and acute sites (Wasylenki et al., 2005). This latter trend been modelled by calculating step growth rates from a solid solution between rhombohedral calcite and strontianite endmembers, and by assuming that Sr2+ in the calcite lattice alters the ion activity product of $CaCO_3$ resulting in a higher detachment rate of Ca^{2+} ions from the lattice which slows step growth (Nielsen et al., 2013).

Fast crystallisation rates favour Sr^{2+} incorporation into calcite by minimising the amount of time the Sr^{2+} is exposed at the calcite surface and able to be desorbed and

replaced by a more favourable cation (Lorens, 1981; Gabitov and Watson, 2006; Tang et al., 2008; Gabitov et al., 2014). Mg^{2+} is also known to enhance the incorporation of Sr^{2+} into calcite. Mg^{2+} is smaller than Ca^{2+}, which in conjunction the larger Sr^{2+} ion balances the lattice strain, enabling greater Sr^{2+} incorporation (Littlewood et al., 2017). Strontium's local coordination environment within the carbonate lattice will also have a significant impact on its distribution coefficient. The larger M^{2+} sites in aragonite allow for greater incorporation of Sr^{2+} relative to calcite (Curti, 1999). Previous work by Matsunuma et al. (2014) used an amorphous calcium carbonate (ACC) pathway to improve the incorporation of trace metals such as Sr into the calcite lattice. Littlewood et al. (2017) found that this technique produced calcite through a vaterite intermediary, and that Sr^{2+} coprecipitated through this pathway retained its vaterite like local environment (within the calcite crystals), indicating reaction pathways are critical for Sr incorporation into calcite.

This paper investigates how Sr is incorporated in calcite, and whether the mechanism of strontium incorporation into calcite changes as the amount of Sr incorporation increases. A series of constant solution composition experiments were conducted in a continuous tank stirred reactor (CTSR) that was seeded with calcite crystals. The total concentration of divalent ions in the reactor feedstock was constant across the experimental series, but the Sr/Ca ratio in individual experiments was varied between 0.002 and 0.86. Precipitates recovered from the reactor at different Sr/Ca ratios were analysed by (i) scanning electron microscopy to observe the crystal morphology and determine the Sr/Ca ratio in different polymorphs by energy dispersive spectroscopy, (ii) x-ray diffraction spectroscopy to determine minerals present and to provide information

on their unit cell dimensions, (iii) and x-ray absorption spectroscopy to determine of the coordination environment around Sr ions incorporated into newly formed minerals.

6.3 Experimental Section

6.3.1 Continuous tank stirred reactor (CTSR) experiments

The continuous tank stirred reactor (CTSR) consisted of a 150 mL spherical reaction vessel with two inlets for the mixed $Ca(OH)_2/SrCl_2$ solution and Na_2CO_3 solution (Quickfit® jointed borosilicate glassware). The concentrations of divalent cations in the stock solution were maintained at a constant concentration of 8.73 $\pm$ 0.34 mM, but the Sr/Ca ratio was varied. Na_2CO_3 was added at a nominal concentration of 50 $\pm$ 0.024 mM to all experiments. The divalent metal and carbonate solutions were fed into the reactor at a constant rate of 135 mL h-1 (1.18 mmol h^{-1}) and 15 mL h-1 (0.75 mmol h^{-1}) respectively to produce a constant solution composition within the reactor with an excess of M^{2+} ions. The pH of the reactor varied between 12.02 and 12.25. The output fluxes of M^{2+} ions was measured (see below), and the precipitation rate was calculated from the difference between the input and ouput fluxes (it varied from 0.74-1.10 mmol h^{-1}).

Initial unseeded experiments produced both calcite and aragonite across a range of Sr:Ca ratios, with no systematic trend (see SI Table 1). Therefore calcite seed crystals with a total mass of 0.73 g (1 m^2 L^{-1}) were added to the reactor at the start of the tests to ensure that calcite was the only polymorph produced (SI Table 2). The CTSR was initially run for 5 h (with a flow rate of 150 mL h^{-1} to replace 1 reactor volume/hour)

after which time 3 solution samples (4 mL) were taken at 1 h intervals to confirm that the solution composition in the reactor had equilibrated, and to determine the Ca:Sr ratio. Solution samples were filtered (0.2 μm Polyethersulfone hydrophilic filters) and the temperature and pH were determined using an Orion 420 pH meter with a VWR SJ113 probe (calibrated at pH 7.0, 10.01 and 12.46). A 1 mL subsample of the filtrate was then added to 9 mL of 0.1 M Aristar® grade HNO_3 (VWR International, USA) for chemical analysis.

At the end of each 7 hour experiment all the precipitate in the reactor was collected by passing the reactor solution through a Buchner filter with Sartorius Stedim Polycarbonate Track-Etch Membrane filter paper. The precipitate was thoroughly rinsed with isopropyl alcohol, after which it was stored in a desiccator. Subsamples of the precipitate (4 mg) were dissolved in 10 mL of 0.1 M Aristar® grade HNO_3 for chemical analysis. Sr and Ca concentrations in the reactor solutions and the precipitate were determined by Ionically Coupled Plasma Optical Emission Spectroscopy (ICP-OES) (Thermo iCAP 7400, Thermo Fisher Scientific, Inc, USA).

6.3.2 Scanning Electron Microscopy and Energy Dispersive Spectroscopy

Precipitate samples were mounted on carbon tape, attached to aluminium stubs and coated with iridium for Scanning Electron Microscope (SEM) analysis on a FEI Quanta 650 Field Emission Gun SEM to investigate crystal morphology. One sample containing 6.36 Wt. % Sr was set in epoxy resin and polished using silicon carbide paper followed by a water-free diamond paste to provide a smooth surface for Energy Dispersive

Spectra (EDS) analysis which was carried out on a Tescan VEGA3 XM, equipped with X-max 150 SDD EDS and Aztec 3.3 data acquisition software.

6.3.3 X-ray Diffraction

Calcite precipitates recovered from the reactor at the endpoint of the experiments were mixed with a small portion of silicon standard and mounted on low background silicon sample holders (the use of a standard enables the resultant XRD pattern to be corrected). Mineralogical analysis was carried out using a Bruker D8 XRD with a Cu Kα1 source.

6.3.4 X-ray Adsorption Spectroscopy

Sr K-edge (16,105 eV) X-ray absorption spectra were collected from selected Sr-containing carbonate precipitates on beamline B18 at the Diamond Light Source. Samples were prepared as pressed pellets, dispersed with cellulose and held in Kapton® tape. Samples were mounted a liquid nitrogen cryostat (80 K) during data collection to minimise noise. At beamline B18 focussing of the beam produces a spot size of 200 x 250 μm. Spectra were gathered from high concentration samples in transmission mode, and in fluorescence mode (using a 9 element Ge solid state detector) for low concentration samples. Multiple XAS scans from each sample were summed and averaged using Athena (version 0.9.25) to maximise the signal/noise ratio. Normalised X-ray absorption near edge structure (XANES) data were plotted and compared to Sr K-edge XANES spectra collected from (Sr-containing) calcite, aragonite and strontianite standards. EXAFS spectra were then extracted and fitted in k-space using Artemis (version 0.9.25) Ravel and Newville (2005) to fit the data using the Markgraf and Reeder

Markgraf and Reeder (1985) calcite model structure.

6.4 Results

XRD

XRD analysis of precipitate from the CTSR reactor experiment with a solution Sr/Ca ratio of 0.002 exhibited a peak profile consistent with calcite, displaying a maximum intensity peak at 29.4° 2θ, and secondary peaks at 39.5°, 39.4°, 43.1°, 47.5°, and 48.5° 2θ. These peaks are consistent with a pure calcite sample. XRD analysis of the other precipitates from the CTSR reactor experiment exhibited essentially the same peak profile, however the spectra showed clear variation with increasing Wt. % Sr (Figure 6.1). As the Sr content of the calcite increased the peaks in the XRD spectra exhibited broadening and a shift in the maximum intensity to lower 2θ. Above 2.45 Wt. % splitting of the calcite peaks was also observed. It is possible that this splitting was present in lower concentration samples but was masked by the proximity of the peaks (a clear asymmetry can be seen in the 2.45 Wt. % samples).

After Sr Wt. % in the precipitate exceeded 9.23 strontianite was first detected in XRD patterns, and became the dominant end product observed when Sr Wt. % in the precipitate exceeded 9.36 (SI Table 2). Precipitates containing detectable strontianite were not included in the subsequent analysis of Sr incorporation in calcite.

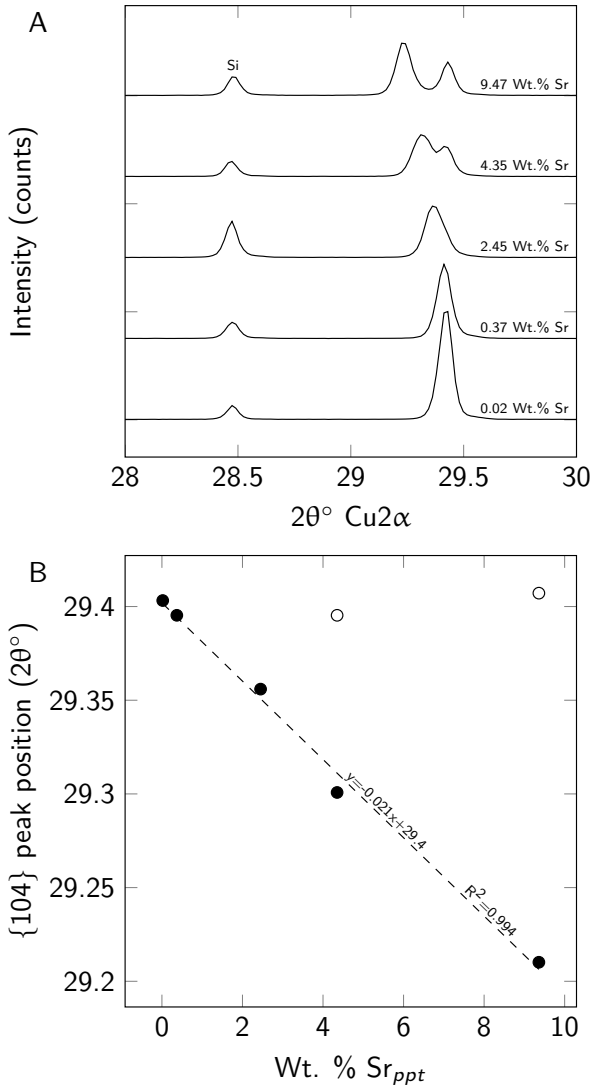

Figure 6.1: A) XRD traces displaying peak broadening and subsequent splitting of the calcite {104} peak at 2θ 29.4° (together wither the silicon standard peak at 2θ=28.46°) B) $2\theta^{\circ}$ position of the strained and unstrained {104} calcite peak (closed and closed symbols respectively

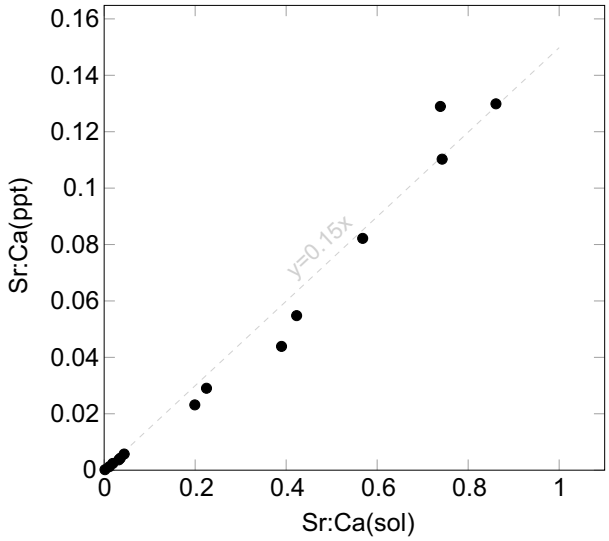

Figure 6.2: Variation in the Sr:Ca ratio in precipitates as a function of Sr:Ca ratio in solution. Trend line calculated by linear regression indicates DSr=0.15.

6.4.1 Sr/Ca ratio in the precipitates

In experiments where the precipitate contained less than 9.36 Wt. % Sr there was an approximately linear relationship ($Sr/Ca_ppt = 0.15 \times Sr/Ca_Aq$) between the Sr/Ca ratio measured in the precipitate and that measured in reactor solution (Figure 6.2). The gradient is equivalent to the Berthelot-Nernst distribution coefficient (Eq. 6.1). Three experiments where $SI_{strontianite}$ was ≥ 2.2 produced precipitates with a D_Sr >0.2.

$$D_{Sr} = \frac{[Sr]/[Ca]_{ppt}}{[Sr]/[Ca]_{sol}} \tag{6.1}$$

6.4.2 Precipitate morphology

Precipitates from these experiments were characterised as a mixture of larger rhombs ($\bar{x}$ 6.9-6.0 μm) and smaller elongate crystals ($\bar{x}$ 3.64-1.96 μm) with rhombic ends and cylindrical centres (Figure 6.3). With increasing Wt. % Sr the elongate crystals present

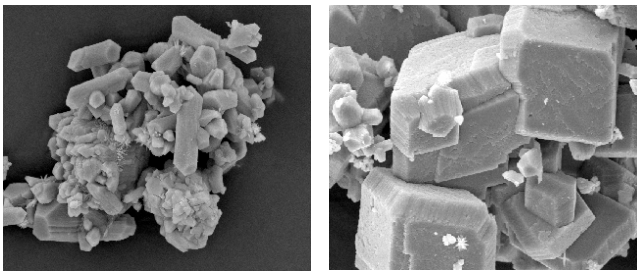

Figure 6.3: Two SEM images from an experiment with 9.36 Wt.% Sr displaying the two calcite morphologies. A) Elongate calcite B) Rhombic Calcite.

Table 6.1: Wt.% Sr and D_{Sr} for the range of precipitates analyzed

#	Sr/Ca (solution)	Sr/Ca (ppt)	Sr (Wt. %)	DSr	L/W* (Median)
50	0.00	0.00	0.02	0.10	1.59
65	0.01	0.00	0.11	0.11	
66	0.02	0.00	0.21	0.13	
58	0.03	0.00	0.32	0.11	
57	0.04	0.00	0.37	0.12	1.61
51	0.04	0.01	0.50	0.13	
59	0.20	0.02	1.96	0.12	
52	0.22	0.03	2.45	0.13	1.82
60	0.39	0.04	3.59	0.11	
53	0.42	0.05	4.35	0.13	2.13
61	0.57	0.08	6.36	0.14	
67	0.74	0.11	8.30	0.15	
54	0.86	0.13	9.36	0.15	2.50
63	0.74	0.13	9.47	0.17	

= sample number; L/W = length/width ratio

*elongate crystals only; average of > 100 measurements for each sample.

in the precipitate displayed a clear trend of increasing length/width ratio, summarised in Table 1. The larger rhombs had average length to width ratios of 0.87.

6.4.3 EDS

EDS mapping was carried-out on 4 separate regions on a resin embedded calcite sample with 6.36 Wt. % Sr. Representative images of the back scattered electron image (BSEI) and Sr, Ca and O maps are included in Figure 6.4. The BSEI identifies a large rhombic

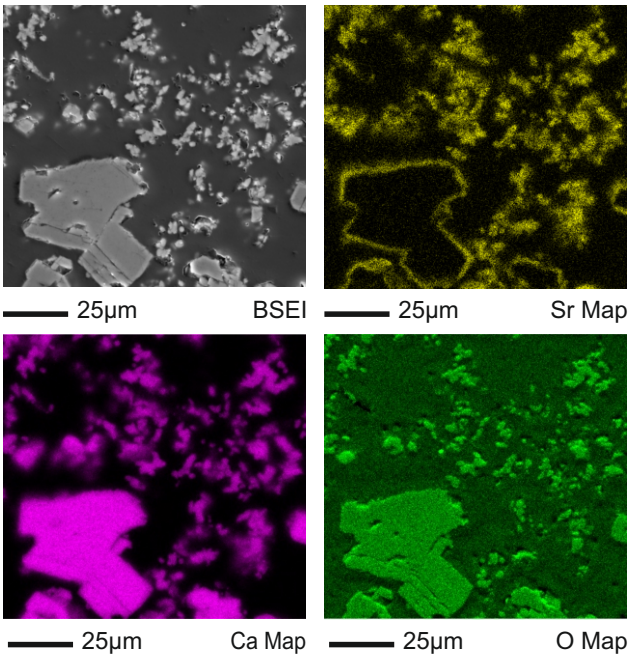

Figure 6.4: Back Scattered Electron Image with Sr, Ca, and Cl EDS element maps from a 6.36 Wt.% sample

crystal (lower right corner) and the fine elongate crystals (occupying the rest of the image). Ca and O maps also highlight these crystals and indicate the crystals have uniform distribution of calcium and carbonate. Sr maps indicates that the rhombic crystals have Sr rich rims but low Sr interiors, while Sr is more uniformly distributed in the elongate crystallites (SI Figure 3).

6.4.4 XAS

Analysis of strontium's coordination environment by XAS is presented in Table 6.2. The lowest Wt.% sample displays Sr-O, Sr-C and Sr-Ca bond lengths and coordination values similar to those observed for Ca-O, Ca-C and Ca-Ca in pure calcite. The lowest Wt.% sample displayed a peak at 16,108 eV and another at 16,119 eV (Figure 6.5). As the Wt.% Sr in the calcite increased the 16,119 eV peak decreased in relative magnitude to become a shoulder to the 16108 eV peak in the 9.47 Wt.% sample. This

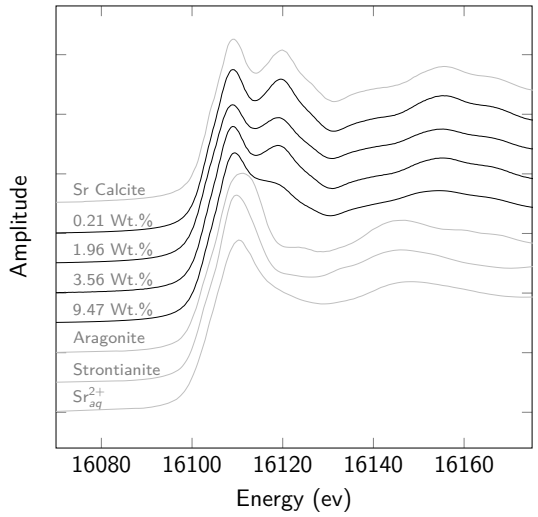

Figure 6.5: Sr XANES spectra collected from a series of increasing Sr Wt.% samples (black lines), plotted with selected standard data (grey)

is consistent with a transition from calcite like coordination environment to a more strontianite/aragonite like coordination environment (both strontianite and aragonite have a 9-fold coordination environment around the divalent metal ion).

Fitting of EXAFS data suggests that low concentrations of Sr^{2+} (0.21 Wt.%) are able to fit into the calcite structure maintaining 6-fold Sr-O coordination, but with a Sr-O bond length of 2.43 $\pm$ 0.09 (the Ca-O bond length in pure calcite is 2.36 ref 22). At higher Sr incorporation (>1.96 Wt.%) the Sr-O bond length was similar (2.44 $\pm$ 0.02), but the best fit for Sr-O coordination increased to 7. The most concentrated sample (9.56 Wt.%) was best fit with 8 fold Sr-O coordination, more similar to that of strontianite/aragonite although the Sr-O bond length is shorter than in strontianite (which has a Sr-O bond length of 2.59 Finch and Allison (2007)). Thus, the Sr-O co-ordination number progressively increased with increasing Sr incorporation.

Coordination of Sr-C remained at 6 in all samples observed, with bond distances decreasing from 3.22 $\pm$ 0.09 to 2.93 $\pm$ 0.05 in the 9.47 Wt. % sample. These fits show

increased Debye-Waller ($\sigma 2$) values which result from carbons low atomic mass and weak electron scattering, and indicates a higher degree of uncertainty in these values.

Bond lengths between Sr and the first and second shells of Ca atoms remained similar across the series (first shell 4.02-4.03 , second shell 4.99-5.04), however, there was a progressive decrease in the transform amplitudes observed above 3 (Figure 6.6). As a result, the best fit coordination numbers systematically decreased through the series from 6 and 6 for the first and second shell respectively in the 0.21 Wt.% sample to 4 and 1 in the 9.47 Wt. % sample.

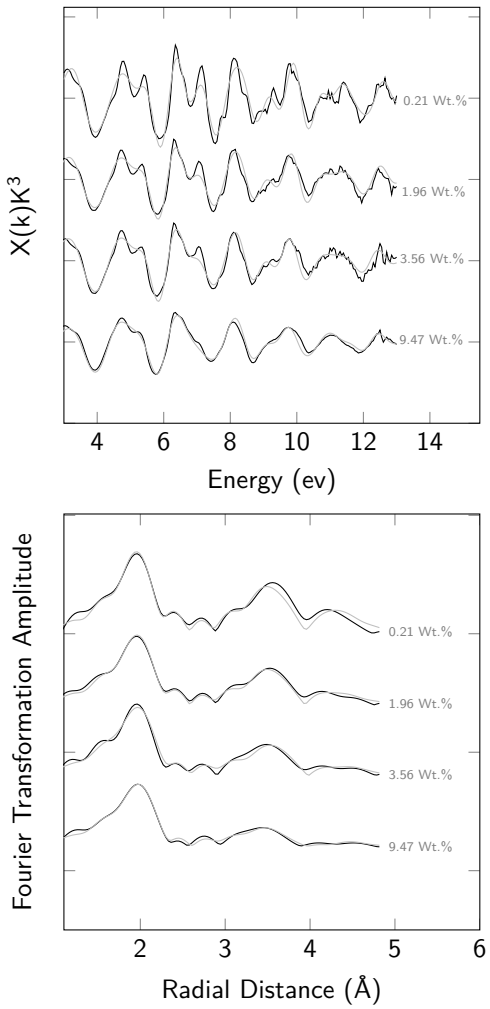

Figure 6.6: A) EXAFS spectra collected from a series of increasing Sr Wt.% samples and B) corresponding Fourier transformations (FT). Model fits using the data shown in Table 2 are also provided for each sample in grey.

6.5 Discussion

6.5.1 Effect of solution composition on reaction product

In this study Sr bearing calcites were precipitated that contained up to 9.36 Wt. % Sr, which was the upper limit for Sr incorporation to calcite observed in these experiments. Two samples displayed a greater Sr Wt. % (SI Table 2) however, XRD analysis indicates one contained strontianite alongside calcite, and both displayed D_{Sr} >2. A $D_{Sr} > 2$ was therefore used to identify any further experiments which may have been affected by strontianite precipitation. D_{Sr} for Sr incorporation into calcite showed little variation prior to the formation of strontianite (D_{Sr}=0.10-0.17), indicating similar rates of carbonate precipitation in these experiments (Lorens, 1981). A minor increase in D_{Sr} was observed toward the upper end of our experimental range, prior to the detection of strontianite through XRD. This may indicate the formation of some strontianite below limits of detection for this technique.

6.5.2 Mode of Sr incorporation to calcite

The {104} main XRD peak of Sr substituted calcite, which is nominally at 2θ = 29.4°, exhibits a linear trend of decreasing $2\theta°$ position with increasing Sr Wt. % (Figure 6.1). This indicates that there is a progressive expansion of the calcite lattice volume with increasing Sr^{2+} incorporation Ravel and Newville (2005). Samples with 4.35 and 9.36

Table 6.2: EXAFS fitting parameters calculated for selected calcite samples in Artemis. Standard data for Calcite ([22] Markgraf and Reeder (1985), [18] Littlewood et al. (2017), [25] Finch and Allison (2007), [26] De Villiers (1971)), Aragonite and Strontianite are included for comparison.

	Shell	N	R ()	σ^2	R-Factor	χ^2
Calcite[22]	O	6	2.36			
	C	6	3.21			
	Ca	6	4.05			
	Ca	6	4.99			
0.21 Wt. %	O	6	2.43(9)	0.0043	0.034	1096
	C	6	3.19(7)	0.0176		
	Ca	6	4.03(1)	0.0061		
	Ca	6	4.94(2)	0.0066		
1.96 Wt. %	O	7	2.44(1)	0.0050	0.023	782.4
	C	6	3.16(5)	0.0258		
	Ca	5	4.03(1)	0.0055		
	Ca	5	4.97(2)	0.0083		
3.59 Wt. %	O	7	2.45(1)	0.0068	0.021	293.5
	C	6	2.78(6)	0.0266		
	Ca	4	4.05(1)	0.0067		
	Ca	3	5.02(3)	0.0085		
9.47 Wt. %	O	8	2.45(1)	0.0066	0.01	1195.9
	C	6	0.21(5)	0.1243		
	Ca	4	4.03(1)	0.0083		
	Ca	1	5.04(4)	0.0043		
Sr-Calcite[18] (5.4 Wt. %)	O	9	2.57			
	C	5	3.10			
	Ca	4	4.12			
Aragonite[25]	O	9	2.58			
	C	6	2.98			
	Ca	6	4.02			
Strontianite[26]	O	9	2.59			
	C	6	3.03			
	Sr	6	4.09			

Wt. % Sr display peak splitting, the right hand peak is Sr-free calcite (probably the seed crystals), while the left hand peak results from calcite that has become disordered due to the presence of Sr (present as both overgrowths on rhombic seed crystals and as elongate crystals). The 2.45 Wt. % sample does not display splitting on the {104} peak however this peak displays a shift in its $2\theta^{\circ}$, fitting on a linear trend with the other samples. It is therefore likely that this peak is a composite of two peaks, a pure calcite peak and a disordered Sr-calcite peak, which were too close together to be resolved by the XRD software. This interpretation is supported by the EXAFS data, which shows Sr is incorporated into the Ca site within the calcite lattice, and bond lengths calculated in Artemis suggest the strain imparted by increasing the Sr Wt. % causes a change in the coordination environment of Sr. An increase in the coordination of O atoms around the Sr, reflecting a larger M^{2+} site. A decrease in the long-range Sr-Ca coordination was also observed which indicates an expansion of the M^{2+} sites resulting in increasing distortion of the calcite lattice. The local environment for Sr within calcite progressed from a rhombohedral calcite like coordination to one more similar to the orthorhombic aragonite/strontianite structure (Figure 6.5). This coordination environment differs from that reported in Littlewood et al. (2017), who found that when calcite is formed from the reordering of an ACC precursor through a vaterite intermediary the Sr^{2+} was retained in a vaterite like environment. The difference in Sr^{2+} coordination between this study and that reported by Littlewood et al. (2017) indicates that the crystallization pathway impacts not only how effectively a trace element may be incorporated but also its local coordination environment.

6.5.3 Effect of Sr^{2+} on calcite morphology

SEM analysis of five precipitates with Wt. % Sr ranging from 0.02-9.36 identified two distinct calcite morphologies, a rhombohedral and an elongate form. Image analysis from these precipitates indicate that the L/W ratio of the elongate morphology displayed a systematic increase as the proportion of Sr in the precipitate increased (Table 1). This correlation between the L/W ratio and the Sr Wt. % implies that the incorporation of Sr favours the growth of a more elongate morphology.

EDS spot analysis indicates that the rhombohedral crystals contain very little Sr throughout their centres, although there is Sr-rich layer at their surface. The Sr-poor core of the rhombic crystals are similar in size to the added calcite seed crystals (SI Figure 4), therefore the rhombic crystal very likely represent a retained fraction of the seed crystals that have been overgrown with Sr-rich calcite during the experiments. Indeed XRD patterns show peaks from two separate calcite phases, one identical to pure Sr-free calcite, the other strained by Sr incorporation. EDS indicates that the maximum concentration of Sr in the Sr-rich overgrowths on rhombic crystals is similar to the average concentration of the smaller elongate crystals. However Sr incorporation in overgrowth layer was typically lower than the elongate crystals, potentially due to the averaging effects of the EDS spot and the narrow rim of Sr incorporation displayed by the rhombic crystals. Therefore we conclude that both the overgrowths and the elongated crystals may have similar amounts of Sr-incorporation (although the mechanism of incorporation may be different).

The SEM-EDS, XRD and EXAFS data together show that Sr is incorporated into calcite and is primarily hosted within its lattice rather than present in surface sorption

complexes. It is also clear that greater incorporation of Sr leads to a change in the local coordination environment of the Sr ion and a greater observed elongation of the initially smaller particles.

Several studies have identified a similar elongate calcite morphology displaying elongation about the c-axis produced by the presence of Mg^{2+} and organic compounds (Davis et al., 2004; Ukrainczyk et al., 2015; Kim et al., 2012). Atomic Force Microscope maps published in Davis et al. (2004) suggest that Mg^{2+} affects the propagation of calcite growth steps by preferentially adsorbing to the acute step sites, causing retardation of the growth rate for these sites and leading to anisotropy in kink propagation.

Due to its larger ionic radius relative to calcium it is expected that Sr^{2+} will preferentially adsorb to the obtuse sites rather than the acute sites. The enhanced growth rate parallel to the c-glide plane suggests that this incorporation of Sr^{2+} is enhancing the growth rate of the obtuse face Figure 6.7. Nielsen et al. (2013) suggest that low concentrations of Sr^{2+} may enhance the calcite growth rate as it is contributing to the net precipitation rate. Step growth rate data (Wasylenki et al., 2005) (which are supported by modelling Nielsen et al. (2013)) displays a more rapid step speed for obtuse steps, with the difference between obtuse and acute steps becoming greater with increasing SI. It is likely that our experiments, which were carried out at SI=0.41-.71 rather than the SI=0.24-0.51 used to measure the step growth rates, would display an even greater obtuse step speed relative to acute steps. Additionally, a threshold followed by a rapid decline in the step growth rates with increasing $[Sr^{2+}]$ is reported (Wasylenki et al., 2005). This threshold results from the impact of trace ions on the solubility of calcite. As the proportion of strontium ions within the lattice increases the lattice bonds become less stable and the rate of

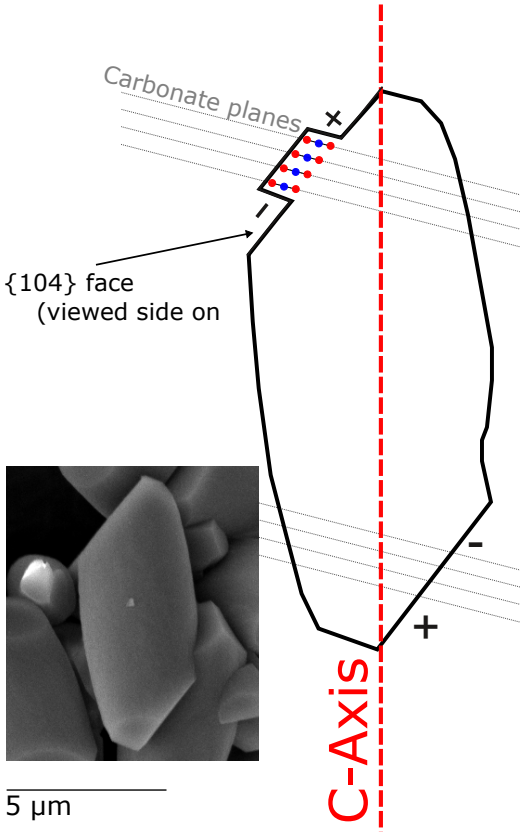

Figure 6.7: Schematic image based on a crystal from the 2.45 Wt. % system. Displaying a side on view of the {104} face and elongating parallel to the C-Axis. A schematic image of the inclination of the carbonate planes with respect to the {104} face is included based on Teng et al. (1998)

ion detachment increases, this effectively destabilises the formation of calcite (Nielsen et al., 2013). This threshold is encountered at increasing [Sr^{2+}] with increasing SI, since our experiments were carried out at greater SI than those presented in (Wasylenki et al., 2005) it is likely that the threshold was not encountered during our experiments.

Sr^{2+} incorporation into calcite produces a similar elongated crystal observed by Mg^{2+} incorporation (Davis et al., 2004) but do so by different mechanisms. Sr^{2+} adsorbs to obtuse sites and enhances growth parallel to the c-glide plane, whereas Mg^{2+} adsorbs to acute sites due to its relatively small ionic radius and retards growth due to its relatively high hydration energy Rodriguez-Cruz et al. (1999), and thus restricts growth orthogonal to the c-glide plane. We suggest that the rhombic morphology does not show

similar elongation to the elongate due to the nature of the Sr incorporation i.e. it is a thin surface layer which cannot influence the shape of the bulk crystal.

6.6 Conclusions

A suite of calcite precipitates displaying a range of Sr^{2+} concentrations were produced in a constant composition reactor. These calcites exhibited increased lattice volume associated with increased Sr content. At low concentrations the Sr^{2+} ion displayed a local environment similar to that of Ca in calcite; with higher concentrations this became more aragonite/strontianite like yet retained a short Sr-O bond length. The presence of Sr^{2+} during calcite growth was found to affect the morphology of the resultant calcite. Precipitates containing greater Sr contents displayed an elongation about their c-axis, most likely caused by preferential adsorption of Sr^{2+} at the obtuse growth steps, allowing an enhanced growth rate at these sites. This study shows that Sr-containing calcite can be produced at relatively high D_{Sr} values in high throughput reactors across a broad range of Sr concentrations. Therefore, controlled Sr-calcite precipitation may potentially be used to remove ^{90}Sr from waste waters present at nuclear sites.

Bibliography

Blanco-Gutierrez, V., Demourgues, A., Jubera, V., Gaudon, M. (2014). Eu(III)/Eu(II)-doped (Ca 0.7 Sr 0.3) CO3 phosphors with vaterite/calcite/aragonite forms as shock/temperature detectors. *J. Mater. Chem. C*, **2**(46), pp. 9969–9977.

Bots, P., Benning, L.G., Rickaby, R.E.M., Shaw, S. (2011). The role of SO4 in the switch from calcite to aragonite seas. *Geology*, **39**(4), pp. 331–334.

Burton, E.A., Walter, L.M. (1987). Relative precipitation rates of aragonite and Mg calcite from seawater: temperature or carbonate ion control? *Geology*, **15**(2), pp. 111–114.

Curti, E. (1999). Coprecipitation of radionuclides with calcite: estimation of partition coefficients based on a review of laboratory investigations and geochemical data. *Applied Geochemistry*, **14**(4), pp. 433–445.

Davis, K.J., Dove, P.M., Wasylenki, L.E., De Yoreo, J.J. (2004). Morphological consequences of differential Mg2+ incorporation at structurally distinct steps on calcite. *American Mineralogist*, **89**(5-6), pp. 714–720.

De Villiers, J.P.R. (1971). Crystal structures of aragonite , strontianite , and witherite. *The American Mineralogist*, **56**, pp. 758–767.
URL: *http://www.minsocam.org/ammin/AM56/AM56_758.pdf*

de Villiers, S., Shen, G.T., Nelson, B.K. (1994). The Sr/Ca-temperature relationship in coralline aragonite: Influence of variability in (Sr/Ca)Seawater and skeletal growth parameters. *Geochimica et Cosmochimica Acta*, **58**(1), pp. 197–208.
URL: *http://www.sciencedirect.com/science/article/pii/001670379490457X*

Fernández-Díaz, L., Fernández-González, Á., Prieto, M. (2010). The role of sulfate groups in controlling CaCO3 polymorphism. *Geochimica et Cosmochimica Acta*, **74**(21), pp. 6064–6076.

Finch, a.a., Allison, N. (2007). Coordination of Sr and Mg in calcite and aragonite. *Mineralogical Magazine*, **71**(October 2007), pp. 539–552.

Fujita, Y., Ferris, F.G., Lawson, R.D., Colwell, F.S., Smith, R.W. (2000). Calcium carbonate precipitation by ureolytic subsurface bacteria. *Geomicrobiology Journal*, **17**(4), pp. 305–318.

Gabitov, R.I., Sadekov, A., Leinweber, A. (2014). Crystal growth rate effect on Mg/Ca and Sr/Ca partitioning between calcite and fluid: An in situ approach. *Chemical Geology*, **367**, pp. 70–82.
URL: *http://dx.doi.org/10.1016/j.chemgeo.2013.12.019*

Gabitov, R.I., Watson, E.B. (2006). Partitioning of strontium between calcite and fluid. *Geochemistry, Geophysics, Geosystems*, **7**(11).

Kim, I.W., Collino, S., Evans, J.S. (2012). Cooperative modulation of mineral growth by prismatic-associated Asprich sequences and Mg(II). *International Journal of Molecular Sciences*, **13**(3), pp. 3949–3958.

Littlewood, J.L., Shaw, S., Peacock, C.L., Bots, P., Trivedi, D., Burke, I.T. (2017). Mechanism of Enhanced Strontium Uptake into Calcite via an Amorphous Calcium Carbonate Crystallization Pathway. *Crystal Growth and Design*, **17**(3), pp. 1214–1223.

Lorens, R.B. (1981). Sr, Cd, Mn and Co distribution coefficients in calcite as a function of calcite precipitation rate. *Geochimica et Cosmochimica Acta*, **45**(4), pp. 553–561.

Markgraf, S., Reeder, R. (1985). High-temperature structure refinements of calcite and magnesite. *Am. Mineral.*, **70**, pp. 590–600.
URL: *http://scholar.google.com/scholar?hl=en&btnG=Search&q=intitle:High-temperature+structure+refinements+of+calcite+and+magnesite#0*

Matsunuma, S., Kagi, H., Komatsu, K., Maruyama, K., Yoshino, T. (2014). Doping incompatible elements into calcite through amorphous calcium carbonate. *Crystal Growth & Design*, **14**(11), pp. 5344–5348.

Mitchell, A.C., Ferris, F.G. (2005). The coprecipitation of Sr into calcite precipitates induced by bacterial ureolysis in artificial groundwater: Temperature and kinetic dependence. *Geochimica et Cosmochimica Acta*, **69**(17), pp. 4199–4210.

Nielsen, L.C., De Yoreo, J.J., DePaolo, D.J. (2013). General model for calcite growth kinetics in the presence of impurity ions. *Geochimica et Cosmochimica Acta*, **115**, pp. 100–114.
URL: *http://dx.doi.org/10.1016/j.gca.2013.04.001*

Paquette, J., Reeder, R.J. (1995). Relationship between surface structure, growth mechanism, and trace element incorporation in calcite. *Geochimica et Cosmochimica Acta*, **59**(4), pp. 735–749.

Ravel, B., Newville, M. (2005). ATHENA, ARTEMIS, HEPHAESTUS: Data analysis for X-ray absorption spectroscopy using IFEFFIT. In *Journal of Synchrotron Radiation*, 4. pp. 537–541.

Rodriguez-Cruz, S., Jockusch, R., Williams, E.R. (1999). Hydration Energies and Structures of Alkaline Earth Metal Ions, M2+ (H2O) n, n= 5-7, M= Mg, Ca, Sr, and Ba. *Journal of the American Chemical Society*, **121**(38), pp. 8898–8906.
URL: *http://www.ncbi.nlm.nih.gov/pubmed/16429612*
http://www.pubmedcentral.nih.gov/articlerender.fcgi?artid=PMC1325212
http://pubs.acs.org/doi/abs/10.1021/ja9911871

Ruiz-Agudo, E., Putnis, C., Rodriguez-Navarro, C., Putnis, A. (2011). Effect of pH on calcite growth at constant ratio and supersaturation. *Geochimica et Cosmochimica Acta*, **75**(1), pp. 284–296.

Stoll, H.M., Klaas, C.M., Probert, I., Encinar, J.R., Garcia Alonso, J.I. (2002). Calcification rate and temperature effects on Sr partitioning in coccoliths of multiple species of coccolithophorids in culture. *Global and Planetary Change*, **34**(3-4), pp. 153–171.

Tang, J., Dietzel, M., Böhm, F., Köhler, S.J., Eisenhauer, A. (2008). Sr2+/Ca2+and44Ca/40Ca fractionation during inorganic calcite formation: II. Ca isotopes. *Geochimica et Cosmochimica Acta*, **72**(15), pp. 3733–3745.

Teng, H.H., Dove, P.M., Orme, C.A., De Yoreo, J.J. (1998). Thermodynamics of Calcite Growth: Baseline for Understanding Biomineral Formation. *Science*, **282**(5389), pp. 724–727.

Tesoriero, A.J., Pankow, J.F. (1996). Solid solution partitioning of Sr2+, Ba2+, and Cd2+ to calcite. *Geochimica et Cosmochimica Acta*, **60**(6), pp. 1053–1063.

Ukrainczyk, M., Greiner, M., Elts, E., Briesen, H. (2015). Simulating preferential sorption of tartrate on prismatic calcite surfaces. *CrystEngComm*, **17**(1), pp. 149–159.
URL: *http://xlink.rsc.org/?DOI=C4CE01447B*

Warren, L.A., Maurice, P.A., Parmar, N., Ferris, G.F. (2001). Microbially mediated calcium carbonate precipitation: Implications for Interpreting calcite precipitation and for solid-phase capture of inorganic contaminants. *Geomicrobiology Journal*, **18**(1), pp. 93–115.

Wasylenki, L.E., Dove, P.M., Wilson, D.S., De Yoreo, J.J. (2005). Nanoscale effects of strontium on calcite growth: An in situ AFM study in the absence of vital effects. *Geochimica et Cosmochimica Acta*, **69**(12), pp. 3017–3027.

Weber, J.N. (1973). Incorporation of stontium into reef coral skeletal carbonates. *Geochim. et Cosmochim. Acta*, **37**(1971), pp. 2173–2190.

Yoreo, J.J.D., Dove, P.M. (2004). Shaping Crystals with Biomolecules. *Science*, **306**(November), pp. 1301–1302.

Chapter 7

Stability of radiolabelled carbonate wastes in cement waste forms

7.1 Summary

The incorporation of Sr bearing calcite into cement was investigated using a cement blend which comprised 50% Ordinary Portland Cement, 40% Blast Furnace Slag, and 10% calcite. It was found that during the cement hydration 5.3 % of the initial calcite dissolved and subsequently incorporated into the cement. It was not possible to track the fate of Sr from the dissolving calcite however it is anticipated to be distributed through the CSH and Ettringite phases, and the ^{14}C is predicted to be distributed in the monocarboaluminate phase. This study indicates that under the conditions studied the majority of calcite incorporated into the cement will be distributed as calcite throughout the matrix, with a minor amount incorporated in cement minerals.

7.2 Introduction

The long term disposal and storage of nuclear waste is an important issue facing the nuclear industry. Radionuclides, particularly those with long half-lives, will remain a hazard millennia into the future; therefore their ultimate disposal must be in a stable waste form.

Cement is commonly used as a material for the immobilization of a range of waste streams. Ordinary Portland Cement (OPC) in particular is widely available, cheap to produce and has a long history of scientific research. It has the added benefit of producing alkalinity, which favours insolubility of many minerals, including carbonates (Glasser, 1997). It may be used to encapsulate solid wastes such as Magnox swarf (Fairhall and Palmer, 1992), preventing direct contact between the solid waste and any waters reaching the repository. Due to the requirement of hydration water in cement production it is possible to directly mix contaminated waters into cement powder; immobilising the contaminant ions by reactions with the cement (Milestone, 2006).

Limestone is commonly used in composite cements acting as both an "inert filler" and an active reactant (Matschei et al., 2007). It is becoming increasingly favoured as a way of reducing the amount of cement required for a given casting and thus reducing CO_2 emissions (Revani and Proske, 2017). While carbonate minerals are insoluble under the high pH conditions produced by OPC, they may continue to react after addition to cement (Milestone, 2006). Contaminant ions either become incorporated into the cement minerals or precipitate as secondary phases. It is important to understand these reactions to determine the long term stability and leaching properties of the final cement

waste forms.

The presence of carbonate ions from the dissolving calcite results in the stabilisation of monocarboaluminate (Mc) over monosulphoaluminate. The aluminium released from this reacts to produce ettringite (Adu-Amankwah et al., 2017; Bonavetti et al., 2001). This ettringite has a larger molar volume than other cement phases and may lead to a reduction in the pore volume of the cement, although it can also generate cracking which may generate fluid flow paths (Matschei et al., 2007). The presence of Limestone in composite cements is also reported to promote Calcium Silicate Hydrate gel (C-S-H) formation (Adu-Amankwah et al., 2017). This increase in early hydration is reported to produce a greater initial strength but weakens the cement in the long term.

Utton et al. (2011) carried out a study into the mixture of $BaCO_3$ containing ^{14}C, produced from THORP re-processing at Sellafield, into a Ground Granulated Blast Furnace Slag (GGBFS) and OPC composite (GGBFS:OPC 9:1). They found that $BaCO_3$ reacted with the SO_4 present in OPC to produce $BaSO_4$, which is less soluble that $BaCO_3$. This process is unlikely to happen with Ca,$SrCO_3$ due to the lower solubility of these phases in their carbonate form relative to their sulphate form. The ^{14}C containing carbonate group was reported to partition into the Mc phase. This Mc phase was likely stabilised by the presence of Ba which scavenges sulphate from the pore solution which may favour the transformation of Mc to ettringite.

This section will test the leaching properties of a OPC/BFS cement after mixing with a ^{14}C labelled Ca,$SrCO_3$. The micro-structure of the resultant waste form will be observed, both before and after leaching, to determine how the Ca,$SrCO_3$ is hosted and if any reactions have taken place.

7.3 Methods

Strontium bearing calcium carbonate was prepared via the methods of (Littlewood et al., 2017), yeilding a Sr composition of 6.52 Wt. % Sr^{2+}. A stock solution with a fixed [Ca], [Sr] and [^{14}C] was prepared and subsequently mixed with Na_2CO_3 to precipitate $Ca_xSr_{1-x}CO_3$. This was allowed to react for 24 h before the crystals were separated via vacuum filtration and rinsing with IPA. The calcite powder was stored in a desiccator prior to mixing into cement grout.

This calcite powder was then blended with Ordinary Portland Cement (OPC) and Ground Granulated Blast Furnace Slag (GGBFS), in the proportions listed in Table 7.1. The OPC contains a small percentage of calcite, therefore the mixing proportions were adjusted to account for this calcite. In the 50-40-10 system 8.75 % of calcite with a Sr Wt.% of 6.52 was mixed with 1.25 Wt.% calcite with a Sr Wt.% of 0. This combined gives 10% calcite with an average 5.71 Wt.%. The Cement was then cast in a CO_2 free environment using 5 mm diameter cylindrical moulds using 20 g of the cement powder blend and 10 g DIW. These blocks were left for 0.5, 1, 7, 12, and 28 days to cure in a CO_2 free environment.

Before analysis the cement was removed from its moulds and crushed using an mortar and pestle to a coarse sand consistency, then washed in IPA for 10 minutes, Ether for 10 minutes before spending 20 minutes on a Hotplate at 50°C to dry. Samples for analysis via EDS were prepared by cutting the cement cylinder using a low speed isomet and then mounting in resin before polishing with silicon carbide paper and a water free diamond paste to achieve a flat surface.

Thermo-Gravimetric Analysis (TGA) was carried out on ground and hydration stopped samples to determine which phases were present based on their thermal decomposition temperatures. This was supplemented by XRD analysis on both dried and un-dried samples using a Bruker D2 XRD. SEM/EDS analysis was carried out using a Tescan VEGA3 XM, equipped with X-max 150 silicon drift detector EDS and Aztec 3.3 data acquisition software on dried and polished samples from the 28 d end point to determine both which phases were present and the distribution of Sr amongst them.

Table 7.1: Cement blends used for the encapsulation experiments

%	50-40-10	70:20:10	20:70:10
OPC	52.35	70.64	19.98
GGBFS	38.90	20.52	70.37
Calcite	8.75	8.84	9.65

7.4 Results

Thermogravimetric Analysis (TGA) data presented in Table 7.2 indicates the mass loss due to the thermal decomposition of $CaCO_3$ to CaO and CO_2 which has been converted to the % of calcite which dissolved during cement hydration. In the 50-40-10 experiment a progressive dissolution starting at 27.9 % after 12 hours and increasing to a maximum of 55.6 % after 28 days. In the experiment which contained a greater proportion of GGBFS (20-70-10) less calcite was dissolved (17.5 %) conversely in the higher OPC experiment (70-20-10) more calcite was dissolved (77.4 %).

The bulk concentration of Sr distributed amongst the cement phases was calculated

Table 7.2. For the each experiment this was based on the dilution of the dissolving calcite with an average Wt.% Sr of 5.71 in a final 30 g cement waste form.

Table 7.2: TGA time series displaying progressive decrease in the amount of $CaCO_3$ in the cement with curing time for the 50-40-10 system. Data from the 20-70-10 and 70-20-10 28d end points are included.

Blend composition	Time (days)	% $CaCO_3$	% Dissolved	Bulk Wt. % Sr
50-40-10	0.5	7.21	27.9	0.15
	7	4.67	53.3	0.28
	28	4.44	55.6	0.29
20-70-10	28	1.75	17.5	0.09
70-20-10	28	7.74	77.4	0.41

The Al/Ca and Si/Ca ratios of the 28 day aged 50-40-10 cement blend, determined by SEM-EDS, are plotted in figure 7.1. These are characteristic of limestone blended cements (Adu-Amankwah et al., 2017), with most analyses plotting between ettringite and Calcium Silicate Hydrate (CSH) end members. Several samples which appear to deviate from this trend line, instead plotting between Calcium Hydroxide (CH) and the CSH characterised by lower Al and Si. The only samples which returned any Sr plot in this area (plotted as black circles) are the only analyses which returned any Sr, suggesting that Sr is hosted in either as hydroxides or $CaCO_3$. Further analysis of the Sr bearing samples, based on their composition and morphology, suggest that they are the initial calcite added.

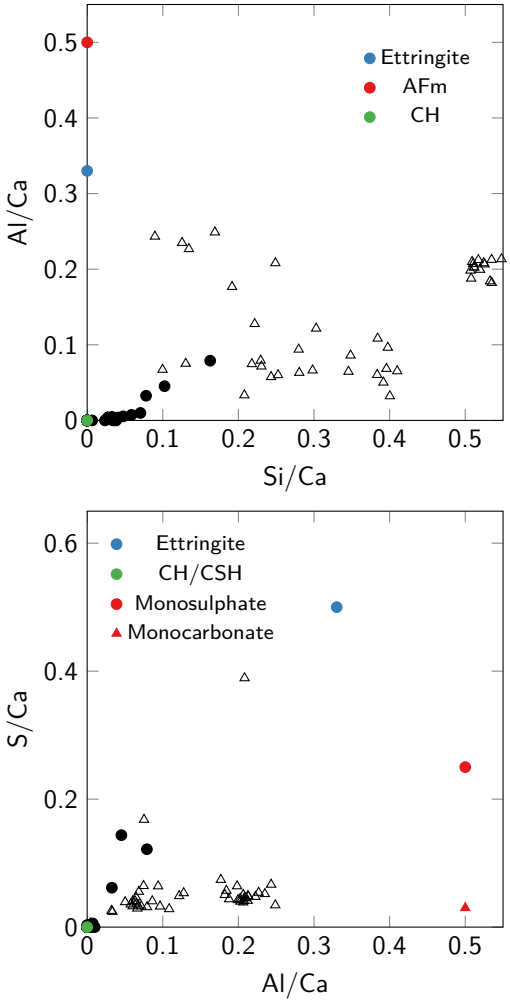

Figure 7.1: Elemental ratios determined by EDS spot analysis plotted alongside key cement end members. Analyses which returned Sr concentrations above LOD are plotted as black circles.

Mapping data is presented in SI Figure D.2. This is somewhat inconclusive due to the low concentration of Sr present in the sample however, spot analysis indicates discrete particles with a Sr Wt. % of 6.75 $\pm$ 0.61 figure 7.2 which, based on their composition most likely indicate the calcite initially added to the system.

XRD data carried out on non-hydrated sample is presented in figure 7.3. This displays ingrowth of Mc from 0.5-28 days. The ettringite peak displays a similar intensity throughout the experiment, indicating its formed early during cement hydration and that it is stable.

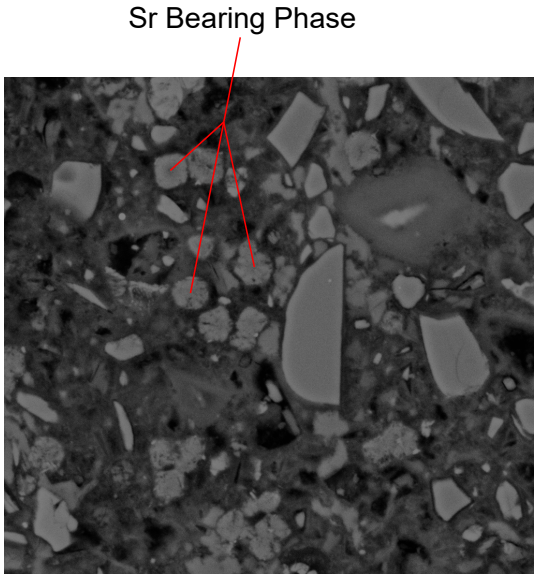

Figure 7.2: Illustration of the morphology which returned Sr Wt.% 6.75 $\pm$ 0.61

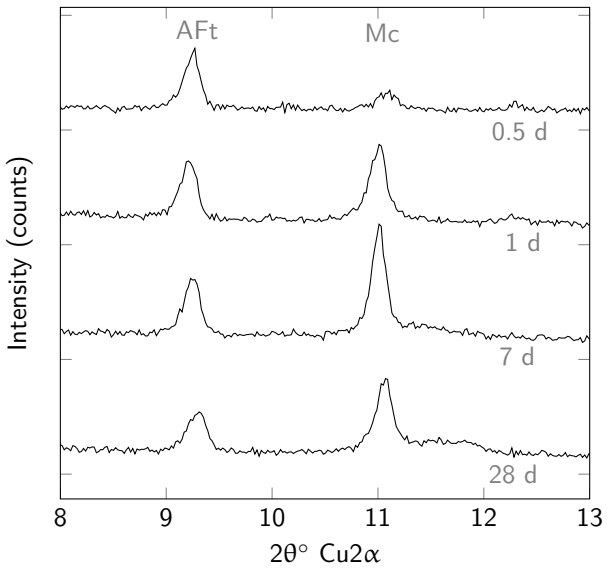

Figure 7.3: XRD data for 3 time points in the 50-40-10 cement blend cured system, displaying the AFt (Ettringite) peak and Mc (Monocarboaluminate) peak.

7.5 Discussion

Sr Distribution

No significant accumulation of Sr in a phase other than the initial $CaCO_3$ was clearly identified. It is possible that Sr is compatible with all cement phases, in the 50-40-10 experiment this would result in a diffuse incorporation across the sample of approximately 0.29 Wt. %, which is likely lower than the limits of detection for EDS. This is supported by the literature as previous authors have suggested the incorporation of Sr into a range of cement phases is viable. These phases include Ettringite (Gougar et al., 1996), C-S-H and 9 Å-Tobermorite (Youssef et al., 2014). While these phases are likely to have varying affinities for the Sr^{2+} ion if the Sr concentration is low and spread diffusely though the sample these subtleties may be below the limit of detection and subsequently lost.

C Distribution

Monocarboaluminate was present in these cement blends and, due to the lack of CO_2 in-gassing, the carbonate in this phase is likely derived from the carbonate added to our experiment. Had this carbonate contained radioactive ^{14}C it is likely that it too would have been transformed to Mc. This is supported by (Utton et al., 2011) who found that ^{14}C from $Ba^{14}CO_3$ was transformed into Mc.

Effect of Cement composition

The cement composition has a significant impact on the dissolution of calcite and therefore the bulk Sr concentration amongst the nascent cement phases. Cements with greater concentrations of OPC displayed greater dissolution of the initial calcite added, up to 77.4 % in the system comprising 70 % OPC. The cause of this is unclear without further mineralogical analysis to determine which mineral phases were driving the dissolution of calcite. However, this suggests that the use of high GGBFS cement would produce a waste form with a lower amount of discrete calcite particles and therefore minimise hotspots of Sr within the cement. Whether the actual activity of these hotspots is enough to cause a criticality hazard if clumping of the calcite particles occurs would need further assessment.

Any dissolution of Ca and Sr bearing material from the cement grout is likely to be precipitated as calcium carbonate due to the predicted high pH of the groundwater (based on cement buffering). An understanding of the groundwater chemistry i.e. whether it is Ca or CO_3 dominated would be useful in determining the potential incorporation of ^{90}Sr or ^{14}C into this phase. The precipitation of calcite may fill pore spaces and fractures in the waste form which would reduce permeability and minimise further dissolution.

7.6 Conclusions

From this work the final fate of Sr incorporated into the cement grouts remains somewhat unclear as EDS analysis only returned positive Sr results for phase assemblages comprising $CaCO_3$. Future work may seek to use a different analytical technique, such

as microfocus XRF performed using a synchrotron source, to allow for detection of the dissolving Sr. However, in the cement compositions used in this study a range of radio-calcite dissolution was achieved (17.5-77.4 %), which suggests that the cement composition is likely to be an important factor from a waste disposal standpoint. Based on this information an experiment could be designed to study the leaching properties of a cement waste form with the Sr mostly in a carbonate phase relative to one with Sr mostly in a cement phase. However, based on a high pH cement buffered repository and due to the physical separation of the calcite from groundwater by the cement matrix, calcium carbonate minerals are likely to have a low solubility.

Based on the observed presence of Mc in both XRD and elemental cross plots, coupled with the findings of Utton et al. (2011) which suggest ^{14}C is stable within this phase, it is likely that any ^{14}C dissolving from the radioactive calcite will be partitioned into this phase.

Bibliography

Adu-Amankwah, S., Zajac, M., Stabler, C., Lothenbach, B., Black, L. (2017). Influence of limestone and anhydrite on the hydration of Portland cements. *Cement and Concrete Research*, pp. 96–109.
URL: *http://dx.doi.org/10.1016/j.cemconres.2017.05.013*

Bonavetti, V.L., Rahhal, V.F., Irassar, E.F. (2001). Studies on the carboaluminate formation in limestone filler-blended cements. *Cement and Concrete Research*, **31**(6), pp. 853–859.

Fairhall, G.A., Palmer, J.D. (1992). The encapsulation of Magnox Swarf in cement in the United Kingdom. *Cement and Concrete Research*, **22**(2-3), pp. 293–298.

Glasser, F.P. (1997). Fundamental aspects of cement solidification and stabilisation. *Journal of Hazardous Materials*, **52**(2-3), pp. 151–170.

Gougar, M.L.D., Scheetz, B.E., Roy, D.M. (1996). Ettringite and C-S-H portland cement phases for waste ion immobilization: A review. *Waste Management*, **16**(4), pp. 295–303.

Littlewood, J.L., Shaw, S., Peacock, C.L., Bots, P., Trivedi, D., Burke, I.T. (2017). Mechanism of Enhanced Strontium Uptake into Calcite via an Amorphous Calcium Carbonate Crystallization Pathway. *Crystal Growth and Design*, **17**(3), pp. 1214–1223.

Matschei, T., Lothenbach, B., Glasser, F.P. (2007). The role of calcium carbonate in cement hydration. *Cement and Concrete Research*, **37**(4), pp. 551–558.

Milestone, N.B. (2006). Reactions in cement encapsulated nuclear wastes: need for toolbox of different cement types. *Advances in Applied Ceramics*, **105**(1), pp. 13–20.

Revani, M., Proske, T. (2017). Influence of chemical-mineralogical properties of limestone on the shrinkage behaviour of cement paste and concrete made of limestone-rich cements. *Construction and Building Materials*, **157**, pp. 818–828.
URL: *https://doi.org/10.1016/j.conbuildmat.2017.09.101*

Utton, C.A., Gallucci, E., Hill, J., Milestone, N.B. (2011). Interaction between BaCO3 and OPC/BFS composite cements at 20 °c and 60 °c. *Cement and Concrete Research*, **41**(3), pp. 236–243.

Youssef, M., Pellenq, R.J., Yildiz, B. (2014). Docking 90Sr radionuclide in cement: An atomistic modeling study. *Physics and Chemistry of the Earth*, **70-71**, pp. 39–44.
URL: *http://dx.doi.org/10.1016/j.pce.2013.11.007*

Part IV

Conclusions

Chapter 8

Conclusions

This project's goal was to expand the knowledge of Sr and ^{14}C coprecipitation into calcium carbonate to aid in the design of a remediation process. This section will aim to extrapolate the key learnings of this project with respect to potential remediation strategies.

^{14}C removal

Carbon-14 removal was observed at a maximum of 99.9 % after 50 minutes in an experiment comprising 10 mM $Ca(OH)_2$ and 1 mM Na_2CO_3 and 2 m^2 L^{-1} rhombic seed crystals (Section 5), however similar removals were obtained for all systems where an excess of Ca was present with respect to TIC. This is due to the Ca^{2+} ions in solution readily reacting with the $^{14}CO_3^{2-}$ ions to form calcite; this reaction is favoured by seed crystals as these lower the effective supersaturation required for precipitation.

After its initial removal ^{14}C displayed a remobilisation back to solution, indicating

that its encapsulation in calcite is metastable. This remobilisation was only significant after TIC began to accumulate in the solution and there was no longer a net CO_2 flux to the precipitate. It is likely caused by a shift in the stable calcite morpholgy, from scalenohedral in high Ca:CO_3 solutions to rhombohedral in low Ca:CO_3 solution, and exacerbated by an associated decrease in pH caused by CO_2 in-gassing which increases the solubility of $CaCO_3$.

^{90}Sr removal

Strontium was removed to below the limits of quantification for ICP-OES (2.9 ppb) in experiments where there was an an excess of Na_2CO_3 relative to $Ca(OH)_2$ and abundant calcite seed crystals (Section 5). The presence of calcite seed crystals had a significant impact on the removal of Sr, increasing it from 98.2% in experiments prepared by dialysis filtration (i.e. in the absence of seed crystals) to over 99.9% in experiments with 2 m^2 L^{-1} of rhombic seed crystals. This is most likely due to the seed crystals lowering the effective supersaturations of both calcite and strontianite as well as the adsorption of Sr to the seed crystal surfaces (which become negative at high pH).

Strontium-90 incorporation into calcite was demonstrated to operate across a range of Sr concentrations with a linear distribution coefficient (Section 6). In some systems an increase in the D_{Sr} was observed towards the end of the experiment. Modelling supports the idea that this is caused by the accumulation of TIC from CO_2 in-gassing which generates a supersaturation of strontianite. Under the conditions anticipated at Sellafield, with groundwater Sr concentrations of 1.4 μM whereas previous experiments were carried out using 140 μM. This means a supersaturation of strontianite will require

greater concentration of TIC in the solution to achieve and is unlikely to occur in the Sellafield groundwater.

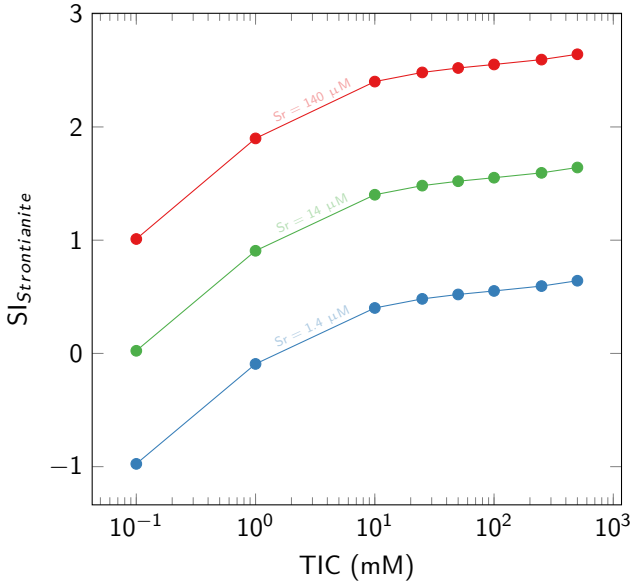

Figure 8.1: Strontianite supersaturation as a function of pH plotted for 3 Sr concentrations (140, 14, 1.4 μM).

The importance of Ionic content

Increased ionic strength may inhibit this technique due to the complexing of ^{90}Sr (and $^{14}CO_3^{2-}$) by solution ions. This suppresses the supersaturation of strontianite which has been shown to be important for the removal of Sr by this technique.

The precipitation of Sr and ^{14}C into calcite was the main focus of this investigation however aragonite (a polymorph of calcite with larger M^{2+} sites) was also investigated. Incorporation of Sr into this morphology is reported to be more favourable than into calcite however this study found it difficult to consistently obtain aragonite at high pH. However if the groundwater is at a circumneutral pH aragonite precipitation may be accessible and thus improve the D_{Sr}.

Understanding the strontianite-calcite solid solution

The Calcite-Strontianite solid solution was found to exist across a broad range of solution compositions i.e. as the as the amount of Sr in the solution increased relative to calcium the proportions in the precipitate increased correspondingly. This solid solution only stopped after strontianite because supersaturated, however calcite with a high degree of Sr^{2+} displayed an increasing lattice disorder.

The stability of radio-carbonate powders in cement waste forms

During mixing into cement a significant proportion of radio-carbonate has been showed to dissolve to form new phases. However, problems were encountered tracking the fate of the contaminants amongst these phases, but based on previous literature it is likely that ^{14}C will partition into monocarboaluminte and ^{90}Sr will be distributed across ettringite, CSH and tobermorite. Further work would have to be carried out to understand if any preferential incorporation exists. The portion of radio-carbonate that remains un-dissolved is likely to remain stable, due to its physical isolation in the cement matrix and its insolubility in the high pH conditions predicted in a cement buffered repository.

8.1 Potential treatment schemes

8.1.1 Batch

Data from batch experiments run for ^{14}C and Sr removal are contained in sections 4 and 5. These experiments were able to achieve effective removal of both Sr and ^{14}C by 99.99% and 99.7% respectively. However, since the Sr and ^{14}C removal did not occur at the same time it is unlikely that a simple batch reactor (Figure 8.2) would be able to achieve simultaneous removal of these two isotopes.

It may however be possible to use a solution with a TIC excess to effectively remove over 99.99% of ^{90}Sr (along with calcium) followed with a polishing stage comprising of an ion exchange media to remove ^{14}C.

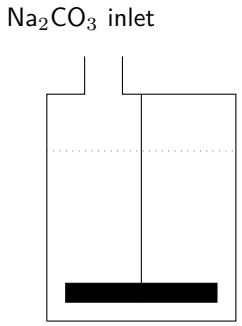

Figure 8.2: Schematic of a Batch treatment process

8.1.2 Continuous flow

Due to the differing removal environments of ^{90}Sr and ^{14}C for this treatment to operate as a continuous flow system it is necessary to separate the ^{90}Sr and ^{14}C removal stages. This can be achieved by running this as a two stage treatment, with one stage comprising

a solution with an excess of TIC and the other and excess of Ca.

Filtration

A continuous flow treatment scheme would have the potential benefit of allowing treatment of groundwater at the rate of pumping, rather than intermittent pumping and treating. However it is unclear how a continuous pumping regime would affect the contaminant profile in the groundwater, as previous work has shown that this may result in increased adsorption of groundwater ions to soil minerals.

Due to the different timings and conditions required for ^{90}Sr and ^{14}C removal these contaminants would have to form separate waste streams in a continuous flow treatment scheme. This could be beneficial as it would allow for separate treatment of the two waste streams which would have significantly different half-lives and ionizing energy.

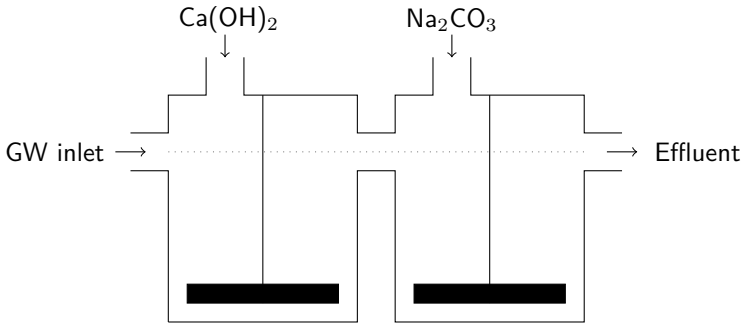

Figure 8.3: Schematic of a continuous flow treatment process

Gas separation

At pH<9 ^{14}C will speciate as $^{14}CO_2$. Therefore if a tank of groundwater is buffered to pH 8 with HCl and allowed sufficient time to equilibrate with the head-space ^{14}C will

be removed from solution as $^{14}CO_2$. This $^{14}CO_2$ may be carried to a second tank filled with a saturated $Ca(OH)_2$ solution. The high pH will force dissolution of the $^{14}CO_2$ and the excess Ca will precipitated the ^{14}C as calcium carbonate. The initial solution, now containing only ^{90}Sr will pass to a second tank where a high TIC concentration can be used to favour Sr removal by carbonate precipitation.

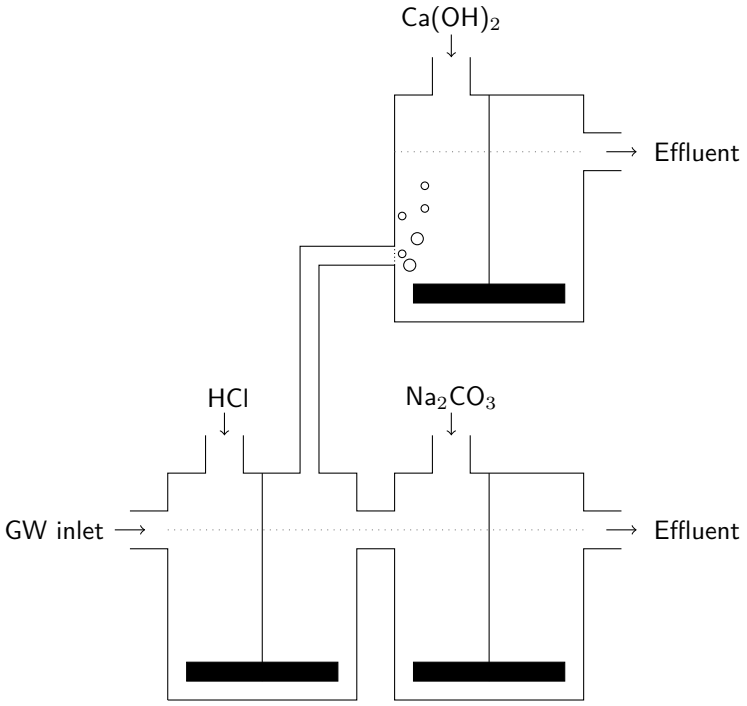

Figure 8.4: Schematic of a continuous flow treatment process

Final Remarks

This research has demonstrated that while there exist a number of complicating factors, the coprecipitation of ^{90}Sr and ^{14}C into calcite is a potentially viable method for the removal of these two isotopes from groundwater. It may be used either to lower the ionic content and reduce the radionuclide profile before a final ion exchange step, or a more complex scheme may be developed that could achieve a more significant

removal. Due to the complexities presented by the carbonate precipitation scheme careful consideration and modelling of site specific conditions will be required prior to any application.

Appendices

Appendix A

Supplementary information Chapter 4: Coprecipitation of ^{14}C and Sr with carbonate precipitates: The importance of reaction kinetics and recrystallization pathways

S.I. Section 1: Full PHREEQC input script

The following script was designed to model the simultaneous dissolution of $Ca(OH)_2$, in-gassing of CO_2 and precipitation of $CaCO_3$. Comment have been included within the script to include readability.

```
RATES
Calcite
# Nancollas and Reddy Calcite precipitation rate
-start
10 si_ cc = si("Calcite")
20 if (m <= 0 and si_ cc < 0) then goto 200
30 rate = 0.576 * 118.2 * 5.4 * (3.6e-9 - act("Ca+2") *
act("CO3-2"))
80 moles = rate * time
```

```
140 if (moles > m) then moles = m
150 if (moles >= 0) then goto 200
160 temp = tot("Ca")
170 mc = tot("C(4)")
180 if mc < temp then temp = mc
190 if -moles > temp then moles = -temp
200 save moles
-end
# Johannsen 1999 Ca(OH)2 dissolution rate
Ca(OH)2
-start
1 si_ caoh = si("Ca(OH)2")
20 if (m <= 0 and si_ caoh < 0) then goto 200
30 SA = 4.5 * m/m0
100 rate = 2.1 * SA * (4.76e-6 - act("Ca+2") *
act("OH-")^2)
110 moles = rate * time
200 SAVE moles
-end
# Empirical Linear CO2 in-gassing rate
CO2(g)
-start
1 si_ co2 = si("CO2(g)")
2 PCO2 = 7.2e-5 # 1/6 atm
3 CO2eq = PCO2 * 0.032
4 SA = 56 # cm2
20 if (m <= 0 and si_ co2 < -3.4) then goto 200
25 rate = 5.4e-4 * CO2eq - 5.4e-4 * (MOL("H2CO3")/10)
26 rate = rate * SA
30 moles = rate * TIME
200 SAVE moles
-end
INCREMENTAL_ REACTIONS TRUE
#Starting solution 1 L
#0.01M NaOH, 1ppm SrCl2 & 1mmol Na2CO3
solution 1
temp 20.0
pH 12.2
water 1 kg
units mmol/L
Na 3 charge
C(4) 1
Sr 0.114
Cl 0.228
KINETICS
CO2(g)
-m0 1
```

```
Ca(OH)2
-m0 0.00918
Calcite
-m0 0
-parms 50 0.6
-cvode TRUE
 # -steps 259200 in 432 steps
 # -steps 3000 in 100 steps
 # -steps 0.5 1.5 8 50 360 1440 2880 4320 minutes
-steps 0.5 1 6.5 42 310 1080 1440 1440 7680 minutes
SELECTED_ OUTPUT
-file Complete Solution.xls
-reset false
USER_ PUNCH
-headings t pH Ca(mmol) Na(mmol) TIC SrC/C0 nCalcite
14C/C0
-start
10 PUNCH total_ time/60/60
20 PUNCH -LA("H+")
30 PUNCH TOT("Ca")*1000
40 PUNCH TOT("Na")*1000
50 PUNCH TOT("C(4)")*1000
60 PUNCH 1-((KIN("Calcite")*1000)*0.00108/0.0114)
70 PUNCH KIN("Calcite")
80 PUNCH act("CO2")*1000
-end
USER_ GRAPH 1
-axis_ scale x_ axis 0.001 auto auto auto logscale
-axis_ scale y_ axis auto
-axis_ titles "time (h)" "[Ca] (mmol)"
-initial_ solutions false
-connect_ simulations true
-start
10 GRAPH_ X total_ time/3600
20 GRAPH_ Y TOT("Ca")*1000
USER_ GRAPH 2
-axis_ scale x_ axis 0.001 auto auto auto logscale
-axis_ scale y_ axis auto
-axis_ titles "time (h)" "pH"
-initial_ solutions false
-connect_ simulations true
-start
10 GRAPH_ X total_ time/3600
20 GRAPH_ Y -LA("H+")
END
```

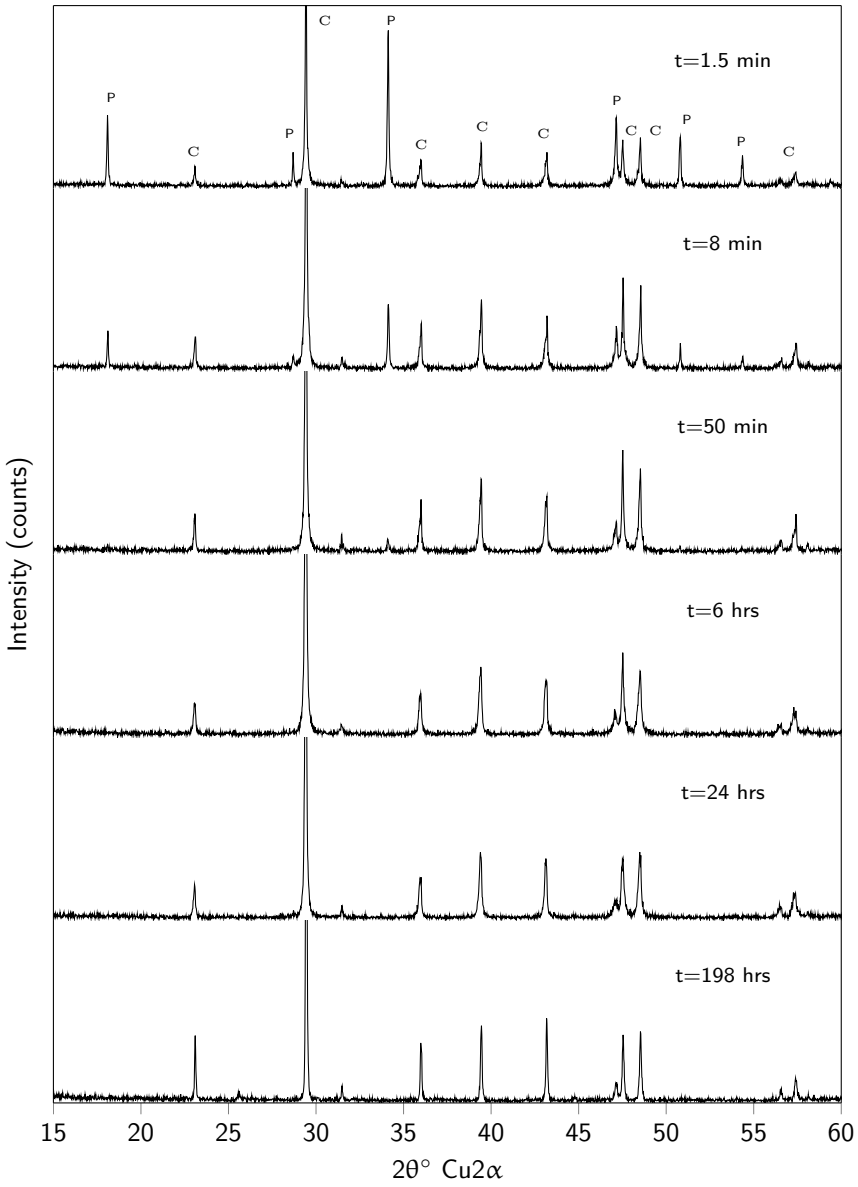

Figure A.1: Stacked XRD traces displaying key mineral phases throughout the [Ca]10:[CO_3]1 experiment (C=Calcite, P=Portlandite)

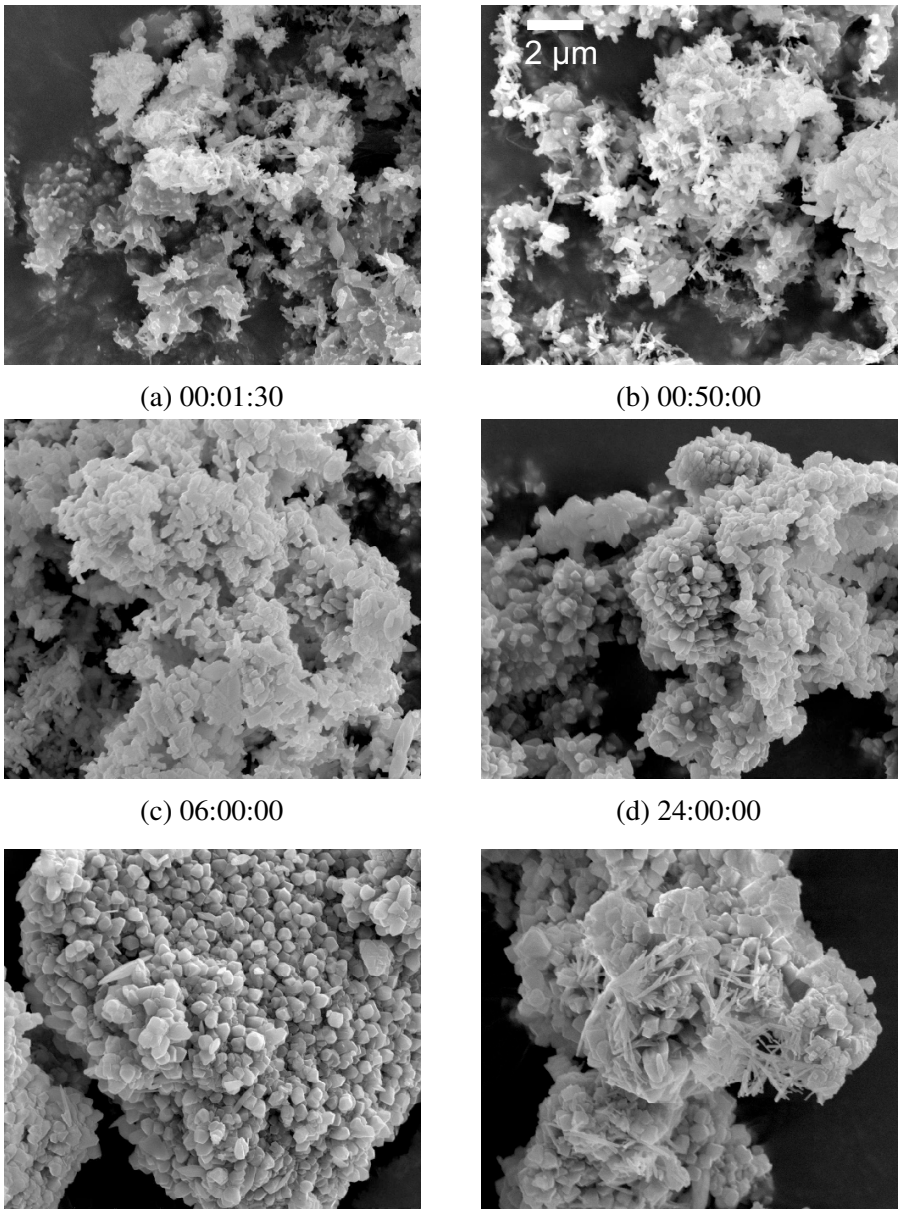

(a) 00:01:30 (b) 00:50:00

(c) 06:00:00 (d) 24:00:00

(e) 48:00:00 (f) 190:00:00

Figure A.2: SEM micrographs from the [Ca]10:[CO_3^{2-}]1 experiment from time intervals between 00:01:30-190h

Appendix B

Supplementary information Chapter 5: Sequestering ^{14}C and Sr into calcium carbonate: The role of pH, Temperature and Sulphate on carbonate polymorphism

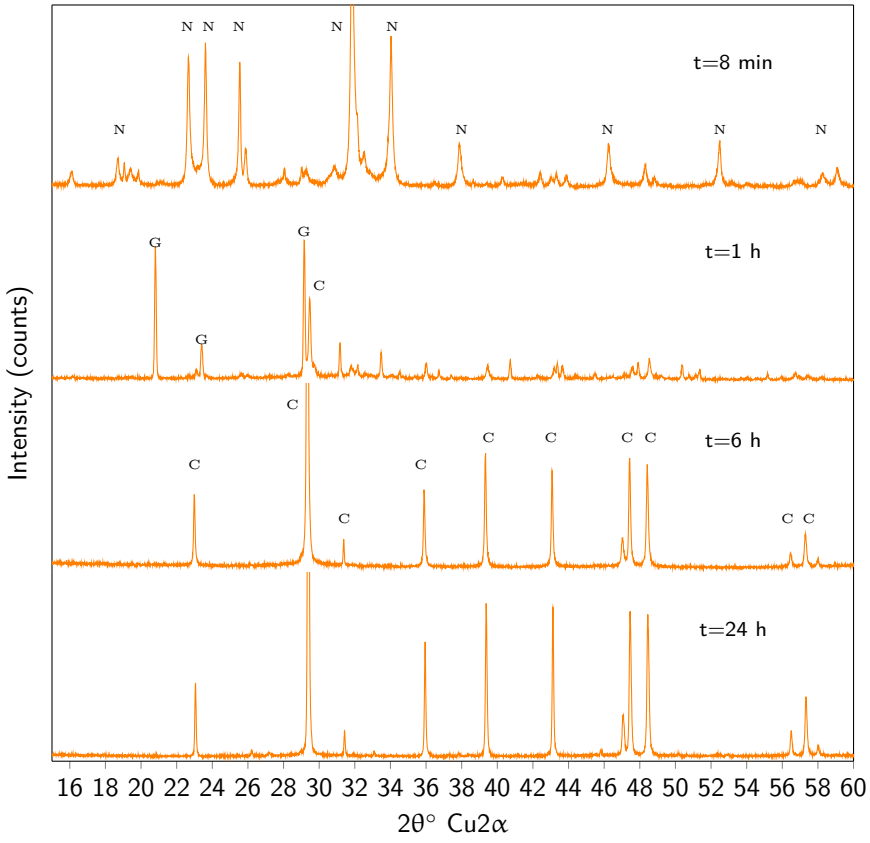

Figure B.1: XRD data from the 50 mM Na_2SO_4 system. N=Na_2SO_4 G=Gypsum C=Calcite

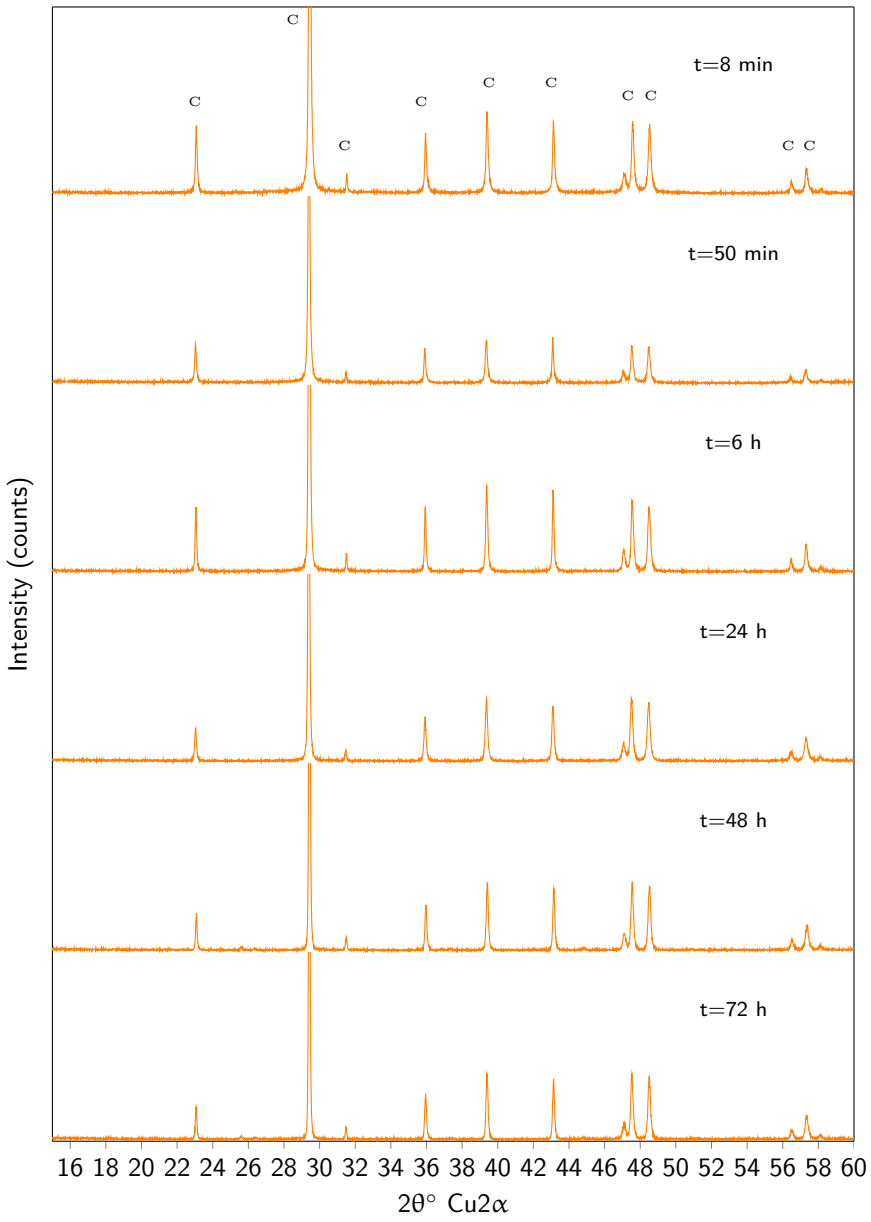

Figure B.2: XRD data from the 40 °C system

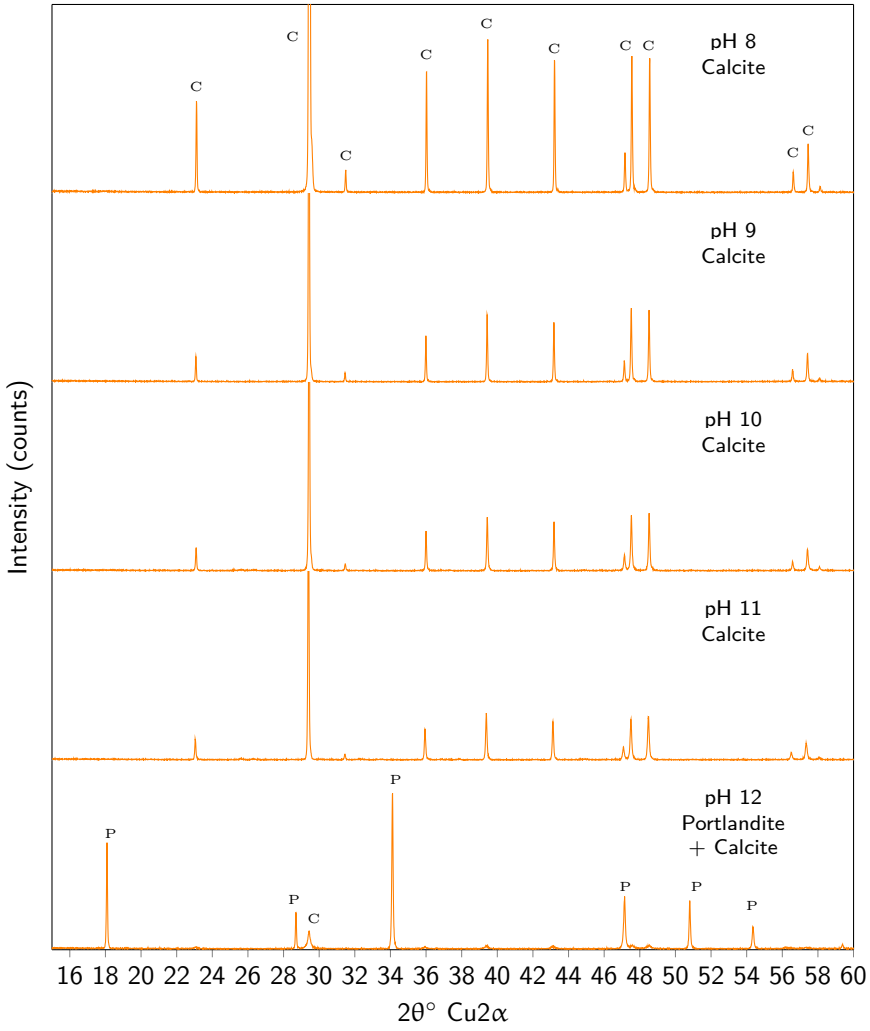

Figure B.3: XRD data from the auto titration experiments using 50 mM Na_2SO_4 from pH 9-12

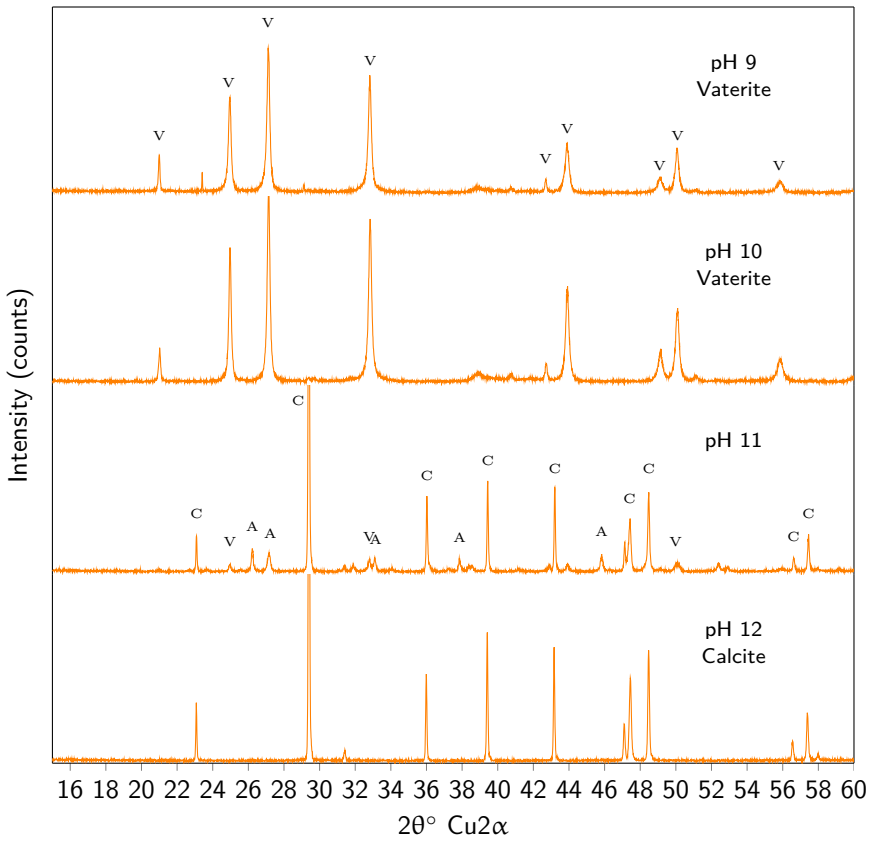

Figure B.4: XRD data from the auto titration experiments using 50 mM Na_2SO_4 from pH 9-12

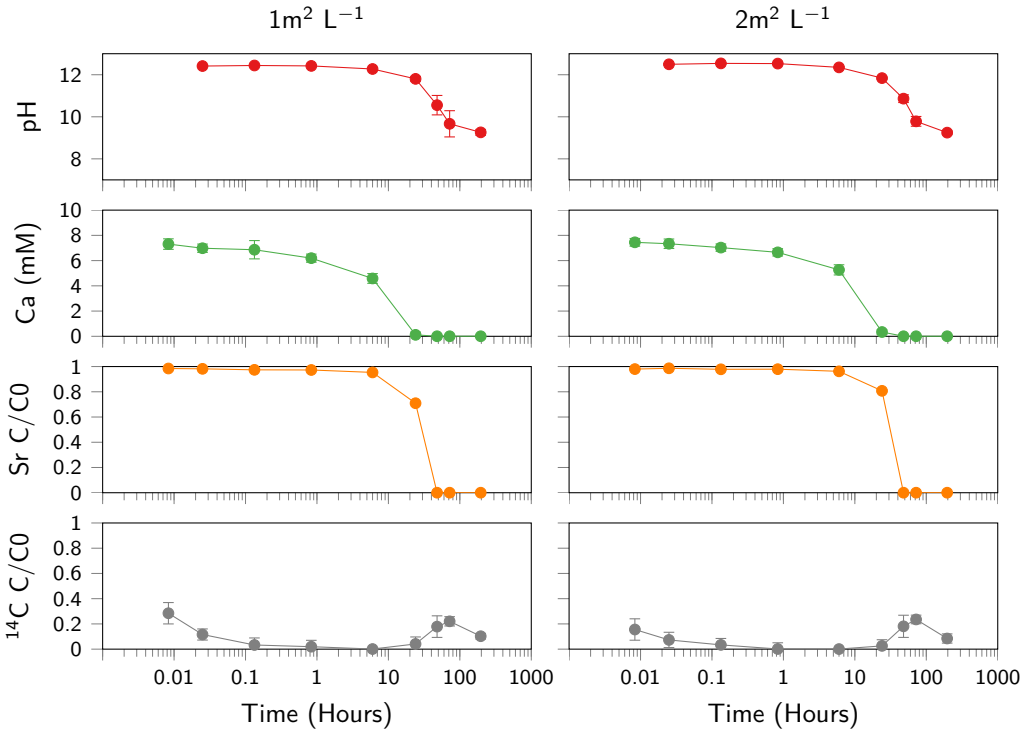

Figure B.5: Complied data from the 1 and 2 m^2 L^{-2} experiments

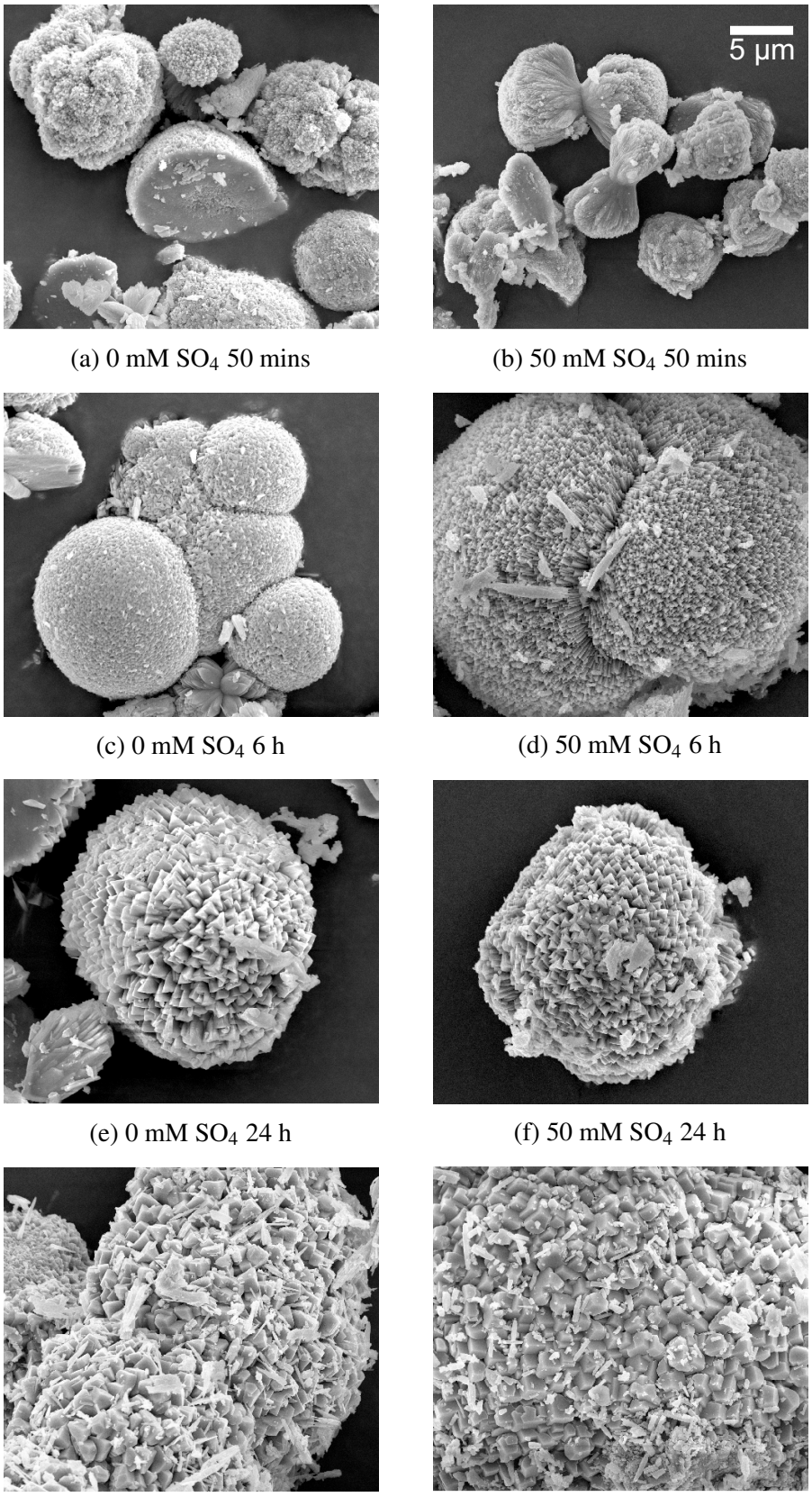

(a) 0 mM SO_4 50 mins

(b) 50 mM SO_4 50 mins

(c) 0 mM SO_4 6 h

(d) 50 mM SO_4 6 h

(e) 0 mM SO_4 24 h

(f) 50 mM SO_4 24 h

(g) 0 mM SO_4 72 h

(h) 50 mM SO_4 72 h

Figure B.6: A comparison of SEM images taken from the 50 mM SO_4 experiments (left) and the 0 mM SO_4 experiment (right)

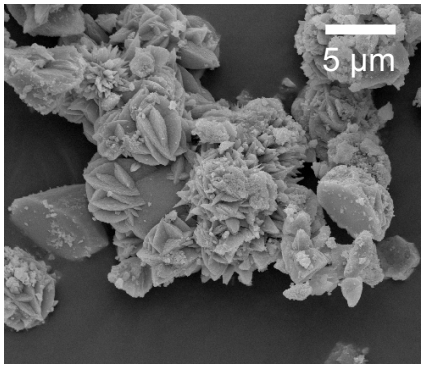

(a) 50 mM pH 9

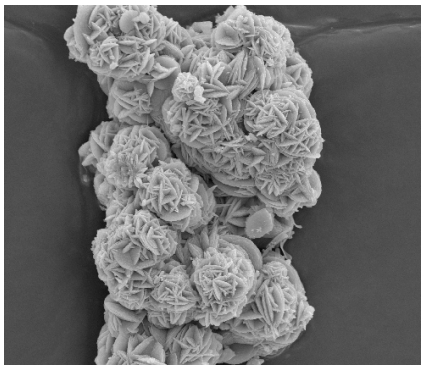

(b) 50 mM pH 10

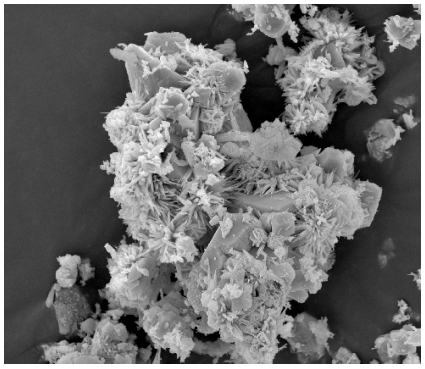

(c) 50 mM pH 11

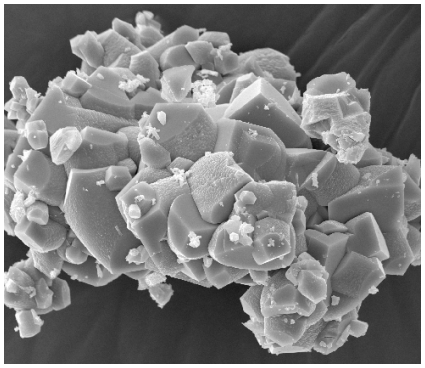

(d) 50 mM pH 12

Figure B.7: The role of pH on carbonate polymorphism in the 50 mM SO_4 systems. 5 μm scale bar (image a) valid for all images.

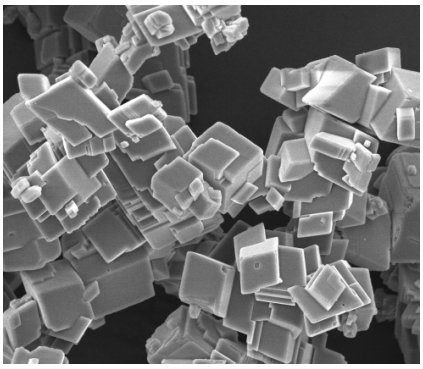

(a) Sigma Aldrich $CaCO_3$ seed crystals

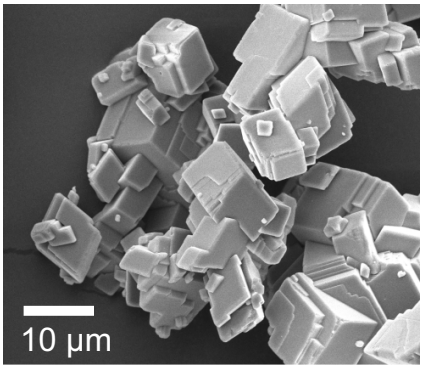

(b) 1 m^2 L^{-1} seeded experiment 8 mins

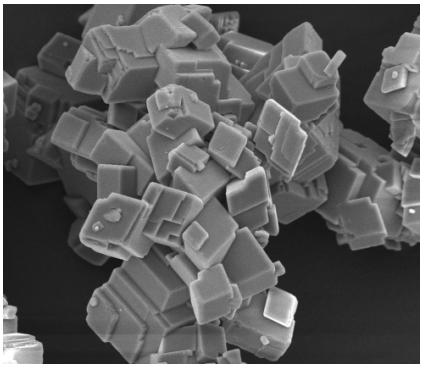

(c) 1 m^2 L^{-1} seeded experiment 50 mins

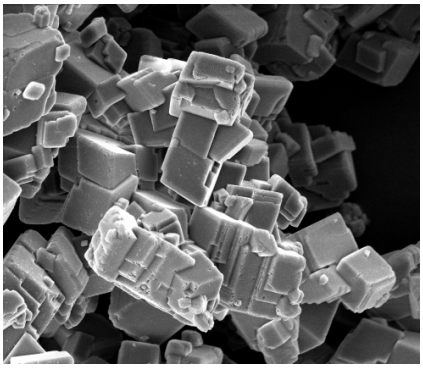

(d) 1 m^2 L^{-1} seeded experiment 24 h

Figure B.8: A comparison of SEM images taken from the seeded experiments, using 0.484 g of Sigma Aldrich $CaCO_3$ to achieve a 1 m^2 L^{-1} surface area.

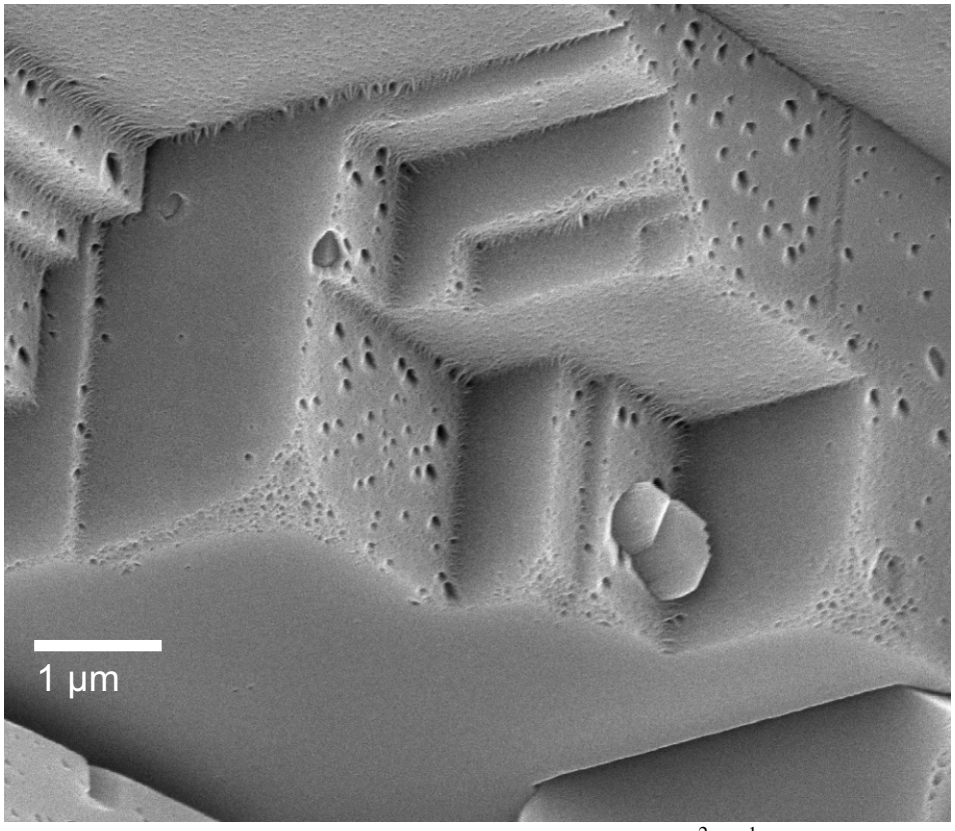

Figure B.9: Surface pitting of a calcite rhomb after 24 h in the 1 m^2 L^{-1} seeded experiment

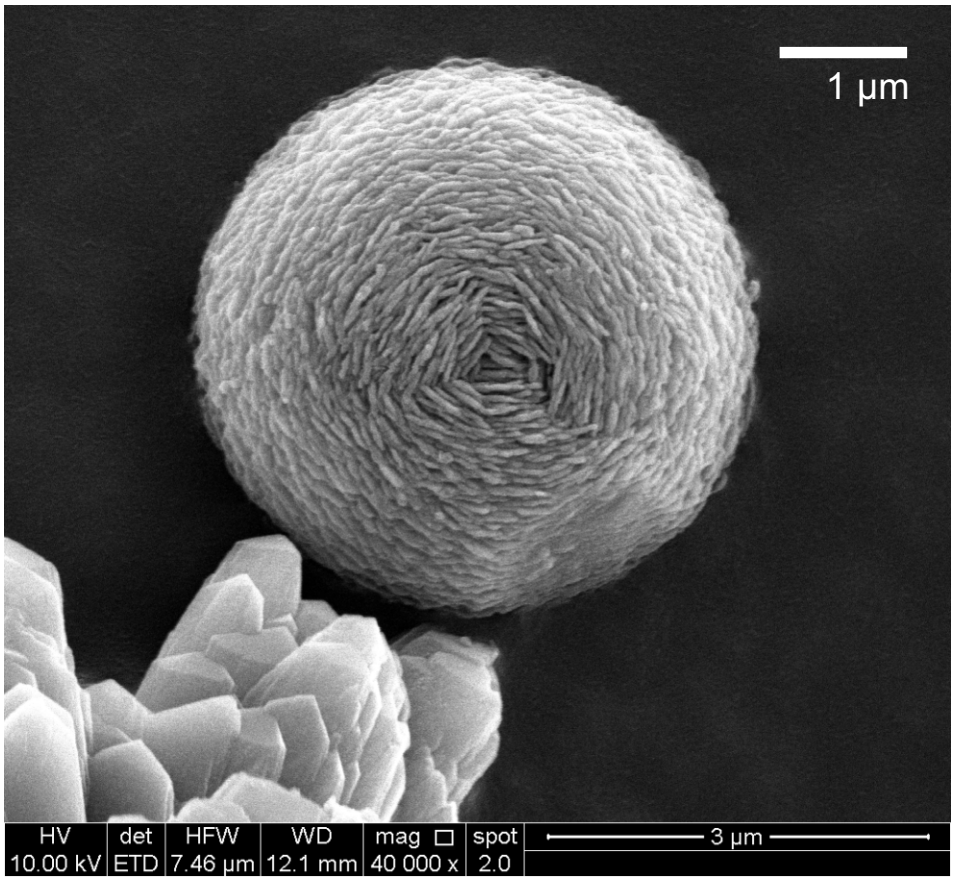

Figure B.10: Vaterite ball observed after 6 h in the 40 °C experiment

Appendix C

S.I. for Section 6: Enhanced Crystallographic incorporation of Strontium(II) ions to Calcite via Preferential Adsorption at Obtuse Sites during Spiral Growth

S.I. Section 1 - XRD Carbonate Polymorphism

Initial constant composition experiments were carried out in a continuous tank stirred reactor fed by a $Ca(OH)_2/SrCl_2$ solution (in which the Sr:Ca ratio varied from 0-0.48) and a 50 mM Na_2CO_3 solution. This achieved a constant composition environment in which the Sr/Ca ratio varied, enabling observations to be made on the role of solution Sr/Ca on Sr incorporation into calcite. Reactions were carried out in a 150 mL reaction vessel in the absence of initial seed crystals.

Data compiled in SI Table 1 show a significant variation in the polymorphism of the

Table C.1: XRD data from the unseeded CTSR experiments

Sample #	[Ca] (mM)	[Sr] (mM)	Sr/Ca $\times 10^2$	Calcite %	Aragonite %	Strontianite %
2	15	0	0	98.67	1.33	0
8	10	0	0	81.29	18.71	0
9	10	0	0	12.40	87.6	0
13	14.9	0.1	0.01	73.39	26.61	0
3	9..9	0.1	0.01	93.39	6.37	0.24
14	14.5	0.5	0.03	98.53	1.44	0.03
4	9.5	0.5	0.05	100	0	0
17	12	3	0.25	97.23	1.98	0.79
6	8	2	0.25	98.85	0.51	0.64
7	6.3	3	0.48	24.87	26.1	49.03
12	9.5	0.5	0.05	-	-	-
15	14	1	0.09	-	-	-
5	9	1	0.11	-	-	-
16	13	2	0.15	-	-	-
18	7.5	2.5	0.33	-	-	-

carbonate forming. At high Sr:Ca (0.48) strontianite becomes the main phase however below this value a mixture of calcite and aragonite was present, the proportions of which show no systematic variation. A potential explanation for this is that both calcite and aragonite have similar solubility products (3.39×10^{-9}) and (4.57×10^{-9}) respectively. Due to these similar supersaturations, and the lack of seed crystals, the polymorph distribution will be dependent of the first phases nucleated in solution. If a significant proportion of the early-formed crystals are of the aragonite polymorph then this will act as a seed crystal allowing a significant proportion of aragonite to form. Due to calcites slightly higher supersaturation this is the most common phase to nucleate which is represented by the skew of the data towards calcite.

Experiments were repeated with rhombohedral calcite seed crystals to guide the crystallization pathways. This was successful at producing a 100% Calcite precipitate in most experiments however XRD data was collected on a Bruker D8 XRD with a Cu

Table C.2: Identification of carbonate polymorph via XRD for selected samples from the unseeded constant composition experiments. C=Calcite, S=Strontianite.

#	Sr/Ca_{sol}	Sr/Ca_{ppt}	Wt. % Sr	D_{Sr}	XRD	$SI_{calcite}$	$SI_{strontianite}$
50	0	0	0.02	0.1	C	1.26	-0.43
65	0.01	0	0.11	0.11		1.07	0.09
58	0.03	0	0.32	0.11		1.3	0.76
60	0.39	0.04	3.56	0.11		1.21	1.76
57	0.04	0	0.37	0.12	C	1.24	0.74
59	0.2	0.02	1.96	0.12		1.28	1.54
66	0.02	0	0.21	0.13		1.36	0.49
51	0.04	0.01	0.5	0.13		1.24	0.85
52	0.22	0.03	2.45	0.13	C	1.12	1.43
53	0.42	0.05	4.35	0.13	C	1.26	1.85
61	0.57	0.08	6.36	0.14		1.21	1.93
67	0.74	0.11	8.3	0.15		1.1	1.94
54	0.86	0.13	9.36	0.15	C	1.14	2.04
63	0.74	0.13	9.48	0.17		1.33	2.16
56	0.84	0.2	13.74	0.24	C/S	1.34	2.22
55	0.46	0.13	9.23	0.28	C/S	2.07	2.69
62	0.85	0.32	19.04	0.38		1.4	2.29

Kα source for selected experiments from the series, it was not possible to collect XRD data for all experiment due to sample size constraints. A summary of samples with XRD data collected is included in the table below, with XRD traces in SI Fig. 3. Two samples were identified with XRD peaks at 25.7 and 26.5 which are consistent with strontianite although a shift to higher 2θ values was observed, potentially indicating Calcite substitution into the lattice.

	BET surface area (m^2 g^{-1})	BET Constant (C)	r^2
a	0.208	-122	0.999
b	0.206	-108	0.999
c	0.206	-106	0.999
Average	0.206	-122	0.999

S.I. Section 2 - Specific Surface Area of Calcite Seed Crystal

The surface area of calcite seed crystals was determined by triplicate BET analysis using a Micromeritics Gemini VII 2390a instrument. A sample of calcite powder was weighed and dried overnight at a temperature of 105°C under a nitrogen atmosphere to remove any water, after which the sample was reweighed. A dead-space volume measurement was taken using helium which was then removed via vacuum and triplicate measurements were taken, using nitrogen as an absorbent at -196 °C. An average value of 0.206 m^{-2} L^{-1} was observed. By adding a mass of 0.73 g of the seed to the 150 mL reactor a surface area of 1 m2 L^{-1} was achieved.

S.I. Section 3 - Calcite morphology series

The following 5 images were collected on a FEI Quanta 650 Field Emission Gun SEM, from a suite samples with Wt. % Sr ranging from 0.02-9.36 %. These images focus on the elongate morphology, displaying its elongating with greater Sr incorporation.

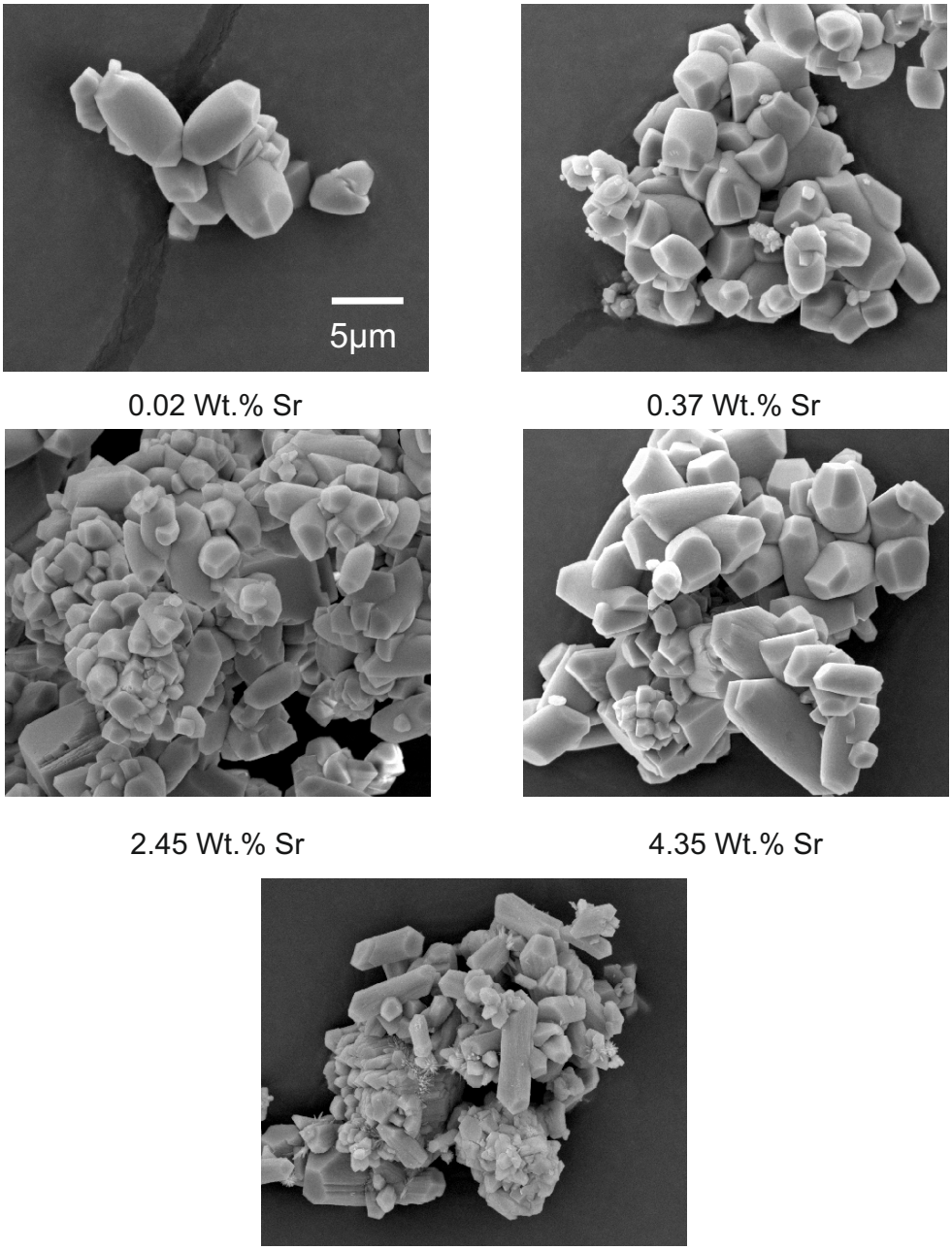

Figure C.2: Increase of the W/L of the elongate crystals with increasing Wt. % Sr

S.I. Section 4 - EDS Histogram

EDS spot analyses were carried out over 41 Rhombic crystals and 37 Crystals of fine material which presented as either elongate crystals or circular in cross section. Of the 41 Rhombic crystals 25 displayed no strontium above limits of detection while the remaining 16 displayed a median Sr/Ca of 0.019. All of the fine material registered Sr at concentrations above the LOD, with a median Sr/Ca of 0.25. This is displayed in the histogram in SI Figure 3.

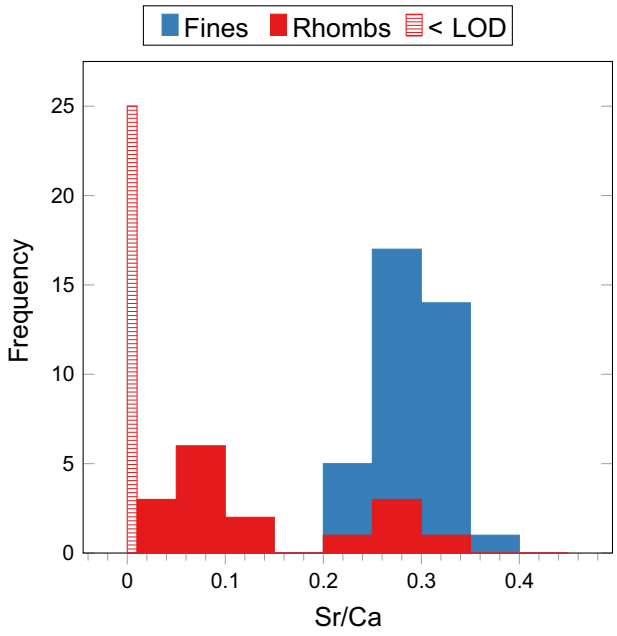

Figure C.3: Sr/Ca ratios from EDS spot analysis of a resin embedded sample of precipitate containing 6.36 Wt. % Sr

	Wt. % Sr	L (μm)	W (μm)	L/W
Elongate	0.02	4.00	2.50	1.59
	0.37	3.73	2.39	1.61
	2.45	3.00	1.65	1.82
	4.35	4.00	1.89	2.13
	9.36	3.48	1.38	2.5
	$\bar{x}$	3.64	1.96	1.86
Rhombic	$\bar{x}$	6.86	5.97	1.15

S.I. Section 5 - Rhombic Crystal Comparison

These micrographs are included to demonstrate the similarity in morphology of the seed crystals used at the start of the reaction and the rhombic morphology obtained at the completion of the reaction.

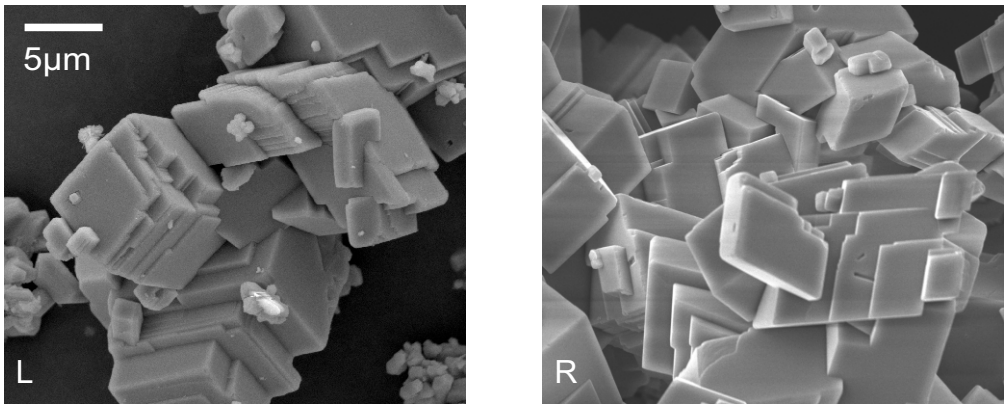

Figure C.4: Comparison of Rhombic crystal obtained from the seeded CTSR (L) and a sample of the seed crystals added at t=0 (R)

S.I. Section 6 - Data table

The final two experiments (56 and 62) were excluded from analyses as these displayed distribution coefficients indicative of strontianite formation. XRD analysis was carried out on sample 56 which returned a positive analysis for strontianite.

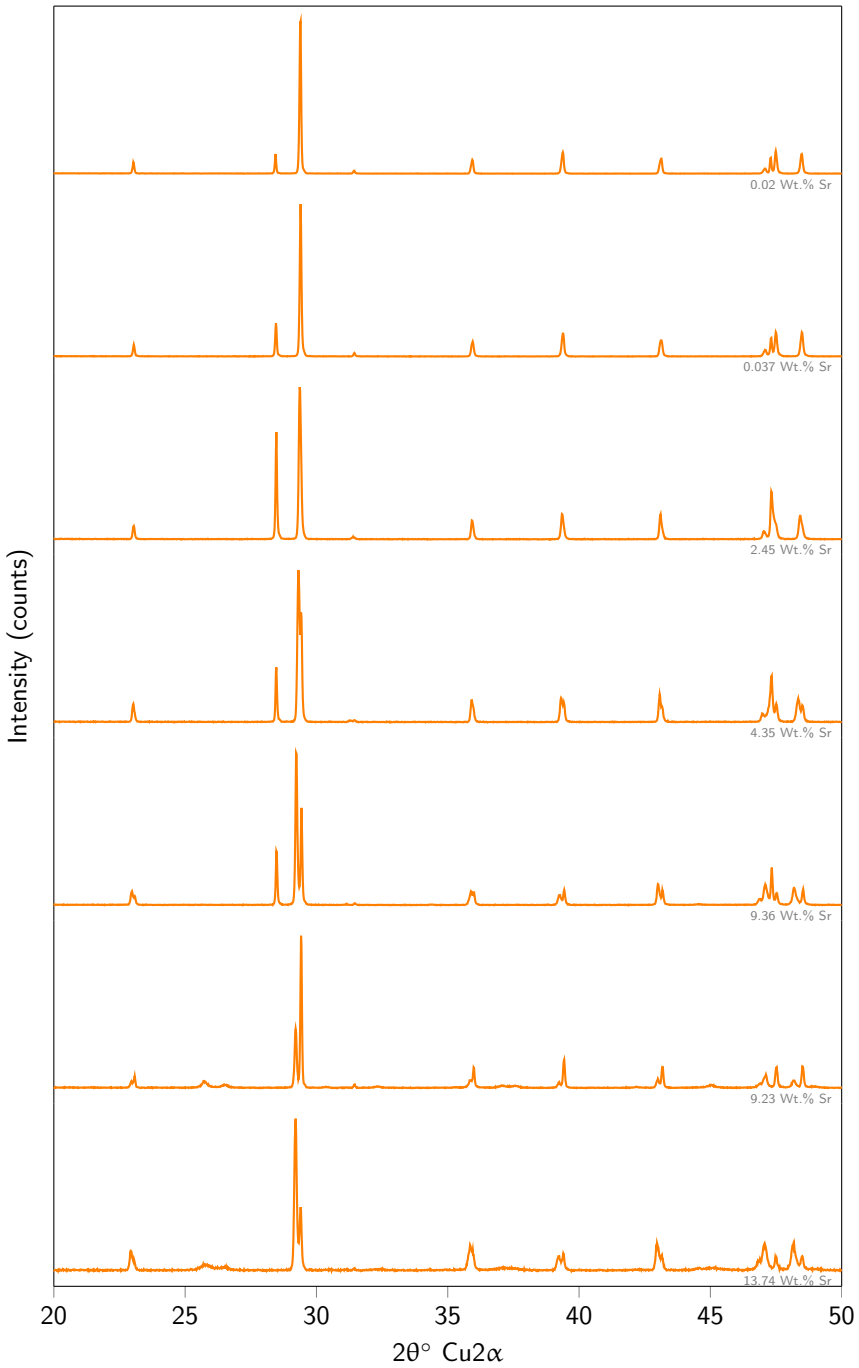

Figure C.1: XRD data for 7 samples from the unseeded constant composition experiments

#	Ca (mM)	Sr (mM)	TIC (mM)	a(Ca^{2+}) (mM)	a(Sr^{2+}) (mM)	a(CO_3^{2-}) (mM)	Sr/Ca (Solution)	Ca/CO_3 (Solution)	Sr/Ca (ppt)	Wt. % (ppt)	D_{Sr}	$SI_{Calcite}$ (R3c)	$SI_{Strontianite}$ (pcmn)	$SI_{Strontianite}$ (R3c)	Ionic Strength (mmol/L)	pH	Temp (°C)	Rate (mmol/h)
50	1.74	0.00	0.05	0.88	0.00	0.02	0.00	33.68	0.00	0.02	0.13	1.43	-0.54	-2.2	15.11	12.17	20.97	0.834
65	1.81	0.02	0.03	0.91	0.01	0.01	0.02	56.73	0.00	0.11	0.11	1.24	0.08	-1.58	15.36	12.22	21.30	0.781
66	1.82	0.03	0.06	0.91	0.02	0.02	0.04	29.76	0.01	0.21	0.13	1.53	0.58	-1.08	15.41	12.19	21.07	0.788
58	2.26	0.07	0.04	1.11	0.04	0.01	0.07	52.59	0.01	0.32	0.11	1.47	0.75	-0.91	16.67	12.24	21.07	0.837
57	2.04	0.07	0.04	1.02	0.04	0.01	0.08	48.73	0.01	0.73	0.12	1.41	0.74	-0.92	16.10	12.24	21.00	0.904
51	1.51	0.07	0.06	0.77	0.04	0.02	0.10	26.68	0.01	0.50	0.13	1.41	0.84	-0.82	14.72	12.06	21.06	1.009
59	1.74	0.35	0.05	0.88	0.20	0.02	0.44	32.69	0.05	1.96	0.12	1.45	1.53	-0.13	16.16	12.22	20.70	0.916
52	1.39	0.31	0.05	0.71	0.18	0.02	0.49	30.15	0.06	2.45	0.13	1.29	1.42	-0.24	15.12	12.03	21.10	0.959
60	1.74	0.68	0.05	0.87	0.38	0.02	0.84	37.71	0.10	3.59	0.11	1.38	.175	0.09	17.13	12.20	21.03	0.882
53	1.38	0.58	0.06	0.70	0.33	0.02	0.93	21.26	0.12	4.35	0.13	1.43	1.84	0.18	15.89	12.02	21.27	0.979
61	1.77	1.01	0.05	0.88	0.56	0.02	1.24	39.18	0.18	6.36	0.14	1.38	1.92	0.26	18.19	12.18	20.73	0.862
67	1.45	1.08	0.04	0.73	0.61	0.01	1.63	33.82	0.24	8.30	0.15	1.28	1.93	0.27	17.56	12.11	21.03	0.755
54	1.17	1.01	0.06	0.61	0.58	0.02	1.89	20.18	0.28	9.36	0.15	1.32	2.03	0.37	16.63	12.09	17.83	0.807
63	1.73	1.28	0.06	0.86	0.71	0.02	1.62	28.75	0.28	9.48	0.17	1.50	2.15	0.49	18.89	12.12	21.00	0.742
56	1.73	1.43	0.06	0.86	0.79	0.02	1.84	27.20	0.45	13.74	0.24	1.51	2.21	0.55	19.32	12.13	21.17	0.848
62	2.25	1.91	0.05	1.09	1.02	0.01	1.86	41.38	0.71	19.04	0.38	1.57	2.28	0.62	22.15	12.09	20.93	0.667

C.1 S.I. Section 7 – Crystallography

Line drawings of selected crystals were extracted from selected SEM micrographs. The interfacial angles between these faces appears to be >90° although it is difficult to precisely measure the angles as the none of the facets are viewed face on by the SEM. The apex of each crystal clearly showed three main faces with one larger than the other two, it was assumed that this was the {104} face.

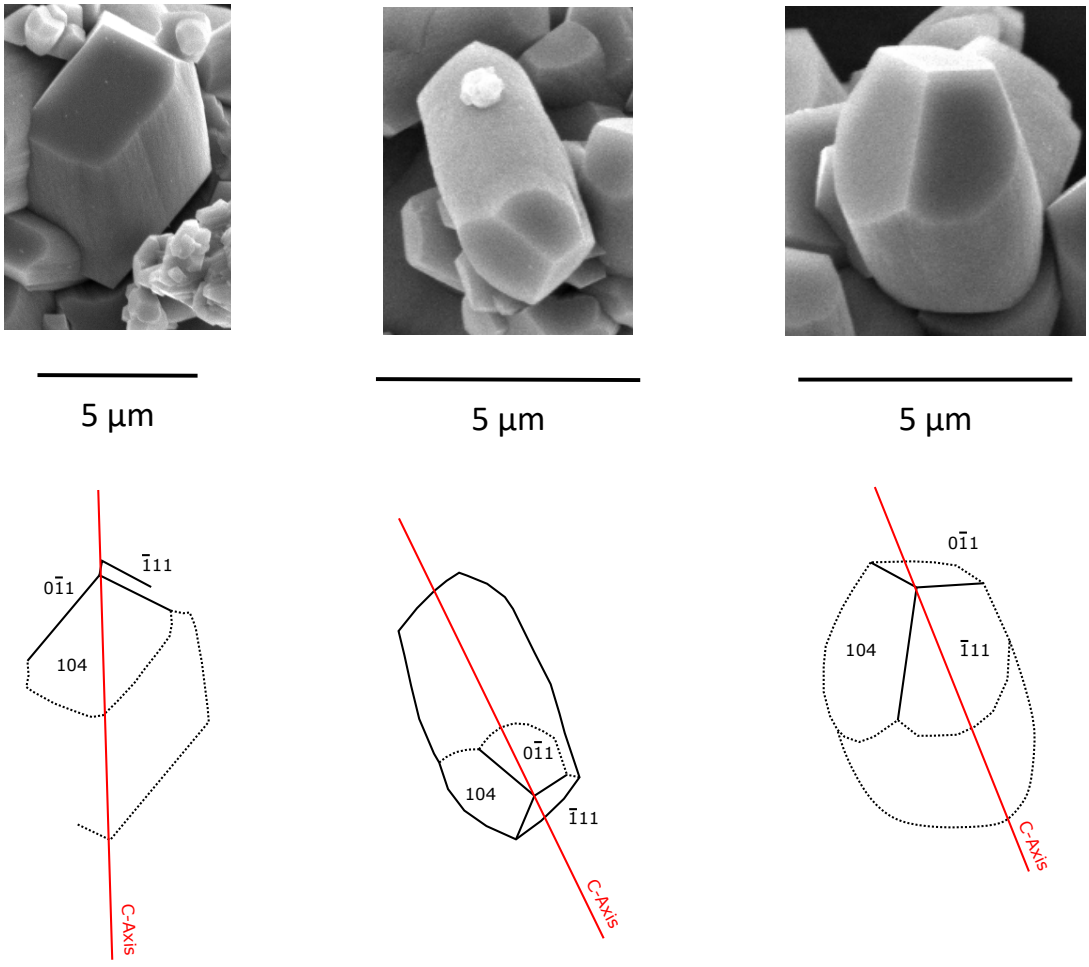

Figure C.5: Crystal line drawings displaying C-Axes and crystal faces.

Appendix D

S.I. for Section 7: Stability of radiolabelled carbonate wastes in cement waste forms

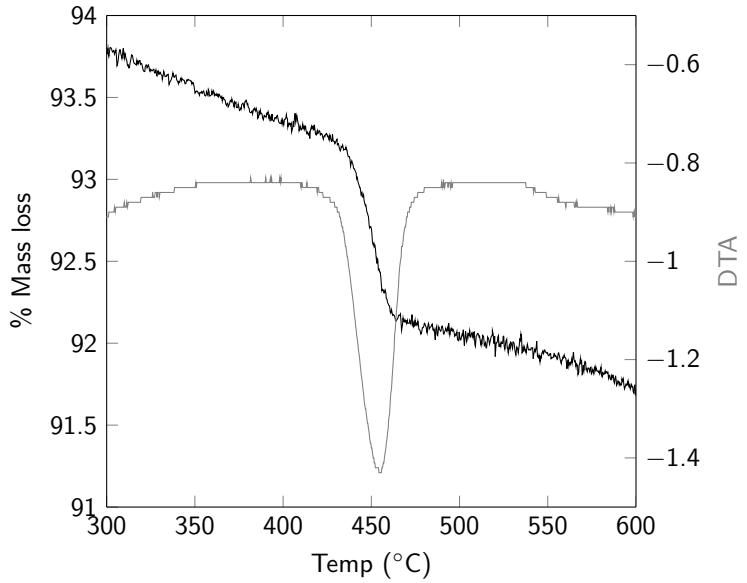

Figure D.1: TGA data from the 28 d endpoint of the 50-40-10 blended system

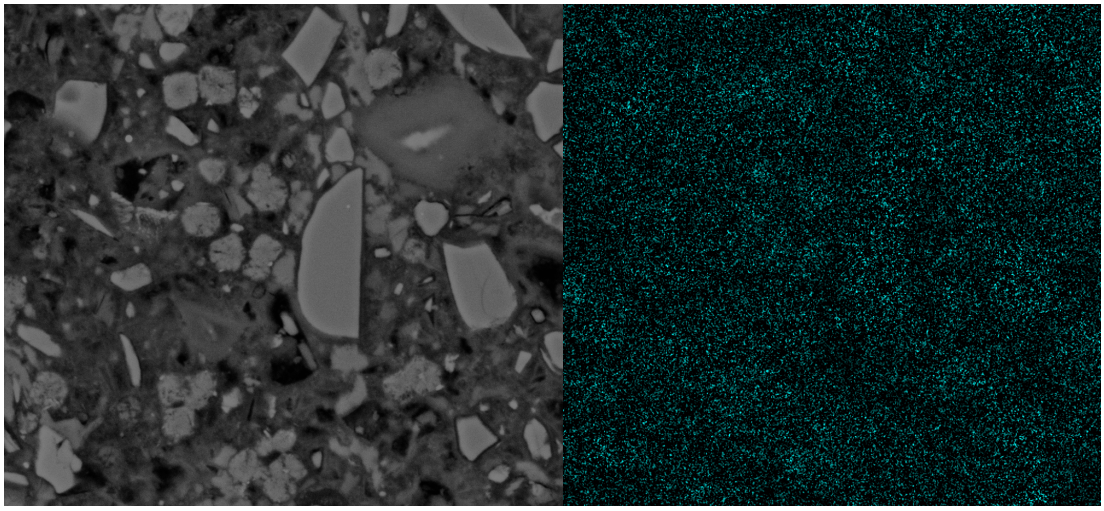

Figure D.2: EDS map displaying Sr distribution across a sample surface with associated SEM image.